ADVANCED MASTERS IN STRUCTURAL ANALYSIS
OF MONUMENTS AND HISTORICAL CONSTRUCTIONS

Master's Thesis

Tibebu Hunegn Birhane

Blast Analysis of Railway Masonry Bridges

This Masters Course has been funded with support from the European Commission. This publication reflects the views only of the author, and the Commission cannot be held responsible for any use which may be made of the information contained therein.

Portugal I 2009

DECLARATION

Name: Tibebu Hunegn Birhane

Email: tibebegnaw@yahoo.com

Title of the Msc Dissertation: Blast Analysis of Railway Masonry Bridges

Supervisor(s): Paulo B. Lourenço

Year: 2009

I hereby declare that all information in this document has been obtained and presented in accordance with academic rules and ethical conduct. I also declare that, as required by these rules and conduct, I have fully cited and referenced all material and results that are not original to this work.

I hereby declare that the MSc Consortium responsible for the Advanced Masters in Structural Analysis of Monuments and Historical Constructions is allowed to store and make available electronically the present MSc Dissertation.

University: University of Minho

Date: Sep 18, 2009

Signature: _____

ACKNOWLEDGEMENTS

I am very pleased to express my gratitude to my advisor prof. Paulo Lourenço, SACH cordinator, Department of Civil Engineering, University of Minho, for his meticulous advice and encouragement throughout the course of this work. I have been benefited greatly from his warm encouragement, understanding, amiability and guidance throughout the period of my stay at University of Minho.

My thanks are due to all who have been participated directly or indirectly for the successfull completion of this study.I would like to express my sincere gratitude to:

- All Professors and staff members of SAHC programme for their academic support.
- Mr. Pedro Medeiros for his continuous involvement in getting the laboratory works done.
- Prof. Nuno Peixinho and his research assistants for their collaborative support in executing the impact test in Mechanical Engineering laboratory.
- Secretariats of SAHC program: Mrs. Elisa Aghito, Mrs. Dora Coelho and Mrs. Sandra Pereira for their friendly support in dealing with all matters of the SAHC program.
- European Union for awarding the Erasmus Mundus scholarship of this study.
- ***Artecanter***, voluntary company which is involved in production of granite stone products in Guimarães, Portugal.
- Mr. Yohanes Adane for his crucial involvement in my career development.
- My parents and friends who have been with me throughout my career development. With out their continuous moral and economic support, their inspiration and encouragement, this success may never have been happened.

ABSTRACT

In addition to threats from natural hazards, infrastructures have been suffered a lot from extreme loadings resulting from man-made hazards. These include impacts from fast moving projectiles, blasts and shocks resulting from explosions. These threats have been attributed to wars or terrorist activities.

Studying the structural action effects from explosions is a subject of much actuality and considerable lack of expertise. Europe has never been so rich and safe, where the violent years of the first half of the 20th century lead to an unprecedented period of peace and stability. Despite the terrorist decades, e.g. connected to ETA and IRA, the attacks of Madrid (2004), London (2005) and worldwide (New York, Oklahoma, Mumbai) had a major psychological effect in the societies. The perception of a terrorist attack became a key issue for the European citizens and 79% of the citizens would like to see joint action of EU in fighting terrorism. Clearly, the understanding about the effect of blast loading in structures and their subsystems saves lives and reduces damage in infrastructures.

Structural assesment of historic masonry bridges for actions from explosions require a detailed understanding of blast phenomena and the dynamic behaviour of the structural components at high strain rates. For this purpose, a comprehensive overview about explosions, the mechanism of blast and the emperical formulation of blast loads as applied to arch bridges are made. More over both quasistatic and dynamic behavior of a prototype arch was assesed both numerically and experimentaly.

Hence with this aim, a scaled prototype single span stone masonry arch was designed and its quasi-static and high rate dynamic behaviour was assessed both experimentally and numerically. In order to investigate whether or not a dynamic enhancement existed at global level and to assess the energy absorbing capacity of the arch, it is necessary to predict the quasi-static force deformation capacity of a structure. This structural evaluation was carried out by displacement controlled experimental testing, simplified limit analysis using Ring software, and advanced non-linear FEA using DIANA. Finally the performance of the arch at high rate loading was investigated through experimental impact test and by non-linear explicit dynamic analysis using LS-DYNA (integrated with ANSYS). The numerical and experimental results have been calibrated and important parameters that influence the assessment of masonry stone arch bridges at high rate loading have been identified.

RESUMO

Além das ameaças de desastres naturais, as infra-estruturas têm sofrido muito com cargas extremas resultantes ou causadas pelo homem. Estas incluem impactos do movimento de projécteis a alta velocidade, explosões e choques resultantes das explosões. Estas ameaças têm sido atribuídas às guerras ou actividades terroristas.

Estudar os efeitos da acção estrutural das explosões é um tema de grande actualidade e com relativa falta de experiência. A Europa nunca foi tão rica e segura. Os violentos anos da primeira metade do século 20 levaram a um período sem precedentes de paz e estabilidade, apesar de marcado por actos de terrorismo, por exemplo, os ligados à ETA e ao IRA, os atentados de Madrid (2004), Londres (2005) e em todo o mundo (Nova York, Oklahoma, Bombaim), que tiveram um efeito psicológico significativo nas sociedades. A percepção de um ataque terrorista tornou-se uma questão fundamental para os cidadãos europeus e 79% dos cidadãos gostariam de ver uma acção conjunta da UE na luta contra o terrorismo. Claramente, o entendimento sobre o efeito da explosão de carga nas estruturas e seus subsistemas salva vidas e reduz os danos nas infra-estruturas.

A análise estrutural de pontes de alvenaria histórica para as acções de explosões exigem uma compreensão detalhada do fenômeno da explosão e do comportamento dinâmico dos componentes estruturais quando sujeitos a deformações rápidas ou quase instântaneas. Para esse efeito, é dada uma visão abrangente sobre as explosões, o mecanismo de explosão e da formulação empírica de cargas de explosão quando aplicadas a pontes em arco. Adicionalemente o comportamento quasi-estático e dinâmico de um arco protótipo foi analisado numérica e experimentalmente.

Com este objectivo, um único protótipo em escala de um arco de alvenaria de pedra de um vão foi projectado e seu comportamento quase-estático e dinâmico a cargas de alta velocidade foi avaliado tanto experimental como numericamente. A fim de investigar se existe ou não um incremento no comportamento global do arco e para determinar a sua capacidade de absorção de energia, foi necessário prever a capacidade de deformação por apliacção de força de forma quasi-estática. Esta avaliação estrutural foi realizada por ensaio experimental com deslocamento controlado, análise limite simplificada cmo utilização do software Ring, e análise de elemtnos finitos não linear utilizando o software DIANA. Finalmente o desempenho do arco na apliacção de força em alta velociadde foi investigado através do teste de impacto experimental e análise não-linear dinâmica explícita usando o software LS-DYNA (integrado com o ANSYS). Os resultados numéricos e experimentais foram calibrados e parâmetros importantes que influenciam a avaliação de pontes de alvenaria de pedra em arcos nestas condições de carregamento foram identificados.

CONTENTS

LIST OF FIGURES

LIST OF TABLES

CHAPTER 1

INTRODUCTION

1.1 Background

Since recently it has becoming a feature of campaigns by terrorist organizations around the world to use explosives to destruct important infrastructures including historical structures. Of these, damages to historical masonry bridges, which has been used for railways and highways, will be a twofold-disruption of the traffic flow and lose of the historic fabric. An explosion on or immediately nearby a bridge can cause catastrophic damage on the bridge locally or globally leading to the total collapse. In addition to the economical and heritage lose, the treat can cause additional causalities if the explosion results from an explosive device carried by the train or vehicle crossing the bridge.

Due to the threat from such extreme loading conditions, efforts have been made during the past decades to develop methods of structural analysis and design to resist blast loads, particularly from military defence engineering. However the issue has become serious for civil infrastructures too after the campaigns of terrorist organizations. Hence it is mandatory to make structural assessment for historic structures and take appropriate safety measures against the probable catastrophic damage.

1.2 Problem Statement

Blast analysis of railway masonry bridges involves the evaluation of structural performance of stone masonry arches, which are the basic structural components of such bridges. Hence the issue involves three major topics:

- Accurate specification of actions on stone masonry bridges arising from explosions. When an explosion occurs on or near a bridge, the bridge will be subjected to blast pressure, impacts from fragments and base excitation from ground shock. Hence for accurate specification of such actions it is important to understand the interactions that occur between the structure and its surrounding during explosions.
- Accurate estimation of the resistance curve of structural system, the arches, using either a simplified guidelines or using robust numerical simulations.
- Accurate performance assessment of the bridge against such actions using either simplified procedures or refined numerical simulations.

1.3 Objectives

The structural assessment of masonry bridges against actions resulting from explosions is a paramount issue as the terrorist threats have been becoming prevalent since last decades. Numerical or analytical studies about the effect of impact and blast on civil infrastructures have been limited; most of the works were done for military protective structures. On the aim of developing a simplified guideline for blast performance of historic bridges, the following issues are identified to be studied in this thesis as a basis towards the development of the knowledge of structural performance assessment of historic masonry railway bridges against actions resulting from explosions.

- To review the blast mechanism and to define associated actions on masonry arch bridges.
- To identify the significant parameters that affect numerical simulation of stone masonry arch bridges in the quasi-static assessment and devise a formulation for their threshold values. Experimental tests are used to calibrate the numerical simulations.
- To study the behavior of stone masonry arches under high rate loading. The performance of stone masonry arches under impact has been simulated both numerically and experimentally.

1.4 Methodology and Scope

This study addresses the problem first by studying a comprehensive overview about explosions, the mechanism of blast and the empirical formulation of blast loads. It also presents the significant cases illustrating the past-performances of buildings and bridges under explosions and impacts.

Secondly a prototype single span stone masonry arch was designed. Both dry joint and mortar joint arches were simulated both experimentally and numerically to investigate the resistance curve of the arch. A simplified limit analysis using RING software and advanced non-linear FEA using DIANA were carried to predict the failure modes and capacity curves of the arch. A displacement controlled quasi-static experimental test was conducted on the arch specimens to calibrate numerical models and to identify and define the bounds of significant parameters that affect the resistance curve.

To characterize the performance of stone masonry arches at high rate loading, a single span stone masonry arch was assessed both experimentally and numerically for impact loading. The prototype arches were tested experimentally using a drop weight apparatus. The numerical simulation was carried out using an explicit dynamic analysis software LS-DYNA.

1.5 Thesis Organization

The primary aim of this Thesis is studying the performance of stone masonry arch bridges under actions from explosions such as impacts and blast pressures. Hence the Chapters of this report are organized in such away that the three fundamental issues of the problem are clearly addressed. As

discussed in the previous Sections, the issues are characterization of the blast mechanism and corresponding structural loads, identification of the resistance parameters to develop the capacity curve of masonry arches and evaluation of the high rate loading performance of such structural systems.. A total of 5 Chapters are presented. Following this introductory Chapter, the second Chapter briefly explains the mechanism of blast, past blast performance of infrastructures such as buildings and bridges and it provides background information about specifying blast actions on masonry arch bridges.

Chapter 3 is devoted to numerical and experimental investigation of the quasi-static capacity of stone masonry arches. A non-linear static FE analysis, using discrete interface model, was carried out to predict the failure mode in advance of the experimental work. A quasi-static experimental test was conducted on the arch and the force deformation behaviour of the arch was obtained. A sensitivity numerical analysis was carried out to figure out the range of values that gives similar global behaviour of the arch from both numerical and experimental simulations.

Chapter 4 presents performance assessment of stone masonry arches at high rate loading. A single span stone masonry arches were assessed both experimentally and numerically for impact loading. The prototype arches were tested experimentally using a drop weight apparatus. The numerical simulation was carried out using an explicit dynamic analysis software LS-DYNA. Finally a calibration of the numerical model was calibrated using the experimental results.

Finally, Chapter 8 draws conclusion from the work presented here in, and recommendations for future research are also suggested in it.

CHAPTER 2

BLAST LOADING: LITRATURE REVIEW

2.1 General

In addition to threats from natural hazards, infrastructures have been suffered a lot from extreme loadings resulting from man-made hazards. These include impacts from fast-moving projectiles, blasts and shocks resulting from explosions. These threats have been attributed to wars or terrorist activities.

Since recently it has becoming a feature of campaigns by terrorist organizations around the world to use explosives to destruct important infrastructures including historical structures. Of these, damages to historical masonry bridges, which has been used for railways and highways, will be a twofold-disruption of the traffic flow and lose of the historic fabric. An explosion occurring on or immediately nearby a bridge can cause catastrophic damage on the bridge locally or globally leading to the total collapse. In addition to the economical and heritage lose, the treat can cause additional causalities if the explosion results from an explosive device carried by the train or vehicle crossing the bridge.

Due to the threat from such extreme loading conditions, efforts have been made during the past decades to develop methods of structural analysis and design to resist blast loads, particularly from military defence engineering departments. However the issue has become serious for civil infrastructures too after the campaigns of terrorist organizations. Hence it is mandatory to make structural assessment for historic structures and take appropriate safety measures against the probable catastrophic damage.

Structural assessment of historic masonry bridges for blast loads require a detailed understanding of blast phenomena and the dynamic response of the structural components. This chapter presents a comprehensive overview about explosions, the mechanism of blast and the empirical formulation of blast loads. It also presents the typical examples to illustrate the past-performances of buildings and bridges under explosions and impacts.

2.2 Blast Mechanism

Explosives are capable of exerting sudden pressure on their surroundings as a rapid conversion of the substance into hot gases. Their pressure, which is raised by the generation of heat during explosion, overbalances the restraining pressure of the surroundings.

When an explosion occurs, the energy released from detonation of the charge is transferred to the surrounding medium-in this case either ground or air. This energy input causes the generation of shock waves (Bangash, 2006) that propagate outward from the centre of the explosion. When these waves encounter a bridge structure, the mode of propagation of the waves will change due to

refraction and diffraction phenomenon at the boundaries of the structure. There by the part of the energy is again damped to the structure causing it to respond either in elastic or inelastic mode.

Hence it is very important to understand and identify the parameters that affect size and propagation of blast waves and mechanism of their interaction with the structure (of interest) to predict the actions and action effects resulting from the interaction. In the following subsections, the sources of explosions and the propagation of blast waves in the surrounding media will be discussed. And hence the fundamental parameters that affect the blast-induced actions on the structure will be identified

2.2.1 Source of Blast-Explosions

An explosion is defined as a large-scale, rapid and sudden release of energy (NGO, Mendis, Gupta, & Ramsay, 2007). An explosion may result from the physical activities such as volcanic eruptions, nuclear reactions, or chemical reactions. In nuclear reactions, energy is released from the formation of different atomic nuclei by the redistribution of the protons and neutrons within the interacting nuclei, whereas the **rapid oxidation of fuel elements** (carbon and hydrogen atoms) is the main source of energy in the case of chemical explosions. The latter is main type of explosion caused by terrorist activity and will be discussed here.

Charges of bombs and explosives are generally made from materials composed of compounds of Nitrogen, Hydrogen, and Oxygen; in some cases with Potassium, and Sulphur (Bangash, 2006). Terrorists often manufacture their own military explosives using Semtex in order to attack buildings and other structures. Military explosives and bombs are made from expensive materials like TNT [symmetrical 2,4,6-trinitrotoluene-$C_6H_2(CH_3)(NO_2)_3$] and RDX.

All blast parameters are primarily dependent on the magnitude of explosion. The magnitude of an explosion is measured in terms of the amount of energy released during the explosion, which is usually referred as the explosive yield. Generally the accepted reference standard for explosive yield is the energy released in an explosion of TNT. When the high explosive is other than TNT, the equivalent energy is obtained by using the charge factor, CF, which is evaluated as

$$CF = \frac{mass\ specific\ energy\ of\ explosive\ charge}{mass\ specific\ energy\ of\ TNT} \qquad 2.1$$

where the mass specific energy is the explosive yield per kg of the charge.Table 2.1 TNT equivalent of explosive charges.Table 2.1 gives the mass specific energy and the corresponding charge factors of common explosive charges.

Table 2.1 TNT equivalent of explosive charges.

Explosives	Mass specific energy (kJ/kg)	TNT equivalent (CF)
TNT	4520	1.00
GDN (glycol dinitrate)	7232	1.60
Pyroxilene	4746	1.05
Pentrinite	6689.6	1.48
Dynamite	5876	1.30
Schneiderite	3164	0.70
Dinitrotoluene (DNT)	3164	0.70
Ethylenedinitramine	5650	1.25*
Compound B (0.6RDX+0.4TNT)	5190	1.148
RDX (cyclonite)	5360	1.185
HMX	5650	1.256
Semtex	5660	1.25*
Dentolite 50/50	-	1.129
DENT	-	1.282

* Identical

The charge factor is used to express the mass of explosive charges in terms of an equivalent TNT mass, which indirectly represents the yield of an explosive device. This is an important parameter which is used to describe the effect of source type on the induced blast waves. Based on the amount of charge they contain, explosives devices are categorized as small, medium and high or large (Bangash, 2006) as shown in Table 2.1Table 2.2.

Table 2.2 Size category of explosive devices

Explosive category	**Amount of charge, *W* (kg TNT)**
Small	≤ 5
Medium	$5 < W \leq 5$
Large	$20 < W \leq 100$
Very large	$100 < W \leq 2500$

2.2.2 Blast-wave propagation

An explosion may occur in the air and on or below the ground surface. When a bomb explodes, a rapid release of stored energy is characterized by an audible blast. The energy released is divided into two distinct phenomena – thermal radiation, and mechanical wave propagating in air and/or soil, known as *air blast* and *ground shock*, respectively. The detonation of a condensed high explosive generates hot gases under pressure up to 300 kilo bar and a temperature of about 3000-4000C° (Bangash, 2006). The hot gas expands forcing out the volume it occupies (see Figure 2.1). If the burst occurs in air, a layer of compressed air (blast wave) forms in front of this gas volume containing most of the energy released by the explosion. On the other hand when a charge is located below the surface, the explosion causes vibrations of the particles of the ground medium resulting in propagation of stress waves in the longitudinal direction.

As the blast wave propagates away from source of explosion, it increases air pressure to a value above the ambient atmospheric pressure. This is referred to as the side-on overpressure that decays as the shock wave expands outward from the explosion source. After a short time, the pressure behind the front may drop below the ambient pressure (see Figure 2.2 and Figure 2.10). During such a negative phase, a partial vacuum is created and air is sucked in. This is also accompanied by high suction winds that carry the debris for long distances away from the explosion source.

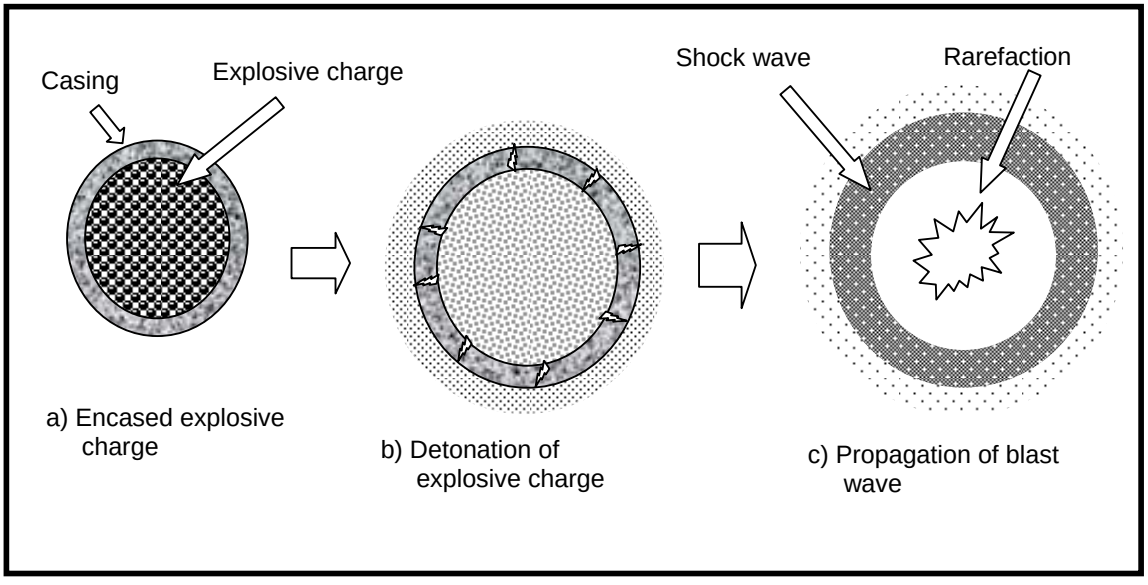

Figure 2.1 Blasting process of explosive charge.

All blast parameters are primarily dependent on the amount of energy released by a detonation in the form of a blast wave and the distance from the explosion. As the blast pressure expands spherically outward from the source, the peak over-pressure of the shock decrease where as the duration of the

pulse increases (see Figure 2.2). Blast scaling laws are used to describe the variation of blast parameters in terms of the explosive size and the source-target distance. The magnitude of the pressure, P, is roughly proportional to the size of the explosive, $E\ (kJ)$, *and i*nversely proportional to the stand of distance, R,.

$$P \propto \frac{E}{R^3} \qquad 2.2$$

The stand-off distance, R, is the effective distance from the centre of the charge to target point experiencing the blast pressure. A universal normalized description of the blast effects can be given by scaling distance relative to $(E / p_o)^{1/3}$ and scaling pressure relative to P_o, where E is the energy release (kJ) and P_o the ambient pressure (typically $100\ kN/m^2$). However, it is convenient to express the basic explosive input or charge weight W as an equivalent mass of TNT, generally expressed in kilograms. Therefore parameters of blast effects are expressed in terms of the dimensional distance parameter (scaled distance), Z, given by

$$Z = \frac{R}{W^{1/3}} \qquad 2.3$$

where *R and w are defined above.*

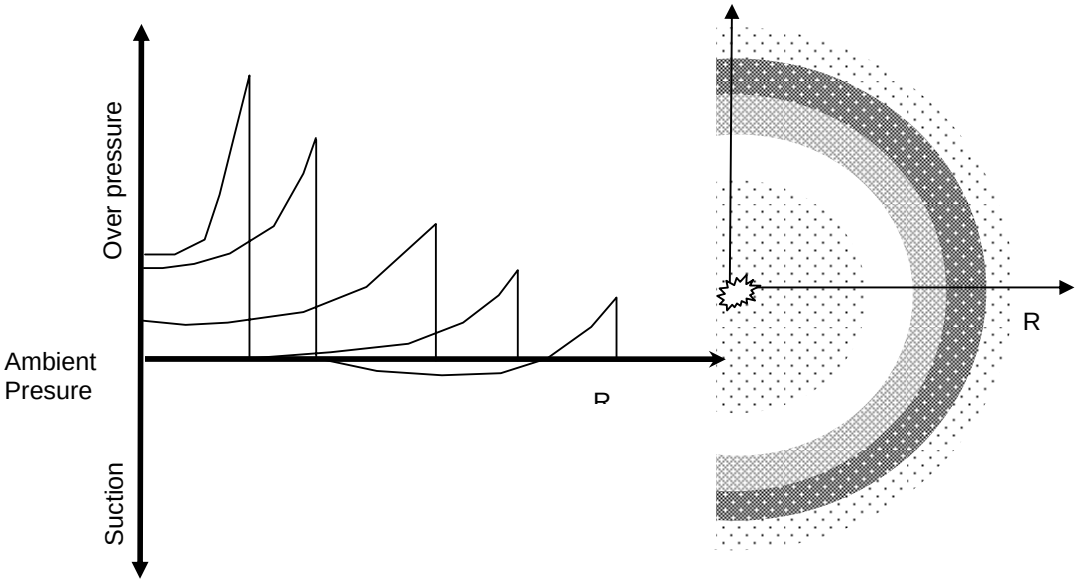

Figure 2.2 Blast pressure variation with blast wave propagation.

After explosion, the blast wave may interact with the ground or directly hit the structure without any reinforcement from the ground reflections. This depends on the location of the blast above the ground with respect to the target structure (TM 5-1300, 1990). Hence we can have three kinds of bursts:

- *Free-air burst: An explosion* which occurs in free air and when the incident wave reaches the structure before being reinforced with ground reflections.
- *Air- burst Explosion*: An explosion which is located at a distance from and above structures so that the ground reflections of the initial wave occur prior to the burst arrival of the blast wave at the structure. An air burst is limited to an explosion which occurs at two to three times the height of a one or two-story building.
- *Surface Burst*: Surface burst occurs when the charge detonation takes place close or on the ground. Unlike what happens in air-burst, the incident and the ground reflected waves are merged near the detonation pint to form a single reinforced hemispherical wave.

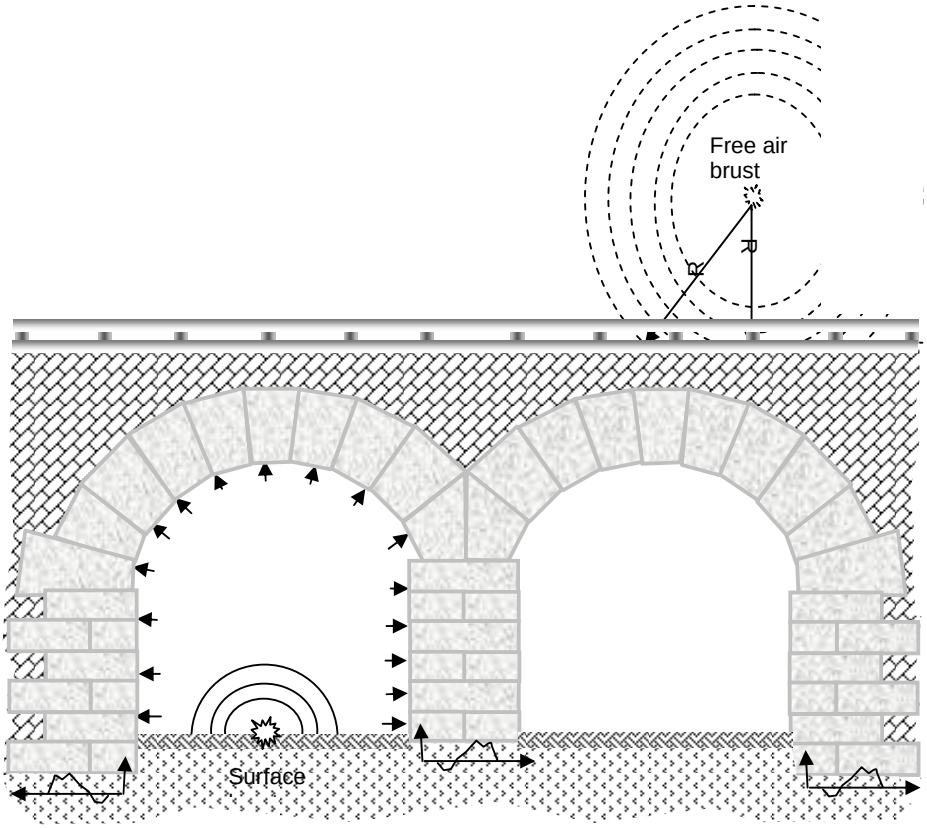

Figure 2.3 Possible burst environments for a masonry bridge-surface burst causing direct ground shock and blast pressure on the intrados of arch, and free air burst causing blast pressure on extrados.

2.3 Past Blast Performances of Structures

Civil infrastructures have been subjected to damages caused by war bombings and have been targeted by terrorist attacks in recent years. This Section deals with the historical survey of important buildings hit directly by bomb explosion and typical bridges damaged during the Second World War.

It has been noted that structural continuity, structural ductility and structural damping improves the blast performance of structures (Bangash, 2006) and (Bulson, 1997). Reinforced concrete structures have more mass, more damping and better energy-absorbing capacity to withstand action effects from explosions. Civil masonry and brick structures were known to have relatively little resistance to local explosions, and in earlier times no attempt was made to predict how they might behave under attack, or what their residual strength might be. Masonry and stone were not employed much in the construction of 'bomb-proof' shelters once reinforced concrete appeared on the structural scene (Bulson, 1997).

2.3.1 Explosives and Impactors used for Terrorist Activity

The most serious terrorist threat against civilian structures has been the use of explosives to detonate inside the building, a large external explosion near the structure and aircrafts to impact the structure. Typical terrorist bombs are homemade types and tend to be economical and are easy to obtain. Table 2.3 summarizes some recent terrorist attacks on buildings with bombs of variable magnitudes and intensity (Bangash, 2006).

Table 2.3 Explosives and impactors used for terrorist attack

Date	Site/Country	Explosive /Impact Load
April 1992	St. Mary Axe, London/UK	350 kg of TNT
April 1992	Staples corner, London/UK	300kg of TNT
Feb 1993	The world Trade center (WTC), NY/USA	0.6 tone of TNT
July 1994	Apartments, Israeli Embassy, London/UK	350kg of TNT
April 1995	Murrah Federal Building, Oklahoma City/ USA	33.1 tone of TNT
September 11, 2001	WTC, NY, USA	Boeing 767-200 ER Weight : 376672kg Speed: 530 miles/hr
September 11, 2001	Pentagon, USA	Boeing 757-200 aircraft Weight: 82.34 MN Speed: 240 m/s

2.3.2 Buildings Damaged by Terrorist attack

A bomb explosion within or around a building can have catastrophic effects, damaging and destroying internal or external portions of the building. It blows out large framework, walls and doors/windows and shuts down building services. The impact from the blast causes debris, fire and smoke and hence can result in injury and death to occupants. Typical building damages caused by terrorist attacks are presented below.

The Alfred P. Murrah Federal Building

In April 1995, the bombing of the Alfred P. Murrah Federal Building in Oklahoma City was one of the largest terrorist attacks in the USA. A car bomb, estimated to contain about 1800 kg of high explosives and located 3–5m from the north face of the building and about 12–15m from the east end, caused 168 fatalities and numerous injuries, and caused an estimated $50 million in damage (Bangash, 2006). Figure 2.4 indicates the Murrah Building prior to blast and its extensive damage part after explosion. The bomb was fertilizer-based (ammonium nitrate fuel oil ANFO) explosive which had the TNT equivalent 1814 (1.05) = 1905 kg.

a) Prior to blast

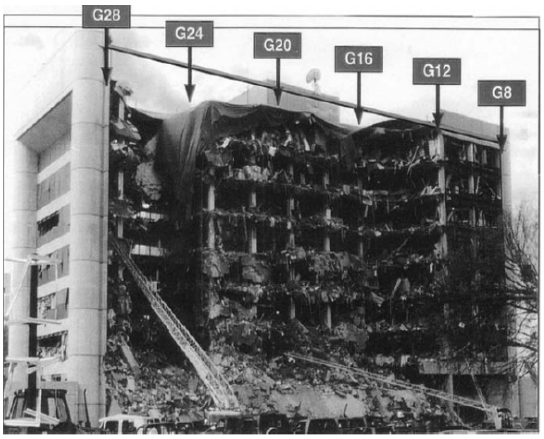

b) After Blast

Figure 2.4 Blast damage to Murah Building.

The Murrah Building was a nine-storey building of RC slab/column construction measuring 61.5m × 21.5 m. the explosion destroyed three of the four front columns and a centre-line column. With four columns completely destroyed, the upper floor toppled northward as the 200mm thick slabs separated from the centre-line columns. As a result, 8 of the 10 bays collapsed in the northern half of the building. Two bays collapsed on either side of the failed centre column in the southern half of the building (see Figure 2.4).

World trade centre (WTC) towers: The events following the attacks in New York City were among the worst building disasters in history and resulted in the largest loss of life from any single building collapse in the United States. Of the 58,000 people estimated to be at the WTC complex, 2,830 lost their lives that day, including 403 emergency responders. Two commercial airliners were hijacked, and each was flown into one of the two 110-storey towers. The structural damage sustained by each tower from the impact, combined with the ensuing fires, resulted in the total collapse of each building. As the towers collapsed, massive debris clouds consisting of crushed and broken building components fell onto and blew into surrounding structures, causing extensive collateral damage and, in some cases, igniting fires and causing additional collapses (see Figure 2.5). In total, 10 major buildings experienced partial or total collapse and approximately 30 million square feet of commercial office space was removed from service, of which 12 million belonged to the WTC Complex.

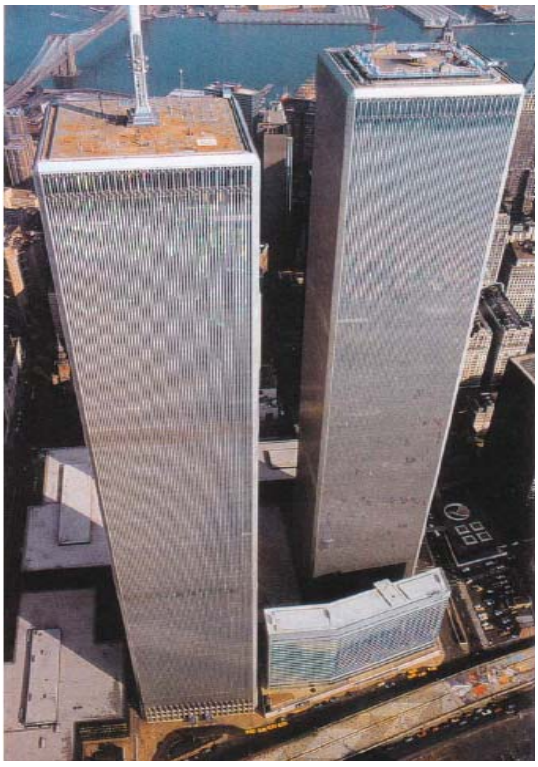

a) Before aircraft impact

b) After aircraft impact

Figure 2.5 World trade center towers before and after aircraft impact, 2001 (Adopted from M.Y.H. Bangash, 2006).

2.3.3 Threats on Bridges

Explosive damage to civil bridges has mainly occurred in the past as a result of military operations, either in an attacking mode when for tactical reasons it has been necessary to demolish bridges by

bombing, artillery shells, rockets or cruise missiles; or in a defensive situation where the demolition of a bridge prevented the enemy from advancing along a planned route (Bulson, 1997). Defensive demolition was normally carried out by the emplacement of cutting charges on selected bridge members. Instances have been recorded of damage due to terrorist activities, mainly relatively slight damage to decks and truss members. For example the damage of the Tila Bund bridge of Pakistan caused for the death of 80 people (Bangash, 2006).

One of the most informative investigations into bomb damage (from aerial bombs) on large civil bridges was made by a UK Ministry of Home Security team in 1944 for the British Bombing Research Mission. The Bombing Research Mission ascertained the effect of bombs of known weight across the Seine between Paris and Rouen. Ten railway girder bridges, nine railway arches, five road girders and three road arches were examined. Many of the bridges (the majority were rail bridges) were damaged three times during the Second World War; firstly when the French authorities demolished parts of bridges in 1940, secondly by the very severe bombing in mid-1944, and thirdly by the German army during the retreat from Normandy and Northern France in the autumn of 1944. In terms of residual strength, rapid repair and speedy re-use, some of the bridges examined provide useful information.

D'Eauplet Railway Bridge: It is a four span continuous steel truss bridge. The collapse of the pier caused for the partial span damage of the bridge, as shown in the Figure 2.6. The bombing history is given in Table 2.4.

Table 2.4 d'Eauplet railway bridge loading history (from P.S. Bulson)

Date	Bombs	Damage observation
7 May 1944	70x1000 GP bombs	No damage
25 May 1944	54x500 GP bombs	No damage
25 May 1944	8x500 GP bombs	No damage
25 May 1944	45x1000 GP bombs	Pier 3 severly shaken
25 May 1944	46x1000 GP bombs	Pier 3 hit again, causing complete destruction

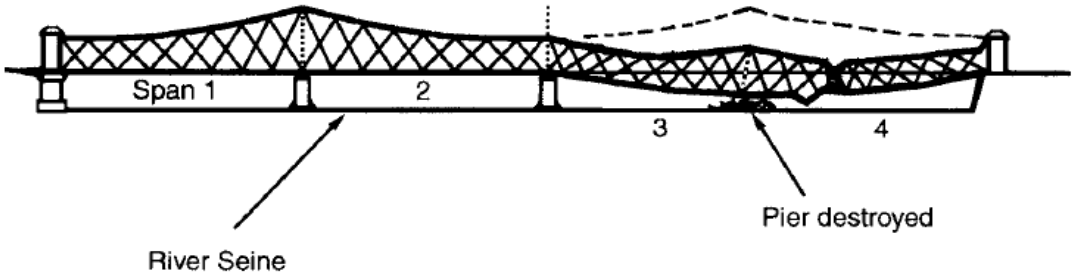

Figure 2.6 Bomb damage of d'Eauplet railway steel bridge, 1944 (from P.S. Bulson)

Le Manoir Railway Bridge: it is a three span steel girder bridge, located between Paris and Rouen. All the three spans were collapsed after successive direct hits of aerial bombs on deck as shown in the

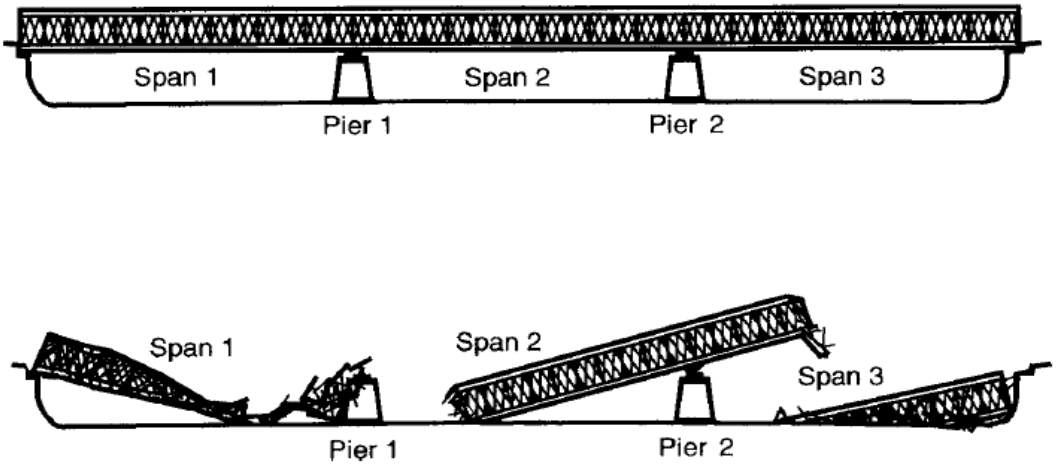

Figure 2.7.

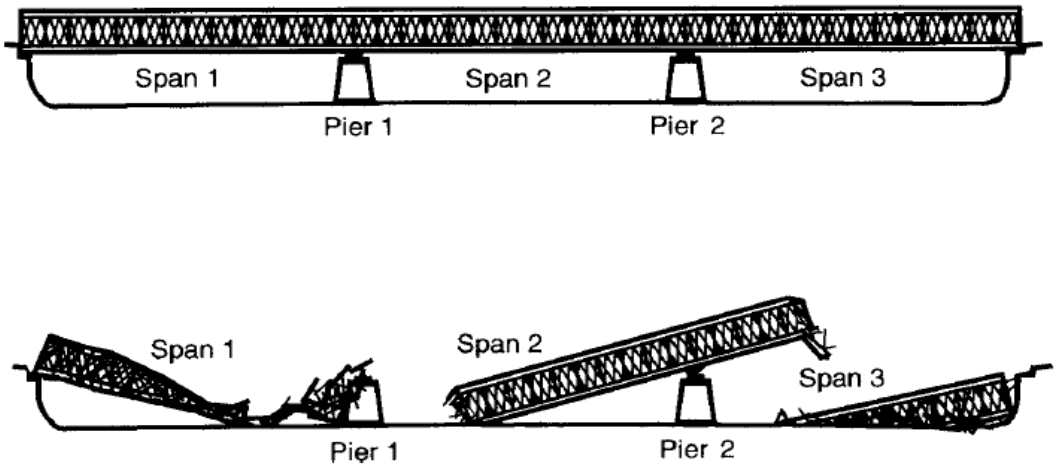

Figure 2.7 Bomb Damage of Le Manoir railway steel bridge, 1944 (from P.S. Bulson)

Vacoulers Railway Bridge: It is a single span mass concrete arch railway bridge, located 30 miles north-west of Paris, Figure 8.5.The bridge withstand direct hits of 97x2000 GP bombs on June 3, 1944 without any significant damage. However, the bridge was demolished after successive hits of 70X200 GP bombs during June 11 and June 12, 1944 as shown in the Figure 2.8.

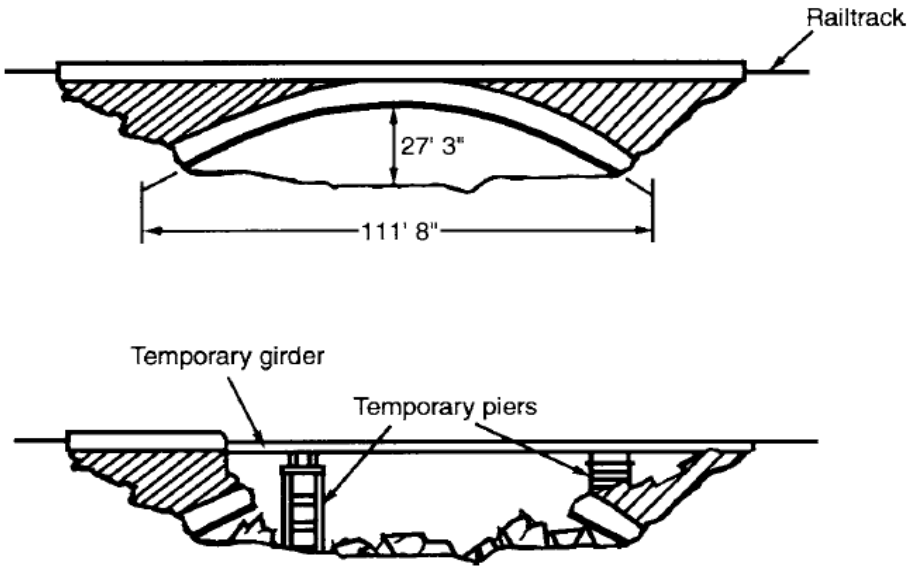

Figure 2.8 Bomb Damage of Vacoulers railway bridge, 1944 (from P.S. Bulson).

The Seine bridges report makes the general point that continuous girder bridges are very resistant to collapse by bombing and that in many positions the main girders of such bridges can be severed without concomitant collapse of the entire structure (Bulson, 1997). It was also clear from the survey that the most vulnerable components of heavy girder bridges were the piers. Masonry arches were found to suffer greater local damage from single hits, but the spans were less and temporary repairs were more readily carried out. The number of hits was very low on the Seine bridges. For every 100 bombs released in all types of attack (high level and low level) three direct hits were scored, two on the superstructure, one on the supports. And it was realized towards the end of the Second World War that the damage resulting from near misses of very large bombs could often be more significant than damage due to direct hits from smaller weapons.

The study concluded that for railway girder bridges the most efficient general purpose bombs were 2000 lb in total weight, and for road girder bridges 1000 lb bombs were more appropriate (Bulson, 1997). For masonry arch bridges the effectiveness of the bombs varied with span, from 1000 lb bombs (0 to 50 ft), to 2000 lb (50 to 100 ft). Although there were instances of 500 lb bombs being effective between 0 and 50 ft span, the use of 1000 lb bombs was thought to be preferable. High-level attack with instantaneous fusing of the bombs was recommended for girder bridges and low-level attack with delayed fusing for masonry arches.

2.4 Blast Load Specification

The energy release associated to detonation of an explosive charge causes

- to fragment the casing of the bomb and to shot the fragments,
- to shock the surrounding air and to create a propagating air-blast wave, and
- to generate ground shock waves.

Hence if a structure stands nearby the detonation, it will trap the energy released from the detonation from the interaction with either of the above listed energy carriers. In other words at least three types of loading actions must be considered to estimate the response of the structure from nearby or hit on explosion:

o impulse load or pressure pulse from air-blast wave,

o impact load from striking fragments, and

o base excitation from ground shock.

The aforementioned actions may give either a local or global response (damage) to the structure.

The severity of the structural action effects from explosions depends on the following parameters (TM 5-1300, 1990):

1. The magnitude of the explosion-the energy release during explosion which is described in terms of charge weight in an equivalent TNT
2. Charge location-the location of the explosion with respect to the structure (stand-off distance) and with respect to the ground affects the intensity of blast waves, ground shock waves and target velocity of the fragments.
3. The size and configuration of the structure: the sensitivity of the structure to respond globally or locally. It also affects the spatial distribution of the blast pressure on the structure.
4. The characteristics of the ground. This influences the blast pressure because of ground reflections and it affects kinematic characteristics of the shock waves propagating to the ground.

In the following Sub sections the quantification of actions on structures due to explosions will be reviewed.

2.4.1 Blast-Air Pressure Pulse

When high explosive detonates in a free air or above ground surface, a blast wave with a pressure front propagates in to a surrounding atmosphere. When this wave reaches to a structure, the wave front either reflects back or diffracts around the corners of the structure. During this interaction, the energy carried by the blast wave is tracked by the structure partially and deformed wave continues

propagation passing the structure. For uncoupled analysis, the effect of this interaction on the structure under consideration is represented by blast pressures. For any given set of free-field blast induced pressure pulses, the forces imparted to an above-ground structure can be divided in to four general components (Bangash, 2006):

- The force resulting from the incident pressure,
- The force associated with the dynamic pressure,
- The force resulting from the reflection of the incident pressure impinging upon an interfacing surface, and
- The pressure associated with the negative phase of the blast wave.

The relative significance of these parameters is dependent upon the geometrical configuration and the size of the structure, the orientation of the structure relative to the shock front, and the design purpose of the blast loads (TM 5-1300, 1990).

A blast load may be specified as an impulse rather than a pressure pulse (pressure time history) only if the duration of the applied pressure acting on the structure is shorter in comparison to its relative response time. However, if the time to reach maximum displacement is equal to or less than three times the load duration, the pressure pulse should be used for these cases (TM 5-1300, 1990).

The actual pressure-time relationship (pulse) resulting from a pressure distribution on a structure is highly irregular because of the **multiple** reflections, diffractions and time phasing, as shown inFigure 2.9. The net blast pressure pulse acting on the structure is given as a superposition of the incident, reflected and dynamic drag pressure. For simplicity of load specification, the pressure time relationship may be approximated by equivalent triangular pulse (TM 1300)

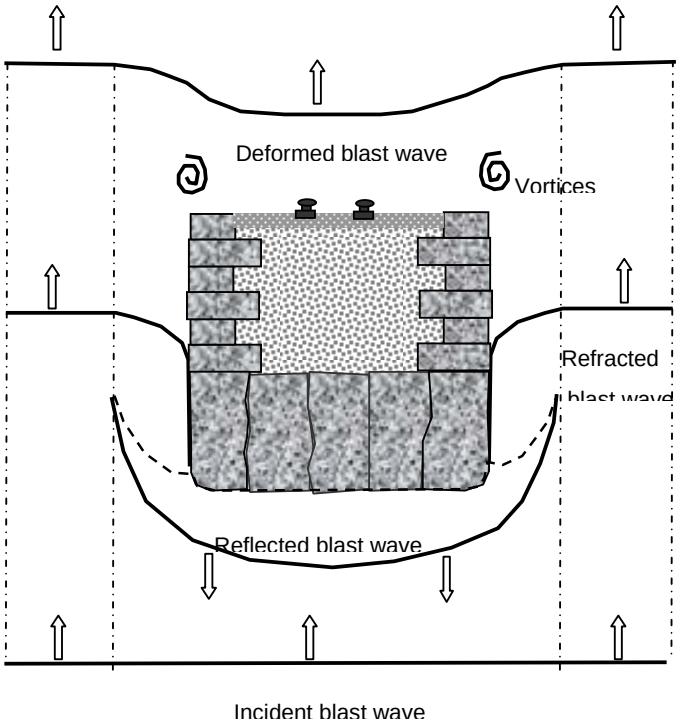

Figure 2.9 Blast wave propagation across a stone masonry arch section-surface brust.

***Incident Blast Pressure*:**

The blast wave resulting from a detonation of an uncased charge in ‘‘free air’’, i.e. distant from the nearest reflecting surface, is well known and often consists of compressed air front and a zone of rarefaction (vacuum formation). This is idealized by a presure pulse consisting a positive and negative phases as shown in Figure 2.10.

At the arrival time of the pressure front t_A, following the explosion, pressure at that position suddenly increases to a peak value of overpressure, P_{so}, over the ambient pressure, P_o. The pressure then decays to ambient level at time t_o, then decays further to an under pressure P_{so}^- (creating a partial vacuum) before eventually returning to ambient conditions. The quantity P_{so} is usually referred to as the peak side-on overpressure, incident peak overpressure or merely peak overpressure (TM 5-1300, 1990). Generally the ambient pressure is equal to 1bar ($100kN/m^2$) (Bangash).

Generally the over-pressure, P_{so} , at time ‘*t*’ after the arrival of the shock front is given by Friedlander Formulation (TM 5-1300, 1990) as:

$$P_s(t) = P_{so}\left(1 - \frac{t-t_A}{t_o}\right)e^{-\beta\frac{t-t_A}{t_o}} \qquad 2.4$$

Where P_{so}, t_A and t_o are defined above, and β is a shape parameter depending on the dimensionless scaled distance Z. It has been shown that the parameter β ranges from 0.1 to 10 (Gantes & Pnevmatikos, 2004). If β is smaller than one, there is an important negative phase, while for β larger

than one the negative phase becomes less significant. The value $\beta = 1$ is a reasonable average Value which is supported by experimental evidence. This value corresponds to positive phase impulse equals to that of the negative phase.

A full discussion and extensive charts for predicting blast pressures and blast durations are given by TM5-1300 (1990). However empirical expressions by different authors are presented as follows.

For a high explosive charge detonating at the ground surface, the maximum blast overpressure, P_{SO}, in bars can be calculated using Newmark and Hansen (1961) relationship as (NGO et. al, 2007):

$$P_{so} = 6784\frac{W}{R^3} + 93\left(\frac{W}{R^3}\right)^{1/2} \qquad 2.5$$

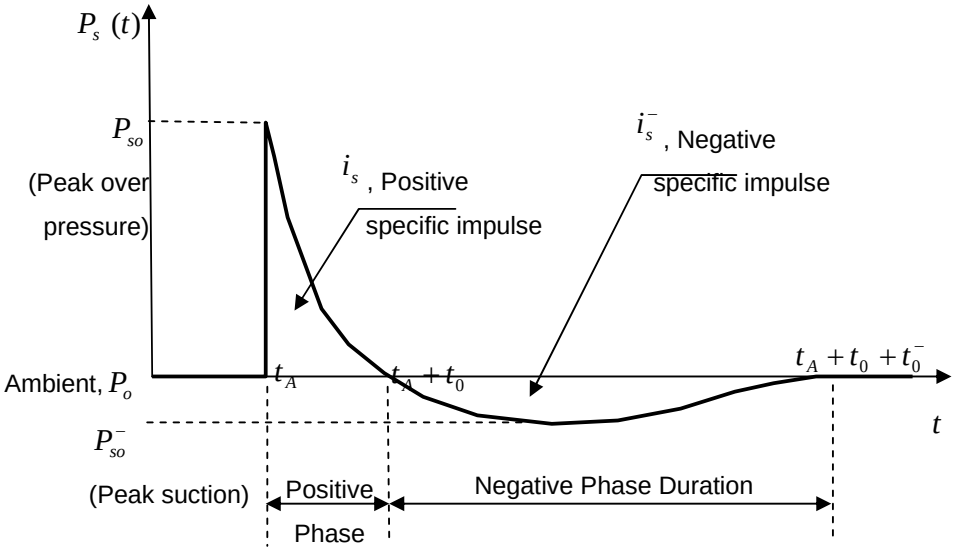

Figure 2.10 Incident blast pressure pulse (pressure time history).

The positive phase pulse duration, $t_o(milliseconds)$, which was proposed by Kinney and Graham (1985) as a function of scaled distance, $z\ (m/kg^{1/3})$, is given as (Pandy et.al, 2006):

$$\frac{t_o}{w^{1/3}} = \frac{980\left[1+\left(\frac{z}{0.54}\right)^{10}\right]}{\left[1+\left(\frac{z}{0.02}\right)^{3}\right]\left[1+\left(\frac{z}{0.74}\right)^{6}\right]\sqrt{1+\left(\frac{z}{6.9}\right)^{2}}} \qquad 2.6$$

The impulse of the incident pressures associated with the blast wave is the integrated area under the pressure-time curve. Consequently, the positive phase impulse i_s, is defined as follows:

$$i_s = \int_{t_A}^{t_A+t_o} P_s(t)dt \qquad 2.7$$

where t_A and t_o are arrival time and positive phase duration of blast wave.

The duration of the negative phase is longer than the positive phase, but the amplitude of the negative pressure is limited by the ambient pressure, P_o, and is often small compared to the peak overpressure, P_{so} . However, in design with regard to explosions the negative phase is considered less important than the positive phase and is therefore often disregarded (TM 5-1300, 1990).

***Reflected blast pressure*:**

When the air blast wave front strikes the face of the structure, reflection occurs and the overpressure amplified suddenly (seeFigure 2.9 and Figure 2.11). If the surface of the structure is perpendicular to the direction of the blast wave propagation, reflection increases the overpressure to a maximum reflected pressure P_r given by (Bangash, 2006):

$$P_r = 2P_{so}\left\{\frac{7P_o+4P_{so}}{7P_o+P_{so}}\right\} \qquad 2.8$$

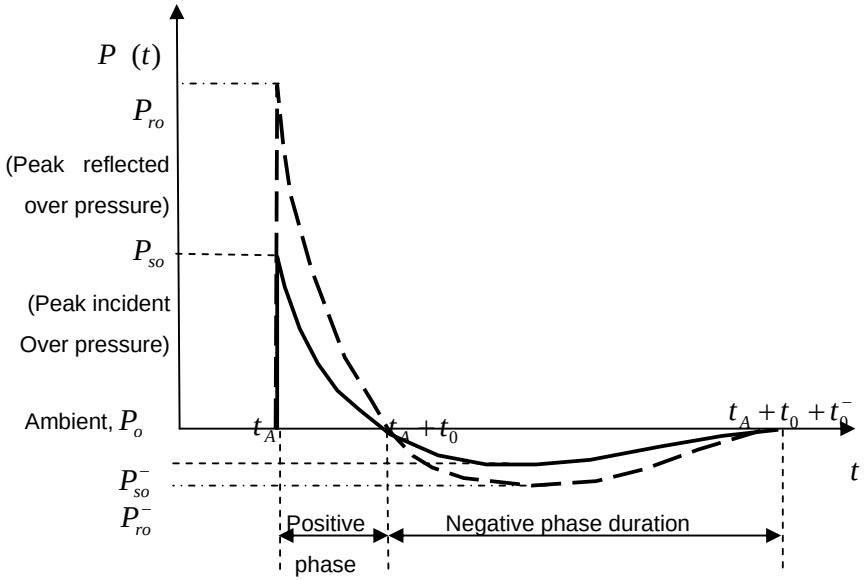

Figure 2.11 Typical reflected blast pressure pulse

***Dynamic Drag pressure*:**

As the blast wave propagates through the atmosphere, the air behind the shock front is moving outward at lower velocity. The velocity of the air particles, and hence the associated wind pressure, depends on the peak overpressure of the blast wave. Strong winds accompanying the blast wave produce dynamic pressure pulse as shown in the **Error! Reference source not found.**. The temporal variation of the dynamic pressure, $p_d(t)$, at a given distance from the explosion can be calculated as (Pandy et.al, 2006):

$$P_d(t) = P_{do}\left(1 - \frac{t}{t_o}\right)e^{-2\frac{t}{t_o}} \qquad 2.9$$

Here, P_{do} is the peak dynamic pressure, *and is given by* (NGO, Mendis, Gupta, & Ramsay, 2007)*:*

$$P_{do} = \frac{5P_{so}^2}{2(P_{so}+7P_o)} \qquad 2.10$$

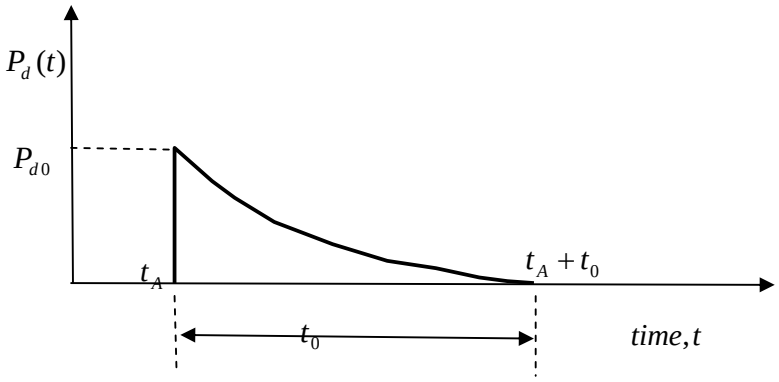

Figure 2.12 *Typical dynamic drag pressure pulse*.

2.4.2 Blast-Fragment Impact

As detonation of the explosive charge in a cased bomb is initiated, the inside temperature and pressure will increase rapidly and the casing will expand until it breaks up in to fragments (Nystrom & Gylltoft, 2009). After explosion, the fragments disperse around the surrounding with different mass distribution and initial velocity depending on the amount of the explosive charge, the type and the weight of casing. Empirical expressions for estimating the mass distribution and initial velocities of the fragments are given in (TM 5-1300, 1990). As the fragments travel through the air, before hitting the target, their velocity will decrease due to the drag forces.

The impact response of a structure to fragments depends on the mass distribution and the target velocity of fragments. It has been shown (Nystrom & Gylltoft, 2009) that the combined loading of blast and fragments, caused by explosions, results in damage greater than the sum of damage caused by the blast and fragment loading treated separately.

2.4.3 Base Excitation-Ground shock

The global blast-induced structural motion is result of the air shock-resulting from the strike of the air-blast wave on the superstructure, and ground shock-resulting from super-seismic wave striking the base of the structure. The energy imparted to the ground by the explosion is the main source of ground shock. The net ground shock experienced by a point on the ground surface is a combination of the air-blast-induced and direct-induced ground shock. The first component occurs when the air-blast compresses the ground surface and sends the stress pulse in to the underlying media; whereas the direct-induced ground shock results from the explosive energy transmitted directly through the ground.

The characteristics of the blast-induced shocks at a point on the ground surface depends on the amount of explosive charge, relative position of the charge to the ground surface, characteristics of the underlying soil, and source to site distance. Figure 2.13 shows velocity components of a typical air-blast- induced ground shock (TM 5-1300, 1990). Empirical formulas are given by and can be referred from (TM 5-1300, 1990) and (NGO, Mendis, Gupta, & Ramsay, 2007) to estimate the peak ground displacement, velocity and acceleration and direct reference can be made to the same.

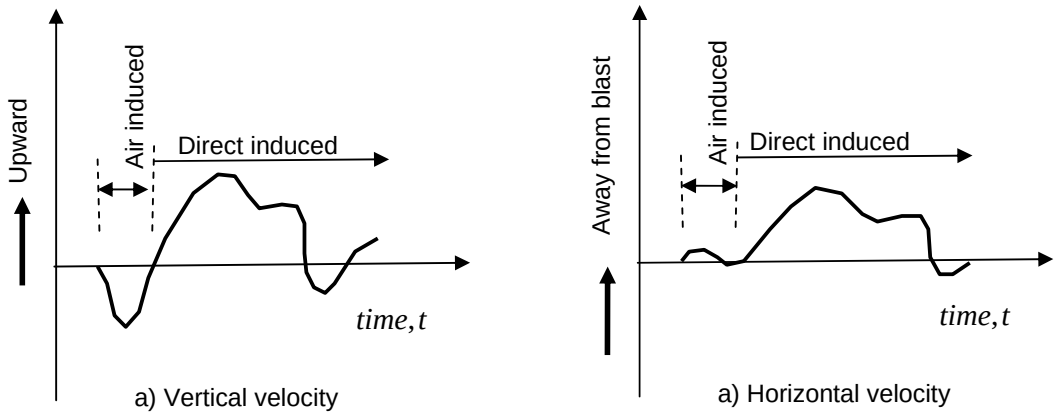

Figure 2.13 Net ground motions produced by an explosion at the ground surface.

CHAPTER 3

QUASI-STATIC PERFORMANCE OF STONE MASONRY BRIDGES: SINGLE SPAN ARCH

3.1 General

The main purpose of this Chapter is to assess the quasi-static capacity of a single span stone masonry arch. In order to investigate whether or not a dynamic enhancement existed at global label, it is necessary to predict the quasi-static force deformation capacity of a structure. Moreover, this assessment gives a bound to the energy absorbing capacity of the arch, the peak static strength, and both pre-peak and post- peak effective stiffness of the structure.

Hence with this aim, a prototype single span masonry arch was designed and its capacity was assessed both experimentally and numerically. The geometric design process was based on the dimensional-constraints of the lab and the same was aided by limit analysis using RING to have best efficient arch. Further a non-linear static FE analysis, using discrete interface model, was carried out to predict the failure mode in advance of the experimental work. A quasi-static experimental test was conducted on the arch and the force deformation behaviour of the arch was obtained.

Joint interface properties play a major role in numerical assessment of masonry stone bridges; therefore the influence of these parameters is addressed in this Chapter. A sensitivity numerical analysis was carried out to figure out the range of values that gives similar global behaviour of the arch from both numerical and experimental simulations.

3.2 Design of the Prototype Arch

A prototype stone masonry arch was designed primarily for impact response simulation. However the same arch was adopted for quasi-static tests too. For this reason, the global dimensions of the arch were fixed based on the geometric constraints of the drop-weight apparatus cell, see Figure 3.1.

Figure 3.1 Impact test apparatus cell, Mechanical Engineering Department lab, UM.

A segmental circular arch with an out-of-plane thickness of 200mm was designed, see Table 3.2 Geometric dimensions of the prototype single span stone-masonry arch.. The specification of the span, l_A, the rise, H_A , and the out-of-plane thickness, W_A are primarily based on the laboratory geometric constraints. The radial thickness of the arch ring and the number of units within the arch ring were determined by carrying out an iterative limit analysis using RING software. The description is given in Section 3.4.

Table 3.1 Review of geometric parameters of segmental masonry arches.

Source: [Arch'07]	H_A/l_A		t_A/l_A	
	From source	In this study	From source	In this study
Ceraldi et.al,2007		0.333	$\geq 1/24$	0.133
Hong, N.K., 2007	≤ 0.50		≥ 0.046	
Paredes, J.A.,2007			≥ 0.09	
Gilbert et.al.,2007	0.25		0.072	

Moreover the radial thickness-span ratio, t_A/l_A, and the span-rise ratio, H_A/l_A, was adjusted to conform to the ranges set from past experience, as shown in Table 3.1.

For the purpose of reusing the same units for different experimental arch set up, the stone blocks were specified to be made from sound granitic rocks. The units are prefabricated by a Voluntary Company, ***Artecanter***, which is involved in production of granite stone products in Guimaraes, Portugal. Even though a rotary sawing machine was used to cut out the units as per the prescribed dimensions, their surfaces are not perfectly smooth.

Table 3.2 Geometric dimensions of the prototype single span stone-masonry arch.

Units	No. of units	Length[Thickness or Height] [mm]	
		Intrados	Extrados
Voussoirs	12	118	147
Key stone	1	115.5	144.5
Abutment (skew back)	2	400[65]	400 [127]
Rise of the arch, $H_A = 400mm$, Clear span of the arch, $L_A = 1200mm$ and subtended angle of the arch = 135 degrees.			

3.3 Quasi-Static Material Properties

The behaviour of masonry arches under quasi-static loads depends on the physical and mechanical properties of the masonry units and that of the corresponding interface joints. The quasi-static behaviour of masonry arches is described by the capacity curve which shows the progressive deformation of the arch under incremental quasi-static load until the formation of a structural mechanism. Masonry arches transfer the superimposed loads by combined action of axial thrust and flexure. These action effects in turn induce compressive, tensile and shear stresses distributed with different intensity among different sections of the arch.

Hence the constituent material components of the arch should resist these stresses so as to transmit the external applied load to the appropriate support without collapse of the arch. The stress resisting capacity [Stress-strain profile and failure criteria] of masonry materials has been characterized through experimental investigations (Vasconcelos, 2005) (Snyman, Bird, & Martin, 1991) (Gilbert, Hobbs, & Molyneaux, 2002).

As the discussed in section 3.2, a segmental stone-masonry arch is taken for this study. There by the arch is composed of stone blocks and joints which are either dry or mortared. The stone blocks are made from typical granite found in Guimaraes, Portugal. Both physical and mechanical characterization of the stone blocks and the joints are based on the previous Ph.D.study by Vasconcelos. The material properties and failure criteria for stone masonry units and joints are discused and reproduced in the following sections in acordance with the required input form for the FEM software pakages.

3.3.1 Properties of Stone Blocks

The stone blocks adopted in this study were fabricated from granite rocks of Guimaraes, Northern city of Portugal. Granitic stone is the most widely used construction masonry material of ancient structures in Northern part of Portugal. Especially most of ancient buildings from Guimaraes are made of dry jointed masonry.

The textural and mineralogical properties of granite rocks from Guimaraes are of types ranging from fine to medium-grained biotitic. The mean density and the porosity of granite stones from Guimaraes is given in Table 3.3. (Vasconcelos, 2005)

Table 3.3 Expected values of physical properties of granite stones from Guimaraes

Stone type	Porosity (%)	Expected Density (kg/m^3)	
		Dry	Saturated
Fresh granite	0.47	2660	2665
Weathered granite	3.56	2579	2614

The mechanical characteristic of the stones is depicted from experimental campaign conducted by University of Minho (Vasconcelos, 2005). These stones are found to be weak and brittle in tension where as they are strong and brittle in compression. A typical stress strain curve of such stones is shown in Figure 3.2 Typical uni-axial stress-strain behavior of granite stone.Figure 3.2.

In the stone masonry arches, either with dry or mortar joints, the units are predominantly subjected to compression stresses, which are well below the peak compressive strength of the stone units, $f'_{c,u}$. Whereas under tension, as the joints are weaker than the units, the joints crack or form a gap in advance and hence give a tensile stress relief for the units. For

this reason, the stress-strain behavior of units is idealized as linear elastic both under tension and compression. And hence for discrete Finite Element (FE) simulation of the arch, Young's Modulus of elasticity and Poison's ratio are required.

The uni-axial mechanical properties of stone units are given in Table 3.4. The values in the table represent mean values of effective young's modulus of elasticity, $E_{c,u}$, compressive strength of stone units, $f'_{c,u}$, effective elastic stiffness under tension, $E_{t,u}$, the peak tensile strength of units, $f'_{t,u}$ and the tensile fracture energy of stone units,G_f^I.

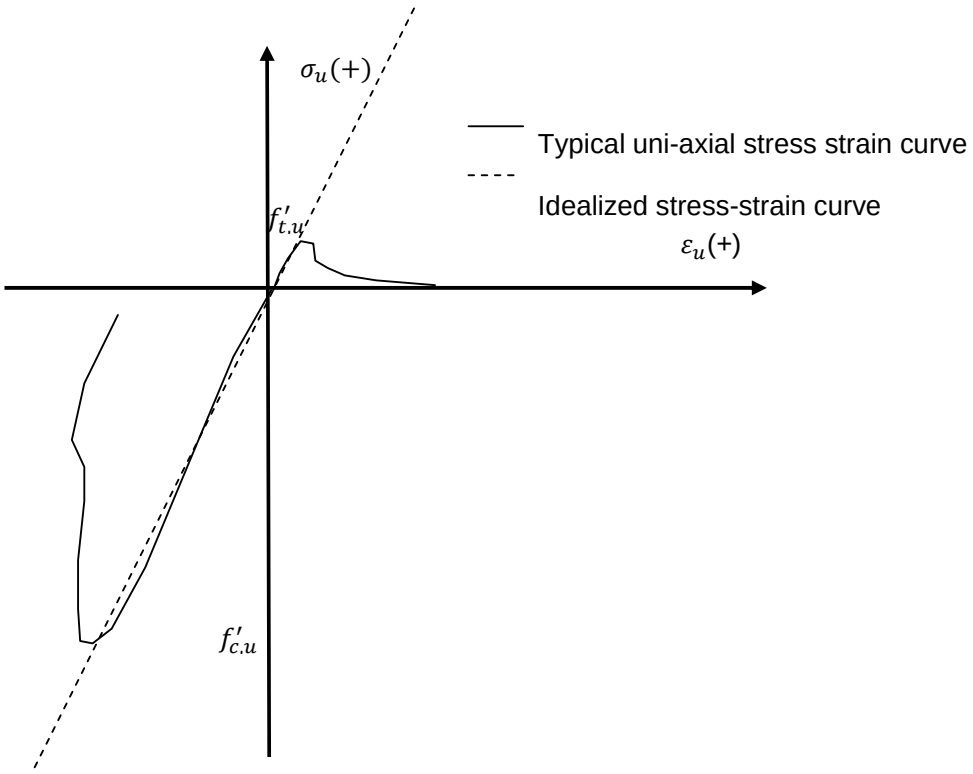

Figure 3.2 Typical uni-axial stress-strain behavior of granite stone.

The Poison's ratio of granite stones increases non-linearly with stress level (Vasconcelos, 2005), as shown in Figure 3.3. For both fresh [GA] and weathered [GA*] type of granite stones the Poison's ratio increases from 0.2 to 0.5 in the pre-peak elastic regime.

Table 3.4 Uni-axial mechanical characteristics of granite stones from Guimaraes

		Fresh granite	Weathered granite
Compression	$E_{c,u}\ (N/mm^2)$	52250	35090
	$f'_{c.u}\ (N/mm^2)$	148	90
	ν	0.23	0.30
Tension	$E_{t,u}\ (N/mm^2)$	12550	3180
	$f'_{t.u}\ (N/mm^2)$	6.01	3.52
	$G_f^I\ (N/mm^2)$	0.148	0.200

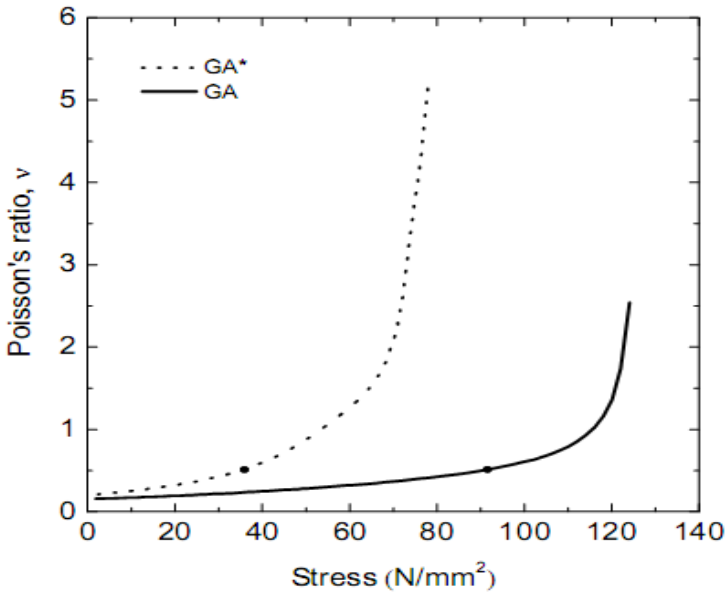

Figure 3.3 Variation of Poison's ratio of granite stone with compressive stress level, adopted from Vasconcelos, 2005.

3.3.2 Properties of stone masonry Joints

In a stone masonry arches, the joints may be either dry or mortared. In case of dry-jointed masonry, the blocks are stabilized by traction forces which are friction and normal thrust forces. The structural behavior of stone masonry joint is described in terms of a relation

between the normal and shear tractions and the normal and shear relative displacements across the interface [See Figure 3.4].

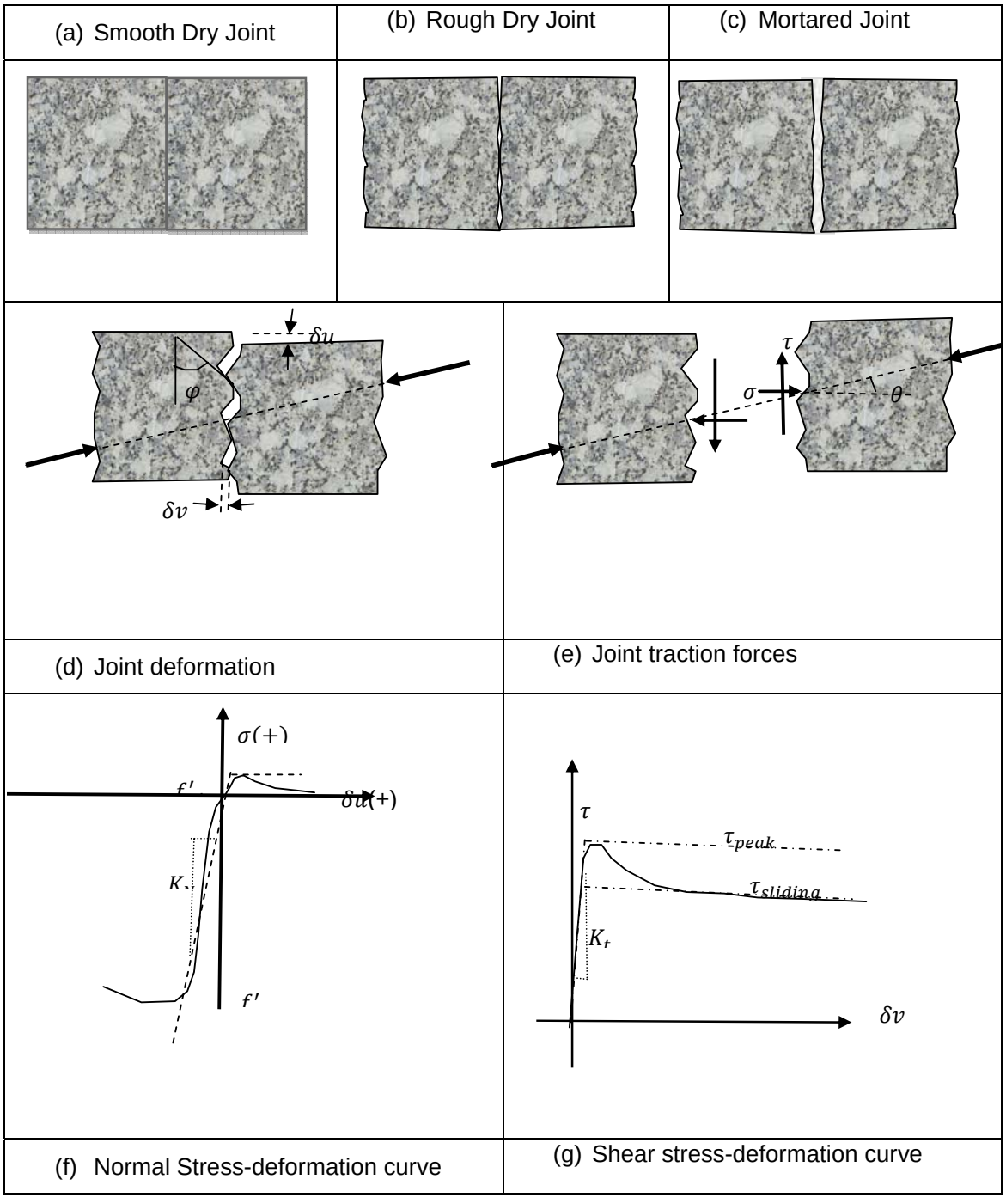

Figure 3.4 Force-deformation behavior of stone masonry joint.

3.3.2.1 Pre-Peak Behaviour- Effective Linear-Elastic Stiffness

In the basic Coulomb friction model, two contacting surfaces can carry shear stresses up to a certain magnitude across their interface before they start sliding relative to each other. This state is known as sticking or pre-peak behaviour [See Figure 3.13]. For dry joints, this is insured by interfacial interlock-characterized by coefficient of friction and the normal contacting stress. For the mortared joints, the resistance is assisted by the interfacial adhesion (cohesion). In this regime, both joint types are assumed to respond in linear elastic mode. Two parameters are required for this constitutive model:

- K_N the interfacial compression elastic modulus in units of [Force/Area/Length], and
- K_t the interfacial shear elastic modulus in units of [Force/Area/Length].

The formulation of these parameters is described in the following sub-sections.

I. *Penalty Stiffness Formulation*: This formulation is based on preventing the penetration of one material body into another material body across their interface. From this condition the normal stiffness of the interface (joint) per unit contact area, K_N, is given by (LS-DYNA):

$$K_N = \frac{p_f * A_c^2 * \boldsymbol{K}}{V_e} \qquad 3.1$$

Where

- P_f is penalty factor
- A_c is the contact area
- $\boldsymbol{K}$ bulk modulus of elasticity
- V_e is volume of the underlying element

For the full interface contact between the target and the contacting stone blocks, the area of contact, A_c, is given by

$$A_c = t_u * w_u \qquad 3.2$$

And the volume of the group of underlying elements along the contact interface, V_e, is given by:

$$V_e = t_u * w_u * le \qquad 3.3$$

Substituting l_u/N_e for l_e, the volume of each element can be obtained as

$$V_e = t_u * w_u * l_u/N_e \qquad 3.4$$

Substituting equation (3.6) in equation (3.1), we get:

$$K_N = \frac{p_f * A_c^2 * \boldsymbol{K}}{A_c l_u / N_e} \qquad 3.5$$

For two dimensional stress flow, the bulk modulus can be approximated as the ratio of Young's modulus to the cross sectional area (contact area), Hence the normal stiffness can be further simplified as:

$$K_N = \frac{p_f * N_e * E_u}{l_u} \qquad 3.6$$

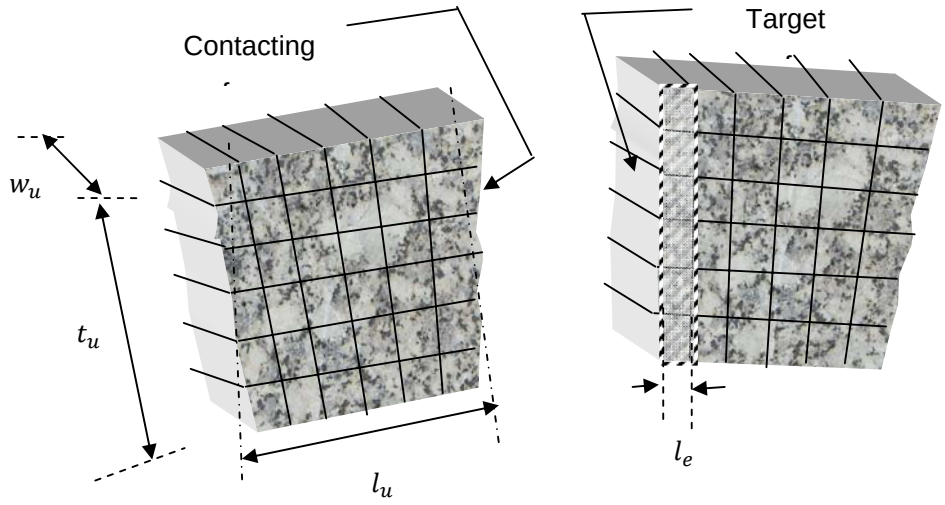

Figure 3.5 Joint stiffness formulation based on penalty contact algorithm

Therefore the normal stiffness of the joint can be expressed as a multiple of the effective axial stiffness per unit area of the stone units. Introducing the factor, bk, the stiffness of the interface can be generalized by the following formulation.

$$K_N = \beta_k K_u \qquad 3.7$$

In which:

β_k is the stiffness reduction factor, $\beta_k = p_f * N_e$, and

K_u is the effective normal stiffness of units per unit contact area evaluated as $K_u = E_u / l_u$.

II. *Joint stiffness from homogenised masonry property:*

For linear elastic behaviour assumption, the total deformation absorbed by the system is equal to the sum of the deformations of the stone units and the joint. This results the following compatibility equation.

$$\Delta u = \Delta u_{masonry} = \Delta u_{units} + \Delta u_{joint} \qquad 3.1$$

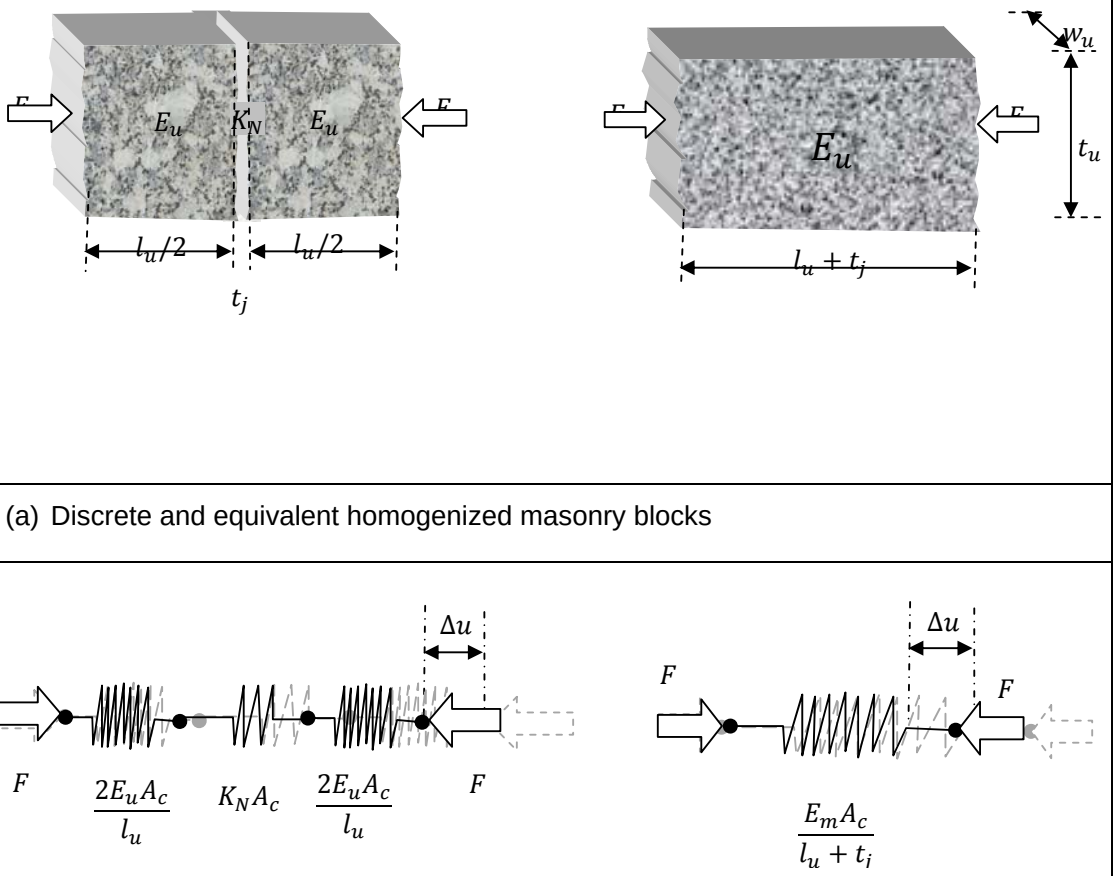

Figure 3.6 Equivalent elastic stiffness formulation of stone masonry joints based on homogenized masonry assumption.

From constitutive relations of linear spring elements, the translational deformation is evaluated as the ratio of the force to the spring stiffness. To ensure static equilibrium of the system, each discrete component should transmit the same amount of force as that of the external applied load, see Figure 3.6. Hence the compatibility equation can be expressed as

$$\frac{F}{\frac{E_m A_c}{l_u + t_j}} = \frac{F}{\frac{2E_u A_c}{l_u}} + \frac{F}{\frac{2E_u A_c}{l_u}} + \frac{F}{K_N A_c}$$

$$=> \frac{1}{\frac{E_m}{l_u + t_j}} = \frac{1}{\frac{E_u}{l_u}} + \frac{1}{K_N}$$

$$=> \frac{1}{K_N} = \frac{l_u + t_j}{E_m} - \frac{l_u}{E_u}$$

$$=> K_N = \frac{E_m E_u}{E_u(l_u + t_j) - E_m l_u}$$

$$=> K_N = \frac{E_m E_u}{E_u(l_u + t_j) - E_m l_u}$$

$$=> K_N = \frac{E_u}{l_u\left(\frac{E_u}{E_m} + \frac{t_j}{l_u} - 1\right)}$$

Therefore the normal stiffness of the stone masonry joint can be evaluated as:

$$K_N = \frac{K_u}{\left(\frac{E_u}{E_m} + \frac{t_j}{l_u} - 1\right)} \qquad 3.8$$

In general, the non dimensionless stiffness factor, β_k, can be formulated as

$$\beta_k = \begin{cases} p_f N_e & ; \quad to\ limit\ inter-penetration\ of\ units \\ or & \\ \frac{1}{\frac{E_u}{E_m} + \frac{t_u}{l_u} - 1} & ; \quad to\ match\ the\ homoginized\ masonry\ stiffness \end{cases} \qquad 3.9$$

The first formulation is dependent on the FE mesh size of the stone units whereas the second approach depends on the elasticity of the masonry, the elasticity of the units, and the relative size of joints with respect to that of the units. The identification of the parameters of the model may be performed through a monotonic uniaxial compression test on the units and masonry prisms.

As an indicator for the range of values of the factor, β_k, the results of the experimental work of Vasconcelos (Vasconcelos, 2005) were analyzed. During the experimental work, stone units having size of 150mmx150mmX150mm were used. Uni-axial Compression tests were conducted using Prisms made from three stone blocks. For mortared joints, 10mm thick lime mortar was used. Using mean values of Young's modules of elasticity of stone blocks and masonry, the normal stiffness factor, β_k, was calculated. The results are shown in Table 3.5.

It can be observed from the table 3.5 that the values of β_k is greatest for smoothly sawn dry joints. On the other hand, mortared rough masonry joints have the lowest value. For dry joints, thickness of the joint is taken as zero. This overestimates the stiffness. However masonry units can never be perfectly smooth, rather they have always some irregularities which are easily crushable.

Table 3.5 Joint stiffness parameters for stone masonry prisms

	Dry Joint		Mortared Joint	
	Smooth	rough	Smooth	rough
E_u	20200			
E_m	14722	7934	4629	1240
t_j/l_u	0.00*	0.00*	0.07	0.07
E_u/E_m	1.37	2.55	4.36	16.29
β_k	2.69	0.65	0.29	0.07

*Thickness of dry joints is taken as zero

The linear elastic tangential stiffness of the joint, K_t , can be formulated in similar fashion as normal stiffness by substituting the shear modulus of elasticity for young's modulus of elasticity. And it can be shown that, the elastic joint shear stiffness can be predicted from normal stiffness as:

$$K_t = \beta_t K_N \qquad 3.10$$

with a stiffness ratio, β_t, given by

$$\beta_t = \frac{1}{2(1-\nu)} \qquad 3.11$$

in which v is the Poison's ratio.

For stress levels below crushing strength of granite stone, poison's ratio varies from 0.2 to 0.5, (Vasconcelos, 2005). Using this range, the value of β_t varies from 0.625 to 1.0.

3.3.2.2 Post-Peak Behaviour: Failure Criteria

The joint failure is described by the interfacial separation. This interfacial separation is defined in terms of plastic relative joint displacement components, namely contact gap or penetration (crushing) and tangential slip distance (sliding). Hence the inelastic constitutive model of joint should ensure occurrence of these phenomena. This behavior is usually implemented in FE formulations using a combined Coulomb friction and gaping criteria (Lourenco, 1998).The model is characterized by six parameters [Figure 3.4 and Figure 3.7]:

- K_N the compression elastic modulus,
- K_t the shear elastic modulus,
- $f_t^{'}$ the maximum normal tensile stress (traction),
- c, cohesive frictional resistance
- μ the friction coefficient (tangent of the friction angle), and
- δ the dilatancy (tangent of the dilatancy angle) .

Here in this model the masonry units are assumed to perform elastically and hence there is no bound for the compression-sliding regime.

According to Coulomb friction model, two contacting surfaces start sliding relative to each other once the peak shear stress is reached. The sliding failure mode is simulated by dilatant friction model which is governed by Coulomb friction law. The Coulomb model can be formulated with the use of a yield surface function, f,

$$f = |\tau| + \mu|\sigma| - c \qquad 3.12$$

with the friction coefficient ,μ, and cohesive sliding resistance, c , which are dependent on the plastic shear deformation (Gilbert et.al, 2002 and Lourenco, 1998). The softening behavior of these parameters is given by [see Figure 3.7]:

$$c = c_o e^{-\left(\frac{c_o}{G_j}\right)\delta v^p} \qquad 3.13$$

$$\mu = \frac{\mu_s}{\frac{\mu_s}{\mu_k}\delta v^p + 1} \qquad 3.14$$

Where δv^p is the plastic shear deformation and $G_f^{"}$ is the shear-fracture energy which is is predominately dependant on the pre-compression stress, $\sigma\,[Mpa]$, as (Molyneaux, Beattie, Gilbert, Burnett, Hobbs, & Newton, 2002).

The friction resistance parameters for granite stone masonry joints are adopted from the works of Vasconcelos, 2005 as shown in the Table 3.6

Table 3.6 Frictional resistance parameters of granite stone masonry joints [Vasconcelos, 2005].

Friction parameters	Dry Joints		Mortared joints*
	Dry units	Saturated units	
c_o	-	-	0.36
μ_s	0.69	0.62	0.63
μ_s	0.65	0.60	0.78

*Lime mortar, with prescribed compressive strength of 3Mpa, was used

For stress range outside the elastic regime, interfacial sliding behavior is governed by non-associated plastic flow rule defined by the dilatancy. Dilatancy describes the ratio of normal displacement to that of plastic tangential displacement (sliding) [Figure 3.4]. Usually it is specified in terms of the resultant flow direction with respect to the tangential component, which is called dilatancy angle, δ . The value of dilatancy angle is estimated from:

$$\varphi = tan^{-}(\delta) = (\frac{\delta u}{\delta v}). \qquad 3.15$$

where $\delta u\ and\ \delta v$ are normal and tangential relative displacements obtained through experimental measurements.

The opening of the joint is associated to positive dilation, whereas negative values of dilatancy represent the compaction of the joint. The dilatancy of a masonry joint interface is mostly controlled by the joint roughness, and is dependent on the residual plastic shear deformation. Depending on the roughness of the interface, dilatancy,δ, of masonry joints ranges from $0.1\ to\ 0.7$ (Gilbert, Hobbs, & Molyneaux, 2002). However it has been reported by Vasconcelos (2005) that dilatancy is insignificant for dry sawn granite units. Hence, for

numerical analysis of arches considered in this study, the dilatancy was not taken in to account.

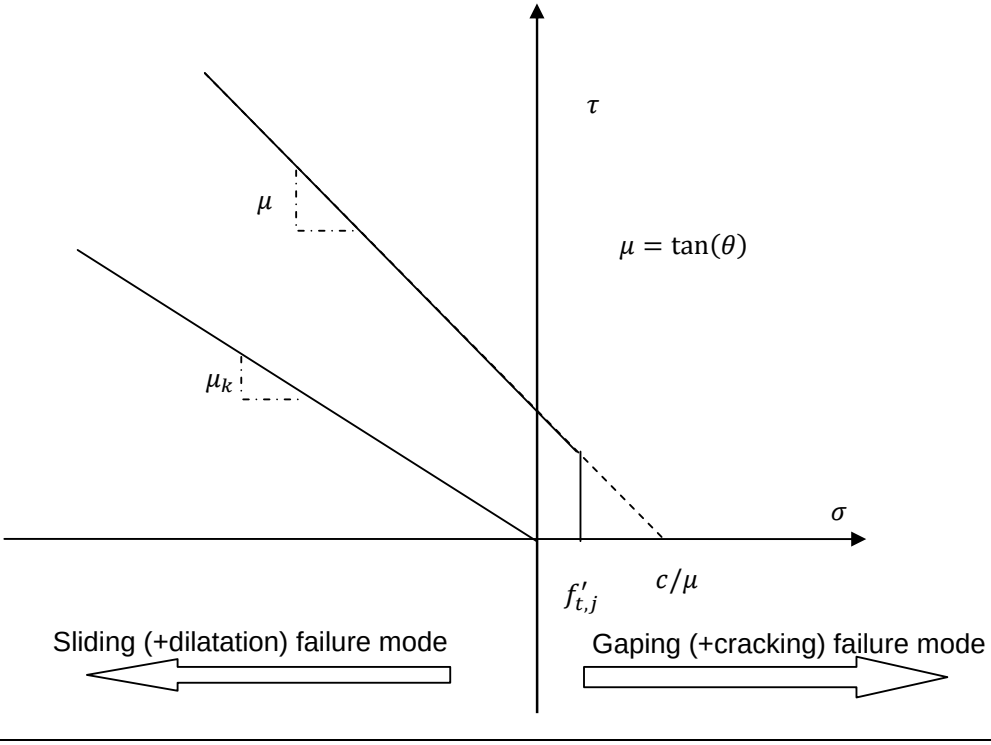

(a) Failure criteria of a stone masonry joint

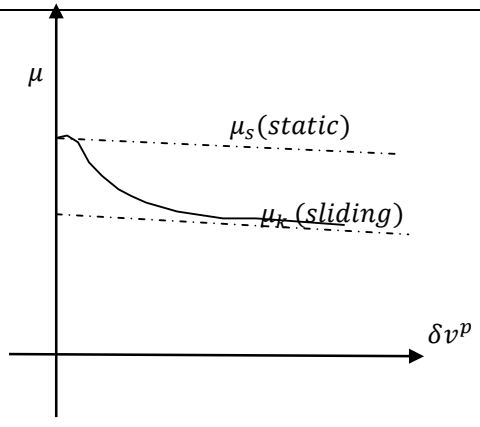

(b) Softening of friction coefficient

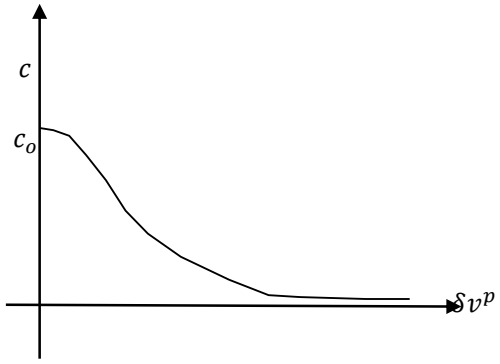

(c) Softening of cohesion

Figure 3.7 *Mathematical interface models for post-peak behavior of masonry joints.*

In the tensile regime, the performance of joints is highly dependent on the interfacial cohesion. The tensile strength of joint ,f_t', ranges from zero to the apex of the Coulomb friction failure curve [$0 \leq f_t' \leq c/\mu$]. The post-peak behavior of masonry joints under tension is usually simulated by discrete-cracking with a gap criterion. This model assumes that a gap arises if the tensile traction, σ_t , normal to the interface exceeds the specified tensile strength. After gap formation, σ_t is reduced to zero immediately (brittle cracking).

For this study, both dry and mortared stone masonry joints were considered. As dry joints don't have any cohesion, the tensile strength for gaping criterion is set to zero. For mortared joints, ranges of the tensile strengths up to the apex of the coulomb failure envelope are considered for parametric study.

3.4 Numerical Structural Capacity Assessment: Limit Analysis

In this section, an iterative limit analysis was carried out to find the best geometric dimensions of the prototype arch that can be accommodated within the drop-weight apparatus cell (see Figure 3.1). The analysis was carried out using non-commercial software RING 1.5, 2005. The software is based on the 'mechanism' method of analysis of rigid blocks. And it evaluates the limit strength and predicts the critical failure mode, from consideration of rocking and sliding stability of the individual blocks, group of blocks and as well as the entire structure.

The software needs the gravitational weight and frictional resistance at the interfaces to ensure the stability. Hence the following parameters were used as inputs for carrying out the assessment of the single arch prototype bridge.

Density: The gravitational forces, either self weight or superimposed weights are main sources of stabilizing forces by producing resisting moment against rocking and by producing normal thrusts at interfaces to mobilize frictional resistance. Only self weight of the arch was considered and evaluated from unit weight of granite stones,$\gamma = 24kN/m^3$ (Vasconcelos, 2005).The value is taken as a lower bound considering the coefficient of variation observed during the test.

Geometry: Thickness of the arch ring, rise and clear span of the arch. These values are varied to carry out the parametric study. Being limited by the floor plan dimensions of the impact test apparatus cell, clear spans of 1.0m, 1.2m and 1.5m were tried. The rise of the arch is fixed to be 0.4m so as to accommodate the arch within the rail frame of the impact

apparatus. And for the same reason, the out-of-plane thickness was taken as 200mm and the radial thickness were varied from 100mm to 160mm.

As it can be observed from Table 3.5, the limit strength of the arch increases with the increase of radial thickness and it decreases with reduction of the rise-to-span ratio. The external load is applied at quarter span. Increasing the thickness of the arch enhances the geometric constraints between block against rotation and it increases the interfacial contact (frictional) area. More over it plays additional role by increasing the stabilizing gravitational load.

The rise-to-span ratio affects the stress flow mode. Within geometric bounds of the prototype arch; the load transfer mechanism shifts from axial thrust to flexural mode. Correspondingly different critical failure modes are observed. For lower thickness, mostly the hinges are rotational as the flexural capacity is a function of thickness to the third order. With increase in thickness, the critical failure mode is accompanied by sliding hinges formed either below the loading point or at the arch-abutment interface opposite to the loaded half span [Figure 3.8].

Table 3.7 Influence of geometric proportions of a segmental arch on its limit strength.

H_A/L_A	Failure Mode	$Thickness\ [mm]$			
		100	120	150	160
0.4	$\Delta\lambda$	0.51	0.93	2.03	2.42
	Hinge type	4R	4R	3R+1S(A)	3R+1S(A)
0.333	$\Delta\lambda$	0.76	1.47	3.47	**4.28**
	Hinge type	4R	4R	3R+1S(Q)	**3R+1S(Q)**
0.267	$\Delta\lambda$	0.91	1.52	3.11	3.92
	Hinge type	4R	4R	4R	4R

$Coefficient\ of\ friction, \mu = 0.65\ and\ number\ of\ units\ =\ 13$

$R = Rotational\ hinge, S(Q) and\ S(A)\ Sliding\ hinge\ at\ quarter\ span\ and\ \ abutment\ respectively$

For this study an arch with, $\frac{H_A}{L_A} = 1/3$, and $t_A = 160mm$ was selected. As sliding occurs with significant post peak frictional resistance, the failure mode consisting rotational and sliding hinges is preferable. Moreover sliding hinge at the loading point is chosen over that of the arch-abutment interface. During sliding, the first type enables to close the rotational hinges to

some extent, while the later facilitates the gaping by increasing the span. Whereas for rotational hinges, once the arch attains its maximum potential energy, the post peak behavior is brittle as the single point contacts at the hinges can't resist any more rotation. The post peak frictional resistance, which is mobilized by sliding hinge formation at the loading point, results in a more stable mechanism than other types of failure mechanisms. The post peak behavior of such mechanisms can be seen from numerical and experimental results presented in Section 3.5

Frictional resistence: Among the frictional resistence parameters of joints, only coeficient of friction is considered by the software. Hence the capacity assesment based on this methdology is best adopted for dry joints, as cohesion plays amajor role in the over all capacity of the arch. To cover the infuence of interfacial frictional resistence on the capacity of the arch, both the coeficient of friction and number of joints were varied to evaluate the load factor and the crosponding failure modes. The ranges of friction coeficient, μ, was adopted as per the works of Vasconcelos, 2005. Where as the lower and uper bounds of the number of units was based on the consideration of units fabriction and dry jointed arch assemblege.

Table 3.8 Influence of friction and number of units on the limit strength of a segmental arch.

μ	Failure Mode	$Number\ of\ Units$				
		9	11	13	15	17
0.60	$\Delta\lambda$	3.31	3.35	3.39	3.1	3.07
	Hinge type	3R+1S(A)	2R+S(1A+1Q)	1R+S(2Q+1A)	3R+1S(A)	3R+1S(A)
0.65	$\Delta\lambda$	3.36	3.91	**4.28**	3.31	3.31
	Hinge type	4R	4R	**3R+1S(Q)**	4R	4R
0.69	$\Delta\lambda$	3.36	3.92	4.82	3.31	3.31
	Hinge type	4R	4R	3R+1S(Q)	4R	4R

$Radial\ thickness\ , t_A = 160mm\ \ and\ clear\ span\ of\ the\ arch, L_A = 1200mm[\frac{H_A}{L_A} = 0.333]$

$R = Rotational\ hinge, S(Q) and\ S(A)\ Sliding\ hinge\ at\ quarter\ span\ and\ \ abutment\ respectively$

As shown in Table 3.8, the decrease in coeficient of friction results in decrement of the interficial shear resisting forces of the joints. This fosters the formation of more sliding

hinges. Obviously, the peak resistence reduces, however the post peak performance depends on the location of the hinge that either favours closing or gaping of rotational hinges. As the values of friction coeficient is uncertain for the dry masonry stone joints, the ranges of values were considered for further parametric study using non-linear static analysis.

Loading : Both the magnitude (arbitrary) and distribution (point of application of the load) are required to evaluate the load factor,$\Delta\lambda$, as coefficient for the limit load. The magnitude of 1KN was used as basis and the crosponding load factors and failure modes were evaluated for each geometric and material parameters [Table 3.7 and Table 3.8]. The loading at the quarter span has been reported as one that gives the lowest load factor from the demand point of view. (Ramos, 2007). However, it can not be ensured that the quarter span as loading point results in the weakest mechanism formation for the prototype bridge selected for this study, as given in Table 3.9. Moreover the boundary conditions are assumed to be fixed. This assuption results in geometrical locking for the loading point at the mid-span.

Table 3.9 Influence of loading position on the limit strength of a segmental arch.

	Loading position to clear span ratio					
	1/10	1/6	1/4	1/3	5/12	1/2
$\Delta\lambda$	3.38	3.33	4.45	4.73	7.30	-
Failure mode	4R	4R	3R+1S(Q)	3R+1S(A)	2R+2S	Locking*

*Geometrical locking because of fixed boundary condition

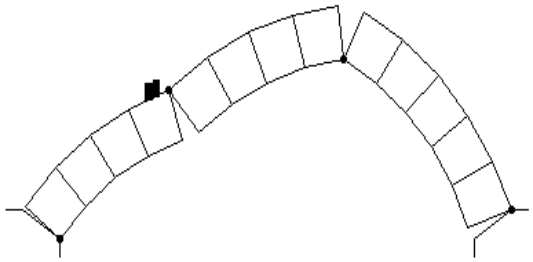

(a) Failure mode 4R

$[H_A/L_A = 0.267, \mu = 0.65, and\ \Delta\lambda = 3.92]$

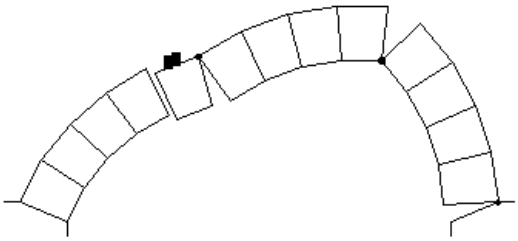

(b) Failure mode 3R +1S

$[H_A/L_A = 0.333, \mu = 0.65\ and\ \Delta\lambda = 4.56]$

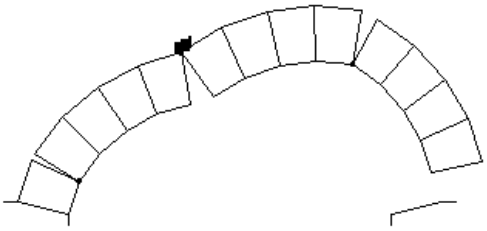

(C) Failure mode 3R+1S (A)

$[H_A/L_A = 0.4, \mu = 0.65\ and\ \Delta\lambda = 2.42]$

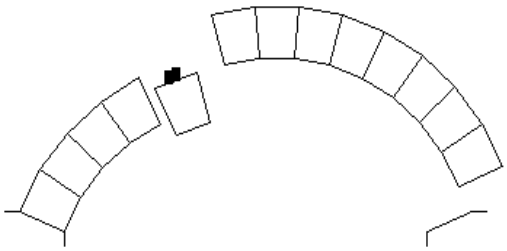

(c) Failure mode R+ S (2Q+A)

$[H_A/L_A = 0.333, \mu = 0.60\ and\ \Delta\lambda = 3.39]$

Figure 3.8 Failure mechanisms of dry jointed stone masonry arch predicted by Limit Analysis using RING 1.5.

3.5 Numerical Structural Capacity Assessment: Non-Linear FEA

The non-linear behaviour of the prototype arch under quasi-static loading was simulated using a finite element software package, (DIANA). A simplified discrete-crack finite element modelling approach has been adopted to model the non-linear quasi-static behaviour the arch. The model was developed using linear elastic plane stress elements for masonry units in conjunction with a contact interface elements for masonry joints.

A displacement based non-linear static analysis was carried out to predict the failure mode of the arch in advance of the experimental work. The results show similar failure mode as predicted by limit analysis. However the peak strength predicted using expected material properties doesn't match with that of the limit analysis. Hence a parametric study was carried out to see the sensitivity of the global response to fundamental properties of the joints

3.5.1 Structural Modeling

As the arch is two dimensional with constant out-of-plane thickness, and the loading is also in-plane, 2D finite element modelling was adopted.

Generally the non-linear behaviour of the stone masonry arches mainly accounted to the discontinuities at the joints. Except in areas of stress concentration, which may be due to localized concentrated loads, the stone blocks experiences compressive stress very much less than their compressive strength. Where as in tension zone, the joints crack in advance the stress reaches the tensile strength of the stones and this results in stress relief for the blocks. Hence it is reasonable to model the units to behave linear elastically and to model the joints explicitly using gapping failure criteria.

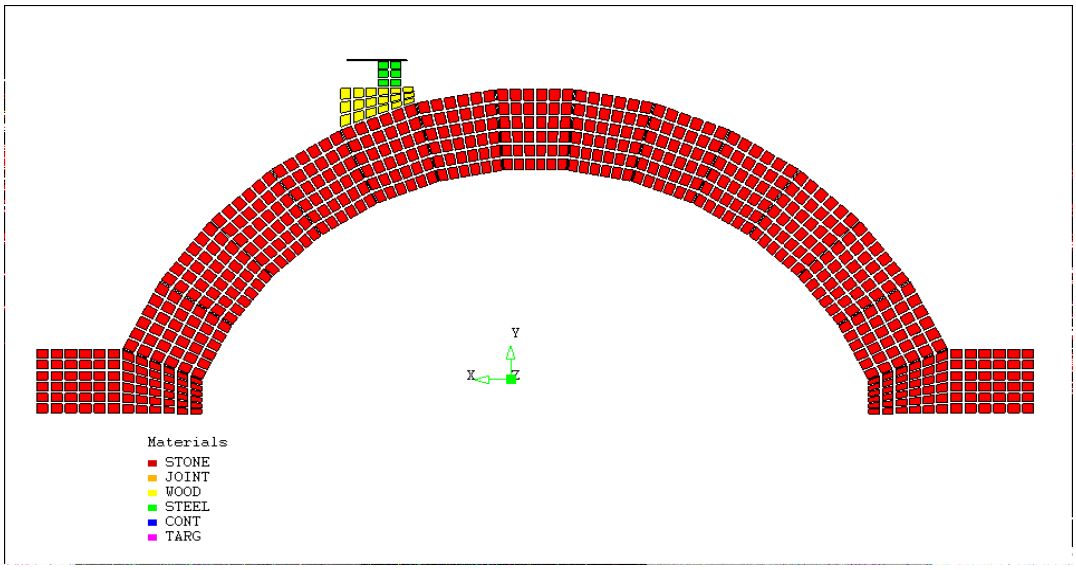

(a) Global model

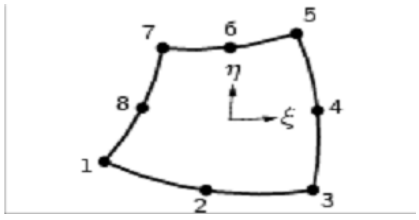

(b) Plane stress element [CQ16M]

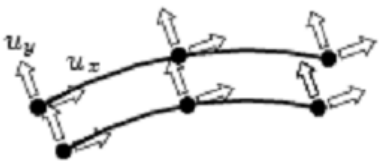

(C) interface element [CL12I]

(d) CL6CT

Figure 3.9 Global FM model of the prototype stone masonry arch for non-linear static analysis.

The arch-Units and Abutments: The stone units and abutments were modeled using a plane stress elements with a continuous and homogeneous material having a Young's modulus equal to 50 GPa, a Poisson coefficient equal to 0.2 and a mass density equal to $2400\ kg/m^3$. A 8-noded quadrilateral plane stress elements were used. These types of elements with mid-side nodes improves the convergence problem associated with the abrupt change of nodal forces as cracking (gaping) occurs (DIANA). The global finite element model is shown in Figure 3.9.

The Arch-Joints: 8-noded Interface structural elements were used to model the masonry joints. They have two translational degree-of-freedoms per node. These elements may have a dimension in their normal direction, i.e., a thickness. In this model, the thickness is zero and can be seen as black lines in the model, see Figure 3.9. They are modeled as area objects by giving a virtual thickness, a separation between units, and then shrink the thickness by rotational transformation. The modeling iDIANA commands are listed in Appendix A.

The interface elements are used to simulate a relation between the traction forces and relative deformations across the masonry joints. Inside the elastic compressive regime, see Figure 3.4, the governing constitutive relation for interface elements, is described by

$$\begin{Bmatrix}\sigma\\ \tau\end{Bmatrix} = \begin{bmatrix}K_N & \\ & K_t\end{bmatrix}\begin{Bmatrix}\delta u\\ \delta v\end{Bmatrix} \qquad 3.16$$

In which the normal traction, σ is perpendicular to the interface; the shear traction force, τ is tangential to the interface [Figure 3.4]. The linear effective stiffness of interface elements were formulated as discussed in Section 3.3.2.1 For tensile stress ranges, above the tensile strength of the joint, a gaping occurs and the corresponding stress in the adjacent nodes drops to zero. A dry jointed stone masonry arch was taken as the pilot model for discussion, and the formulated the properties of interface elements are given in Table 3.10.

Load cell: The global non-linear FE model was generated to simulate the laboratory set up (Figure 3.9). As discussed in Section 3.4, the external loads were applied at quarter span of the arch, and the load bearing units were explicitly modeled to represent the actual stress flow in to the arch. The steel bearing, which allows free rotation at the loading point, and the underlying wooden wedge, were modeled using linear elastic plane stress elements.

Table 3.10 Quasi-static Properties of interface elements for the pilot stone masonry arch bridge

Mesh size [no. of elements per edge of the unit], Ne	6
Effective unit stiffness, K_u	$4 * 10^{11} N/m^3$
Normal stiffness factor, β_k	0.01
Tangential stiffness factor,β_t	0.625
Cohesion, c_o	0.00
Tensile strength,f_t'	0.00
Coefficient of friction,μ_s	0.65
Dilatancy angle,φ	0.00

The interface between the loading jack and the steel bearing was modeled using three node contact element, with loading jack as a target and the steel bearing edge as a contacter. This explicit modeling of the loading cell was required to apply a displacement load to the target and gravitational load to the arch without any vertical restraint from the loading cell. More over the selection of the target (jack) and the contacter (steel bearing) components of the contact elements was based on the penetration requirement of contact algorithms. To ensure that inter penetrations are detected by contact algorithms, it is recommended that the interface component which is more rigid and have coarser element meshing should be assigned as target; whereas the more flexible part as a contacter. In this case the jack, which is modeled using a single element and fixed in the vertical direction to apply displacement loads, is taken as target.

Loads and Boundary Conditions: Both the right and the left abutments are fixed against the vertical and horizontal translations. And the loading jack is restrained from horizontal translations. Rigid beam constraint is applied at the top nodes of the steel bearing to make sure that these nodes experiences the same penetrations during displacement loading from the jack.

A gravitational load is applied to the entire arch. As the arch is fully modeled this load is specified as base acceleration, g = 9.81 m/s. For the force based, non linear analysis, a uniform pressure, $q = 94644 N/m^2$, at the interface between steel bearing and wooden wedge was applied.This pressure is equivalent to the peak load, $p_{peak} = 4.28 kN$, predicted by limit analysis. For displacement based analysis, a pre described vertical deformation load

of 1mm was applied in the down ward direction on the nodes representing the jack (target element). The loads are summarized in Table 3.1

Table 3.11 Quasi-static loads applied to FE model of the prototype arch

Load Case	Type	Value
LC1	Self weight	-9.81m/s2 (y)
LC2	Load cell Pressure	-94644N/m2 (y)
LC3	Load cell Deformation	-0.001m (y)

3.5.2 Structural Analysis

A non linear static analysis was carried out to derive the quasi-static capacity curve of the arch. Both the displacement based and displacement based approaches were carried out.

For the force based analysis, the self weight was applied in a single step, and the pressure load was applied with step sizes fixed automatically by adoptive loading algorithms involving arc-length scheme (DIANA). In this analysis case the contact elements are removed from the model as they are relevant

In the displacement based analysis case, the self weight was applied in advance to get stabilizing pre-compression stress against shear sliding failure of the joints. This load is totally carried by the arch, not transferred to the supports at the loading cell, as the contact elements are don't transmit tensile stress. After preloading with self weight, the deformation load was applied in step sizes determined by energy based iterative algorithms. Both the command and the input data files are included in the Appendix B.

Both simulation approaches tries to represent a monotonically increasing load applied until the collapse. Both approaches predict the same peak load and the pre-peak behavior. However the later approach was successful to predict the post peak behavior.

3.5.3 Results and Discussion

The results of numerical simulation of the pilot model, with material properties and loading conditions described above, will be presented.

Figure 3.10 shows the capacity curve of the arch obtained by the displacement based non-linear analysis. The arch peak strength of the model is only 64.4% of the value estimated

through the limit analysis. This deviation may arise due to the basic assumptions of each methodology and the material properties used for the models. The same friction coefficient and unit weights of the stone units were used in both models. However the basic assumptions in simulating the behavior of joints are different. In limit analysis the blocks were assumed to be rigid and the interfaces of such rigid blocks don't interpenetrate. However in the FM model, the interfaces are assumed to be flexible to an extent where convergence problem won't arise. In this model the interface stiffness was taken as 1% of the effective normal stiffness of the solid units. In both cases the tensile strength and the cohesion was ignored. Hence the possible cause of the variation may be accounted to the stiffness parameters of the joints and a sensitivity analysis was carried out and presented in Section 3.7.

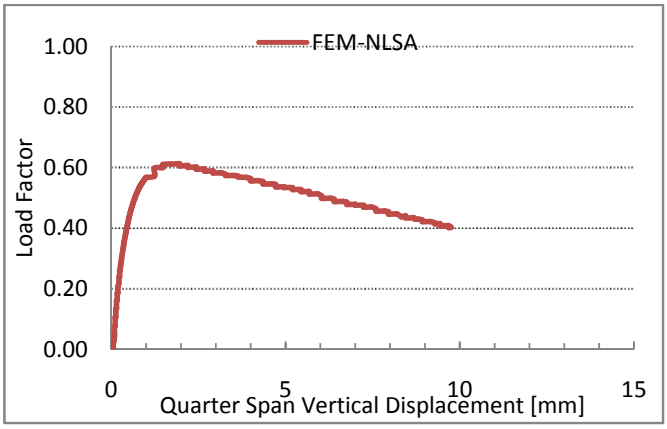

Figure 3.10 Quasi-static capacity curve of the pilot proto type arch, predicted by FEA

The other parameter between the two formulations is the strength and the elasticity of the stone blocks. In limit analysis, the block is assumed rigid and infinitely strong. In the FE model, the blocks were modeled using linear elastic material property, with Modulus of elasticity equal to 50Gpa. However, the stresses generated in the blocks are very small that hardly contributes to the global deformation. As shown in Figure 3.11 Vector plots of the principal stress flow in the dry jointed masonry arch.Figure 3.11 , the magnitude of the maximum principal Cauchy stress (compression) is 1.84Mpa which is very much less than the compressive strength of the units, see Section 3.3.1

Regarding the failure modes, both limit and FE model predict the same failure mechanism. The arch mechanism is formed with the appearance of 3 rotational hinges and one sliding hinge. For better impression of the behavior of the arch model, contour plot of the effective

Von Miss's stresses and the vector plot of the principal stresses and normal interfacial stresses are plotted over the deformed shape of the arch. The Figures give peak compressive stresses at each level of deformation.

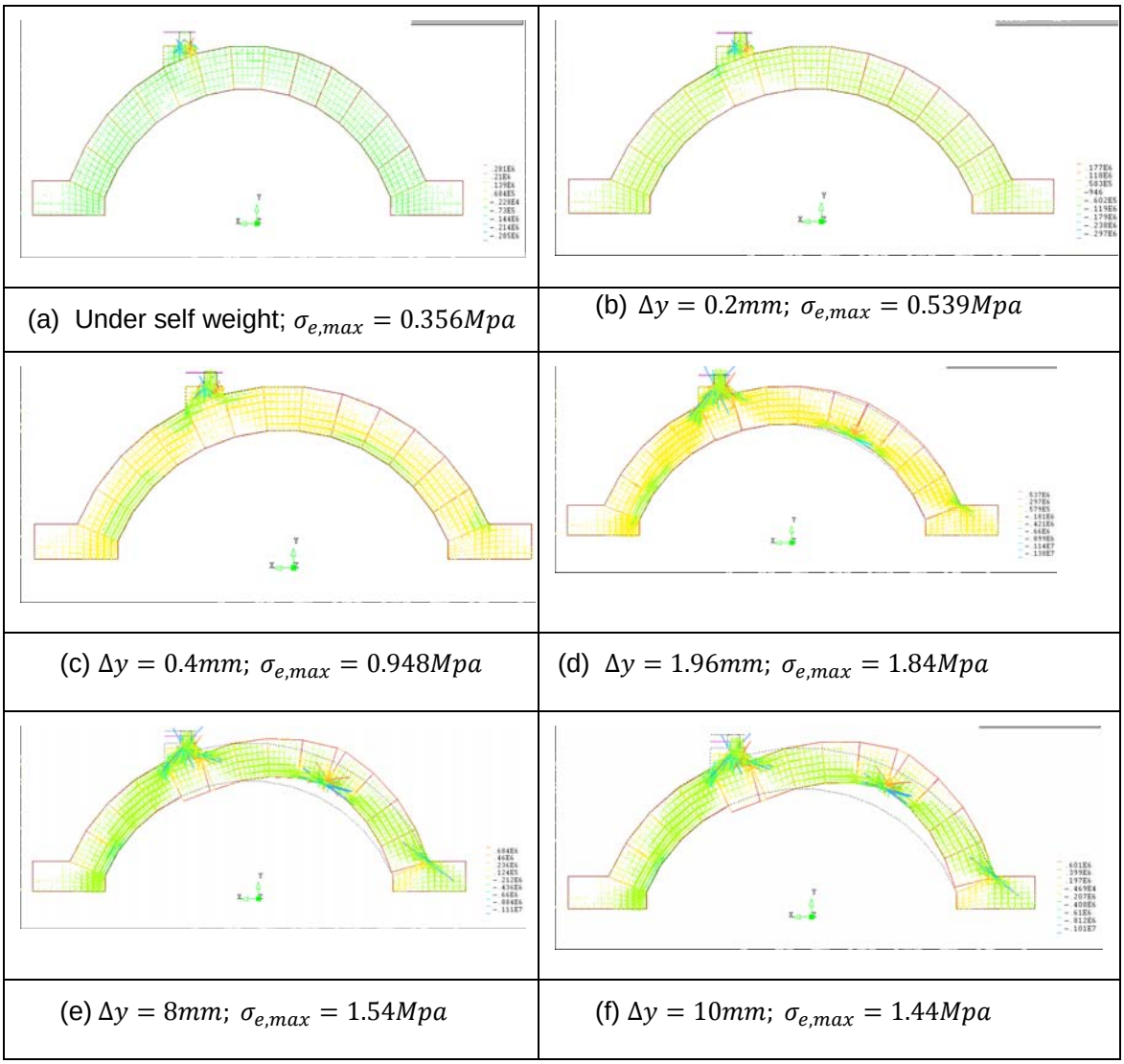

(a) Under self weight; $\sigma_{e,max} = 0.356Mpa$

(b) $\Delta y = 0.2mm;\ \sigma_{e,max} = 0.539Mpa$

(c) $\Delta y = 0.4mm;\ \sigma_{e,max} = 0.948Mpa$

(d) $\Delta y = 1.96mm;\ \sigma_{e,max} = 1.84Mpa$

(e) $\Delta y = 8mm;\ \sigma_{e,max} = 1.54Mpa$

(f) $\Delta y = 10mm;\ \sigma_{e,max} = 1.44Mpa$

Figure 3.11 Vector plots of the principal stress flow in the dry jointed masonry arch.

The arch attains its peak strength at 1.96mm. In each figure, two stress plots in pre-peak and post-peak regime of the arch are included in addition to that of the peak and self weight.

Figure 3.11 shows the vector plot of principal Cauchy stress overlapped on the deformed shape of the arch. The plot gives the qualitative variation in the stress flow in the arch as the

arch deforms accompanied with rotational and sliding hinge formation. Under self weight alone, the stresses are flowing to the support almost uniformly.

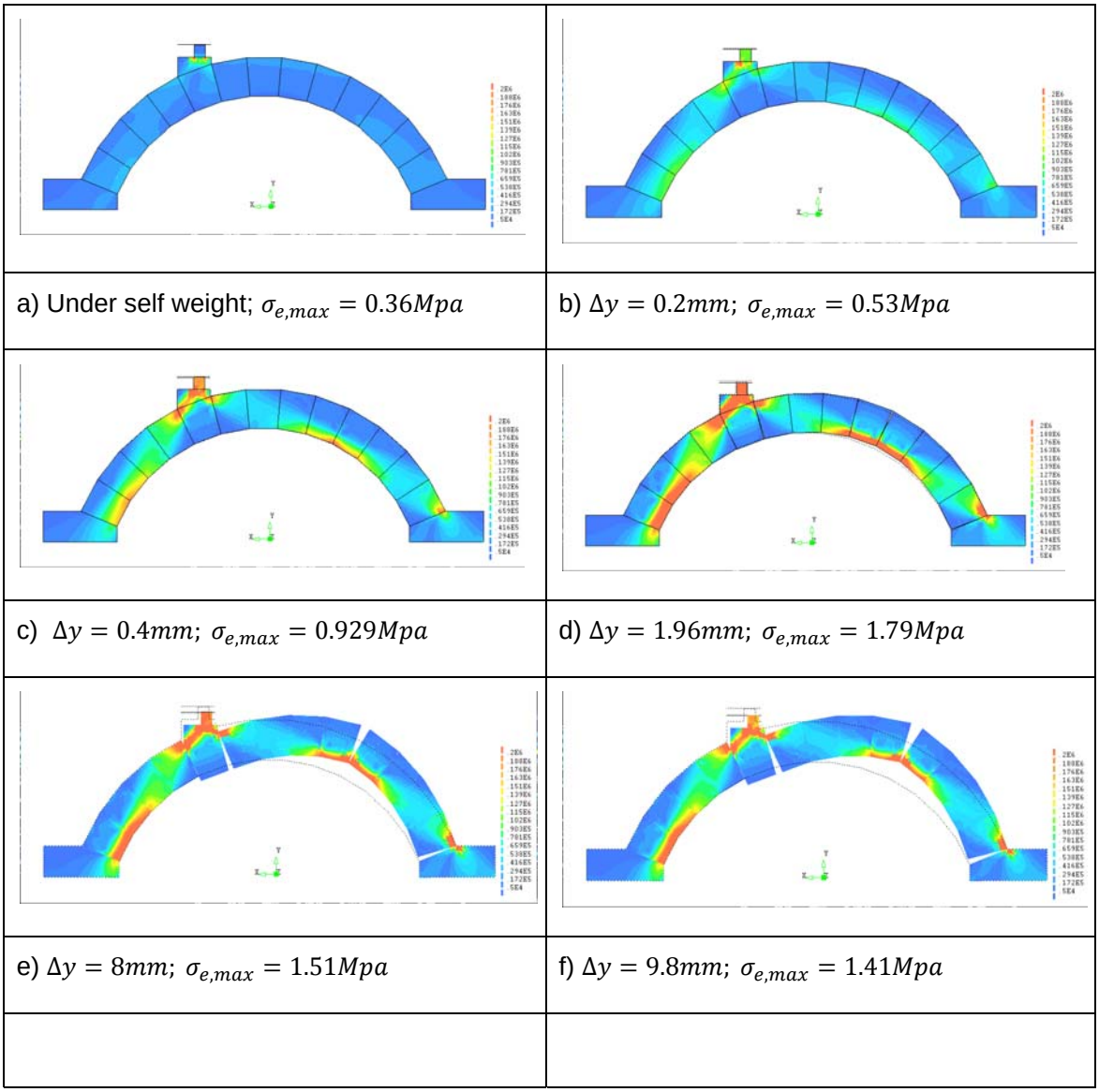

a) Under self weight; $\sigma_{e,max} = 0.36Mpa$

b) $\Delta y = 0.2mm;\ \sigma_{e,max} = 0.53Mpa$

c) $\Delta y = 0.4mm;\ \sigma_{e,max} = 0.929Mpa$

d) $\Delta y = 1.96mm;\ \sigma_{e,max} = 1.79Mpa$

e) $\Delta y = 8mm;\ \sigma_{e,max} = 1.51Mpa$

f) $\Delta y = 9.8mm;\ \sigma_{e,max} = 1.41Mpa$

Figure 3.12 Contour plots of the effective stresses in the dry jointed masonry arch.

As it can be seen in Figure 3.13 at displacement of 0.2mm, the first hinges appear in the intrados just below the loading point. The unit, at which the load was applied, loses its contact from adjacent blocks in the intrados side. With further loading the units on the right side quarter span lose contact on the extrados edge. And then one predominate rotational hinge is formed, on the same side, together with rotation a hinge at the right abutment, in

which gaping appears in the intrados side. When the gapping in the two right side hinges increases, sliding hinge appears below the loading point. The appearance of this hinge prevents the sudden collapse, by stabilizing the thrust from coming out side of the arch.

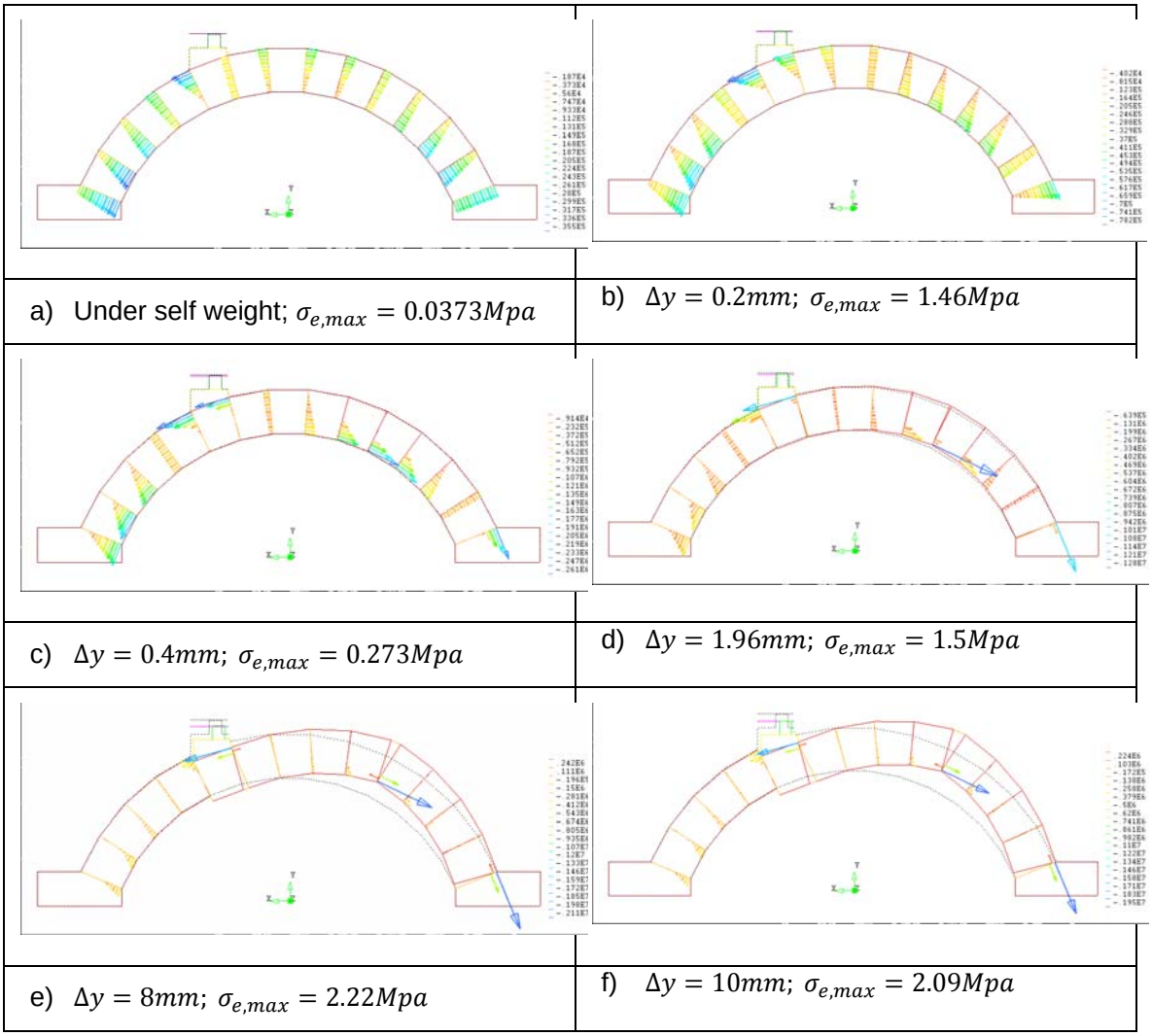

a) Under self weight; $\sigma_{e,max} = 0.0373Mpa$

b) $\Delta y = 0.2mm;\ \sigma_{e,max} = 1.46Mpa$

c) $\Delta y = 0.4mm;\ \sigma_{e,max} = 0.273Mpa$

d) $\Delta y = 1.96mm;\ \sigma_{e,max} = 1.5Mpa$

e) $\Delta y = 8mm;\ \sigma_{e,max} = 2.22Mpa$

f) $\Delta y = 10mm;\ \sigma_{e,max} = 2.09Mpa$

Figure 3.13 Vector plots of the normal interfacial stresses of dry jointed masonry arch..

In General the FE simulation predicts a ductile failure mode of the arch. Based on this pilot model, it has been found that the arch can withstand peak load of 2.62kN and can deform to 10mm vertically down ward at the loading point without collapse. More over the arch can absorb an equivalent energy of 255J

3.6 Experimental Structural Capacity Assessment

To calibrate the results from the non-linear static analysis, and to estimate the amount of energy that can be absorbed by the arch reliably, a quasi-static experimental test was carried out on the prototype arch. The test was carried out in the civil engineering department laboratory, University of Minho. The results of the test conform well to the results of the FE simulation. The testing procedure and the corresponding results are presented in the following sections.

3.6.1 Experimental Set Up

The arch was assembled on a reaction steel frame, made of the I-section steel girders. The girders are 45cm deep and well braced, which makes it much stronger and stiffer that the arch specimen. Hence it was believed that the frame can provide sufficient lateral and vertical constraint.

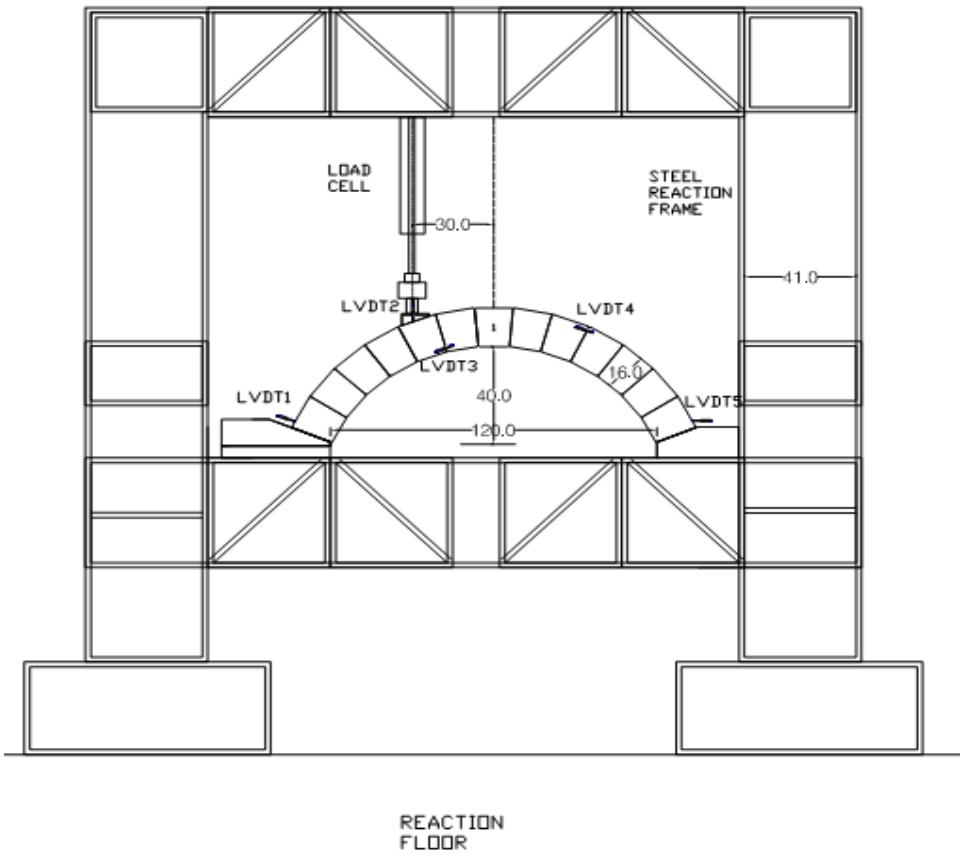

Figure 3.14: Quasi-static experimental test set up

As a dry joint stone masonry arch, the construction was carried out using a formwork that fits the intrados of the arch. The assembling of the units starts from left and right abutments, and then stacking each unit one by one up to the key stone. Finally the key stone was driven in between the right and the left rings of the arch using a hammer. Note that the abutments are well restrained laterally against the reaction frame as shown the in Figure 3.14Figure 3.14.

Once the arch was constructed, a wooden bearing, with horizontal width of 11cm, out of plane thickness of 200mm, and a height (on the left) of 50mm, was glued to the fifth stone block using rapid hardening epoxy resin adhesive. The wooden wedge was placed in such way that it coincides with the location of the quarter span (300mm from the center line of the arch). More over a steel bearing, with a roller at the top, was placed over the wooden wedge. This enables to make sure that no rotational restrain exists between the arch and the loading cell.

Finally the loading cell (actuator) was positioned at the quarter span of the arch; and a total of five external displacement transducers, LVDTs, were set on the arch to measure the deformations. The first and the fifth LVDTs were planned to measure the sliding at the abutment arch interfaces. And LVDT2 was used to measure deformation at the loading point. Whereas the third and fourth were positioned to measure the opening at the rotational hinges on the left and right quarter span.

3.6.2 Test Execution

A single test was carried out on dry jointed masonry arch. The actuator and the LVDTS were connected to a data acquisition system and calibrated. After calibration, a displacement controlled load was applied at a rate of 0.005mm/s, see Figure 3.15.The adoption of this rate of loading was on the basis of attaining a stable progressive damage of the arch. More over photographs and videos were taken to capture deformation progress of the arch. The test takes 2361s to let the arch deform a vertical displacement of 12mm.

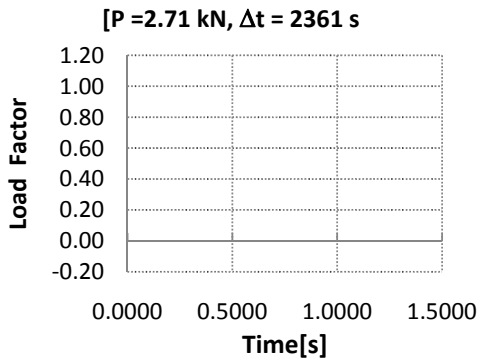

(a) Actuator load history

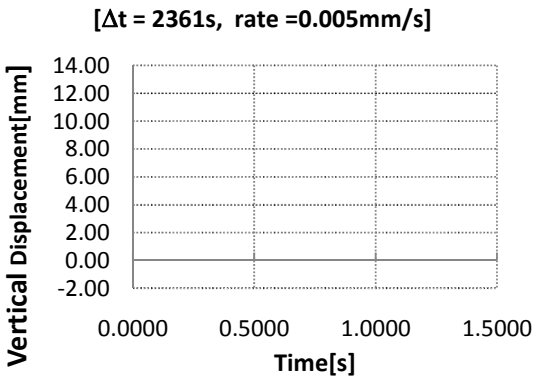

(b) Actuator displacement history.

Figure 3.15 Experimental quasi-static Loading History

3.6.3 Results and Discussion

As discussed above, the vertical deformation at loading point was recorded using an external LVDT as well as by internal transducer which is integrated with the actuator. The arch was found to carry a peak load of 2.71kN and was able to deform quasi statically (at a rate of 0.005mm/s) to 12 mm without collapse, until the peak strength is reduced by 35%.Figure 3.17 shows the ultimate deformation just before the test halted. These values are in agreement with FE simulation results and will be discussed in the next Section.

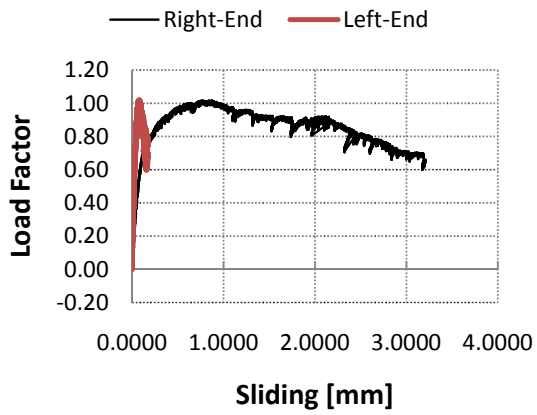

(a) Sliding at arch-abutment interfaces

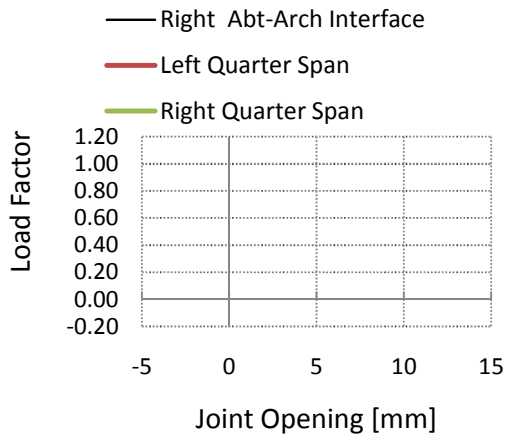

(b) Gaping at rotational hinges

Figure 3.16 Sliding and rotational gaping at the critical hinges of observed during quasi-static experiment

The failure mechanism observed during the experimental test was identical to that predicted by limit analysis and the FE nonlinear analysis. Three rotational hinges and one sliding hinge were prominently observed at the same location as that of the numerical simulation. Two rotational hinges centered at the extrados and intrados of the left and right quarter span, one rotational hinge at the right arch-abutment interface, and one sliding hinge at the left quarter span below the loading point, see Figure 3.17. At the right side abutment, the sliding was more than that of the left side as the thrust force predominantly goes to the nearby support, which in turn gives greater sliding resistance. The openings of the left quarter rotational hinges, stops at around 3.5mm, this discrepancy is due to the threshold limits of the transducer, A maximum of 10mm opening was measured at the right quarter span hinge. It should be noted that the opening measurements are presented here to see relative deformation, as the transducers were not accurately fixed at the opening edges parallel to the direction of flow.

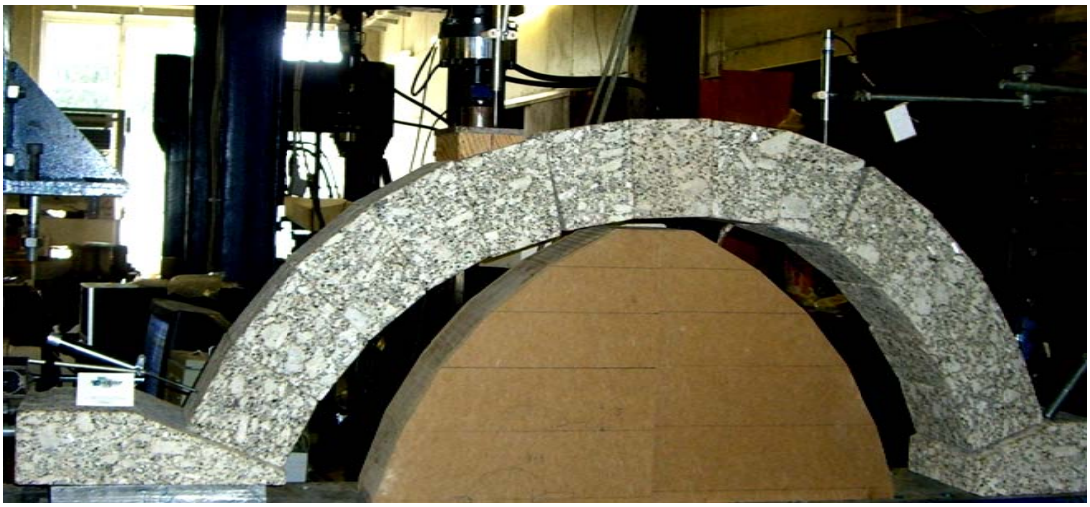

(a) Deformed arch at the ultimate displcement ($\Delta y = 12mm$)

(b) Left abutment-no opening

(c) Hinges at the left quarter span

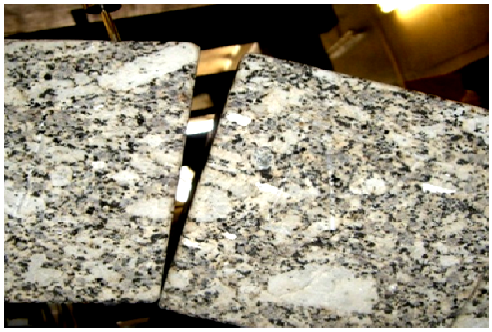

(d) Hinge at the right quarter span

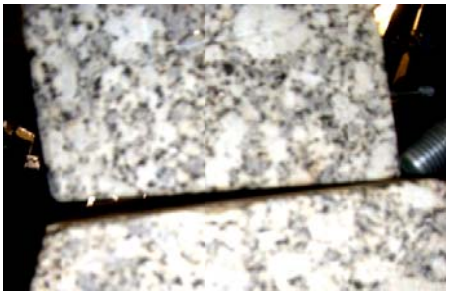

(e) Hinge at the right abutment

Figure 3.17 Deformation of a stone masonry arch under quasi-static loading (Experimental)

3.7 Validation of Structural Models

It has been found that the results of limit analysis significantly vary from that of the FE and experimental result. Hence parametric study was done to see the possible causes of the difference. As the geometrical configuration and inertial properties were the same for both simulations; parameters that affect the pre-peak flexibility and post peak behaviour are considered. This includes the elasticity of the units, the stiffness of the joints and the shear strength parameters of the joints. It has been found that, for dry jointed stone masonry arch, the stiffness of the joints greatly influences the peak strength as well as the pre-peak stiffness of the arch.

3.7.1 Sensitivity of the Response to Pre-Peak Stiffness Parameters

The pre-peak stiffness and the peak strength of an arch depend on the elasticity of the units, the stiffness of the joints and the rigidity of the support. The modulus of elasticity of the reaction frame is about four times that of the arch, the depth of the members of the frame are almost three times the thickness of the arch with a comparable span range, and more importantly, the small stresses level are transmitted to the rigid frame joints. This condition enables to make the assumption that the supporting frame is rigid (non-deformable under the given loading condition) and it doesn't affect the result. Hence the discrepancy between the results is solely accounted by flexibility of the joints and modulus of elasticity of the joints.

3.7.1.1 Effect of Modulus of Elasticity of Stone Blocks

The modulus of elasticity of granite stones from Guimares ranges from 35Gpa to 55Gpa, as discussed in Section 3.3.1. The modulus off elasticity affects the stiffness of the global structure directly or indirectly in two ways. Primarily it affects the deformability of the units and secondly it also affects the stiffness of the joints (Equation 3.10). As discussed above in Section 3.5.3, the peak concentrated stresses in the pre-peak regime are less than 1Mpa where as the value rises to maximum of 2Mpa Figure 3.12. Both of which are very small to produce strains which are significant for the total deformation. Hence a value of 50Gpa was taken as the same for all the models, and the interface stiffness factor was taken as an important parameter for the study.

3.7.1.2 Effect of Joint Interfacial Stiffness

As discussed in Section 3.3.2.1, selection of the normal and the tangential stiffness values for interface elements depends on the problem at hand and the associated convergence problem during numerical simulation.

If the problem involves interfaces which are perfectly smooth and with no expected localized surface crushing, zero width (thickness) interface elements with infinite stiffness to avoid interpenetrations. However this affects the convergence of the equilibrium iterations due to sudden change of nodal forces as the gaps arise. Secondly nothing is perfectly smooth and free of surface irregularities which are easily damageable, as in the case of stone masonry units. Hence either interface elements of with a finite size and reduced stiffness or zero thick interface elements with an allowance of interpenetration should be used. In this study, the later approach is adopted. That means the stone blocks can interpenetrate in compression

zone and for a gap in the tension zone. The influence of the weak zone of joints (or joint size) is indirectly accounted by the joints stiffness factor,β_k,(Equation 3.12)

It has been shown in Table 3.5 that values of ,β_k, for granite stone joints vary from 0.07 to 2.67.However from penalty stiffness formulation approach, the stiffness should be less than or equal to the stiffness of the underlying finite element to convergence problem, more over shouldn't be taken too much small to limit inter penetration. A penalty factor of 0.1 is usually recommended (DIANA) (Hallquist, 1998) (ANSYS).Here in this study 6 8-noded plane elements were used to mesh a stone unit. Hence the stiffness factor should vary from 0.6 to 6.

<table>
<tr><td> 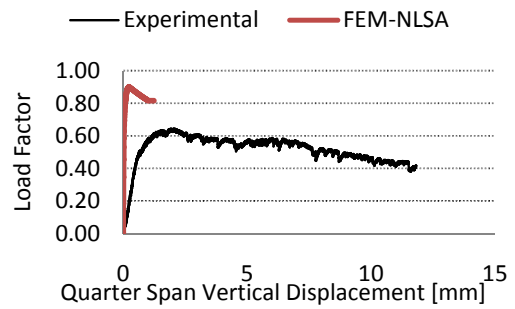
</td><td> 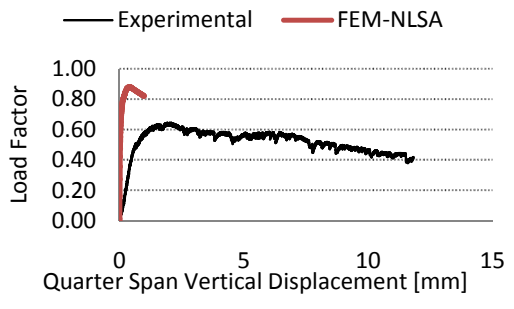
</td></tr>
<tr><td>$(a)\beta_k = 1.0\ \lambda_{FEM} = 0.902$</td><td>$(b)\beta_k = 0.25\ and\ \lambda_{FEM} = 0.881$</td></tr>
<tr><td> 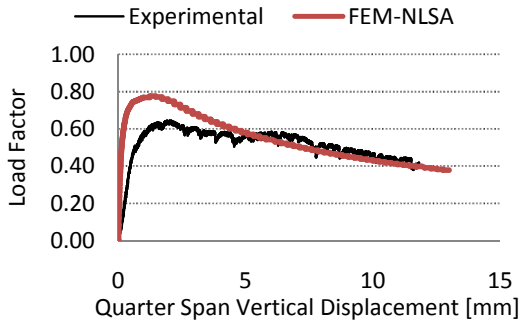
</td><td> 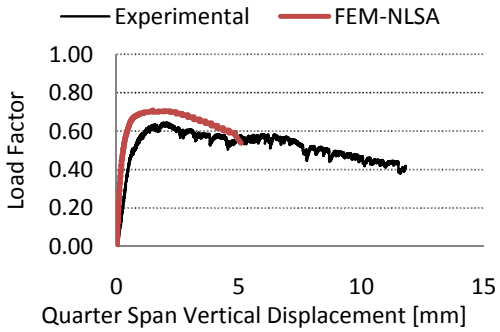
</td></tr>
<tr><td>$(c)\beta_k = 0.05 and\ \lambda_{FEM} = 0.776$</td><td>$(d)\beta_k = 0.02\ and\ \lambda_{FEM} = 0.825$</td></tr>
</table>

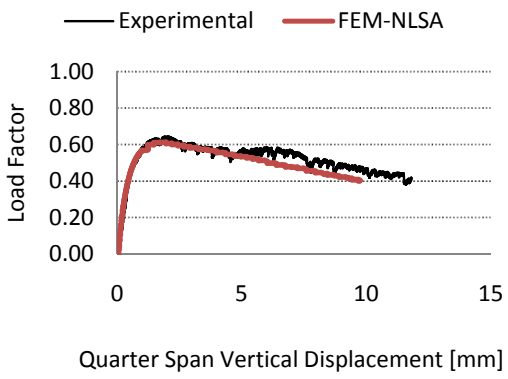

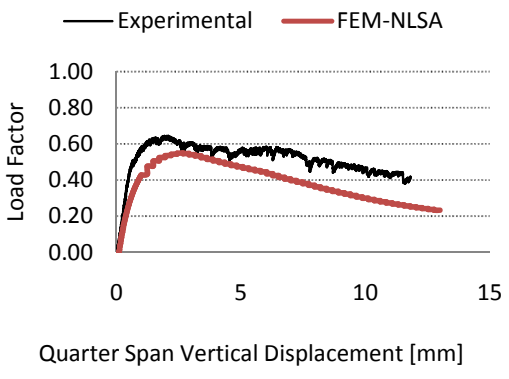

$(e)\beta_k = 0.01\ and\ \lambda_{FEM} = 0.613$	$(f)\beta_k = 0.005\ and\ \lambda_{FEM} = 0.550$
$P_{peak} = 4.28kN; \lambda_{EXP} = 0.644\ and\ \mu = 0.65$	

Figure 3.18 Effect of the interface stiffness on the quasi-static capacity assessment of a dry joint stone masonry arch

Hence the value , β_k, was varied from 1 0 to 0.005 and the results are shown in Figure 3.18 It was found that with the increase of the interface stiffness, both the strength and the pre-peak stiffness of the arch enhances. However the best matching performance curve to that of the experimental was found when β_k was taken as 0.01.That means when the interfaces elements are assigned a stiffness value 1% of the effective compressive stiffness of the stone units. Both the peak strength (5% difference) and the post-peak behaviour are in good agreement.

However the value of the stiffness factor which matches the experimental and the FE simulation results in a big difference in the peak strength estimation by limit analysis using RING. When a higher interface stiffness value is used, the result matches with that of the limit analysis, which is in agreement with rigid block assumption-no penetration between the block. That is the units are allowed either to slide or rotate as a rigid block. However in stone masonry construction, perfect interfaces are likely to find. For instance the units in of the arch specimen considered in this study are machine-sawn which are more or less smooth. Hence this rigid interface assumption in limit analysis should be taken with caution as it results an overestimated capacity of arches.

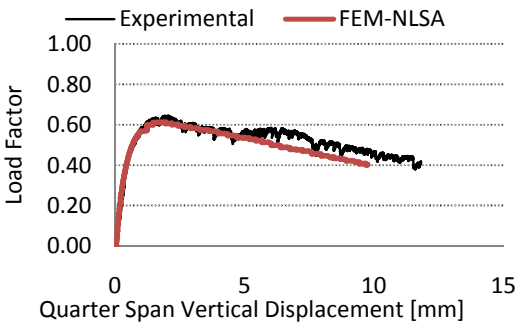

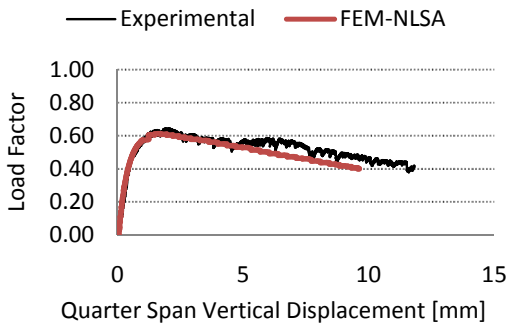

$(a)\beta_t = 0.625\ and\ \lambda_{FEM} = 0.613$	$(b)\beta_t = 1.0\ and\ \lambda_{FEM} = 0.612$
$P_{peak} = 4.28kN; \lambda_{EXP} = 0.644\ and\ \mu = 0.65, \beta_k = 0.01$	

Figure 3.19 Effect of the interface stiffness on the quasi-static capacity assessment of a dry joint stone masonry arch

The other possible case that can be considered to influence is the ratio of the tangential to the normal stiffness ratio. Usually an equal stiffness for both the normal and shear tractions is considered ((DIANA) (ANSYS). The other alternative is to formulate the shear stiffness of the joints in proportion to the shear modulus of elasticity. Both approaches were considered and brought no significant difference as shown in Figure 3.19

3.7.2 Sensitivity of the Response to Post-Peak Strength parameters

In addition to the pre-peak strength parameters, the post peak strength parameters may affect the result. In this prototype study, the units are assumed to behave elastically and hence the post peak parameters are those of the stone unit interface properties only. So both cohesion and coefficient of friction are considered. Actually in this study a dry jointed stone masonry arch was tested experimentally, but the numerical simulation was carried out to see how much application of cohesive binders (mortar joints) enhances the capacity of the arch. Both these issues are discussed in the following sub sections.

3.7.2.1 Effect of Joint-Interfacial Friction Coefficient

It has been reported the coefficient of friction for dry jointed masonry to vary from 0.6 to 0.69 as shown in Table 3.6. Hence the non-linear FE analysis was carried out for three values (0.60, 0.65, and 0.69) and the results (Figure 3.20) show that the capacity curve of the arch is almost independent of the selection of the friction coefficients within the specified rage.

However taking the lower bounds enhances the post-peak prediction where as the upper bounds enables better prediction of the peak strength. Peak load factors differ from the experimental value by 3% and 12% respectively.

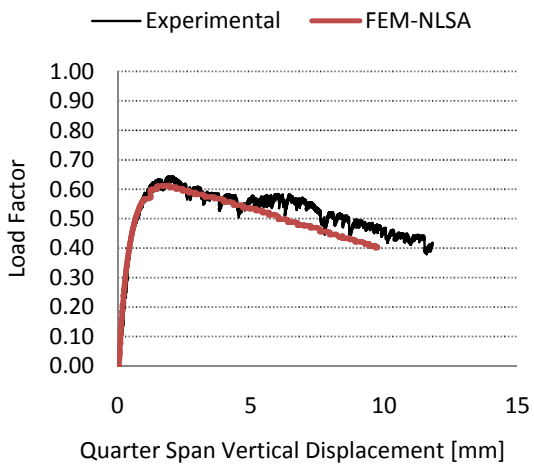

$(a)\mu = 0.69\ and\ \lambda_{FEM} = 0.623$

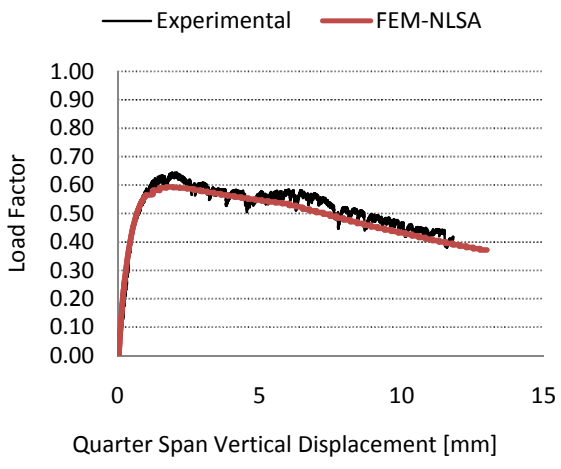

$(b)\mu = 0.60 and\ \lambda_{FEM} = 0.564$

$(c)\beta_k = 0.01; \beta_t = 0.625\ and\ \lambda_{EXP} = 0.644$

Figure 3.20 Effect of coefficient of friction on the quasi-static capacity assessment of dry jointed masonry arch.

3.7.2.2 Effect of Joint-Interfacial Cohesion

The application of adhesive binder in the joints significantly changes the quasi-static performance the stone masonry arch. Here in this study the thickness of the interface elements was taken as zero in the model. However the reduced joint stiffness was taken, which may indirectly accounts the presence of the mortar joints as illustrated in Equation 3.12.

It has been reported from the work of Vasconcelos that the cohesion of mortared stone masonry joints (lime based mortar) is in the neighbourhood of 0.35Mpa. And it has been deduced from the same document that values of $\beta_k$for mortared joints to be 0.07, which is much higher than 0.01. So as mortared jointed masonry are softer than the dry jointed masonry, the later value was adopted for the parametric study.

As shown in Figure 3.21, the initial pre-peak stiffness doesn't change with cohesion rather the peak strength and the post-peak behaviour drastically changed. The strength of the masonry increases with cohesion. Once the peak strength is attained, the capacity curve snaps down to that of the dry jointed arch. More over the failure mechanism is changed to the four rational hinges. The fourth rotational hinge is formed on the right abutment with gapping on the extrados edge.

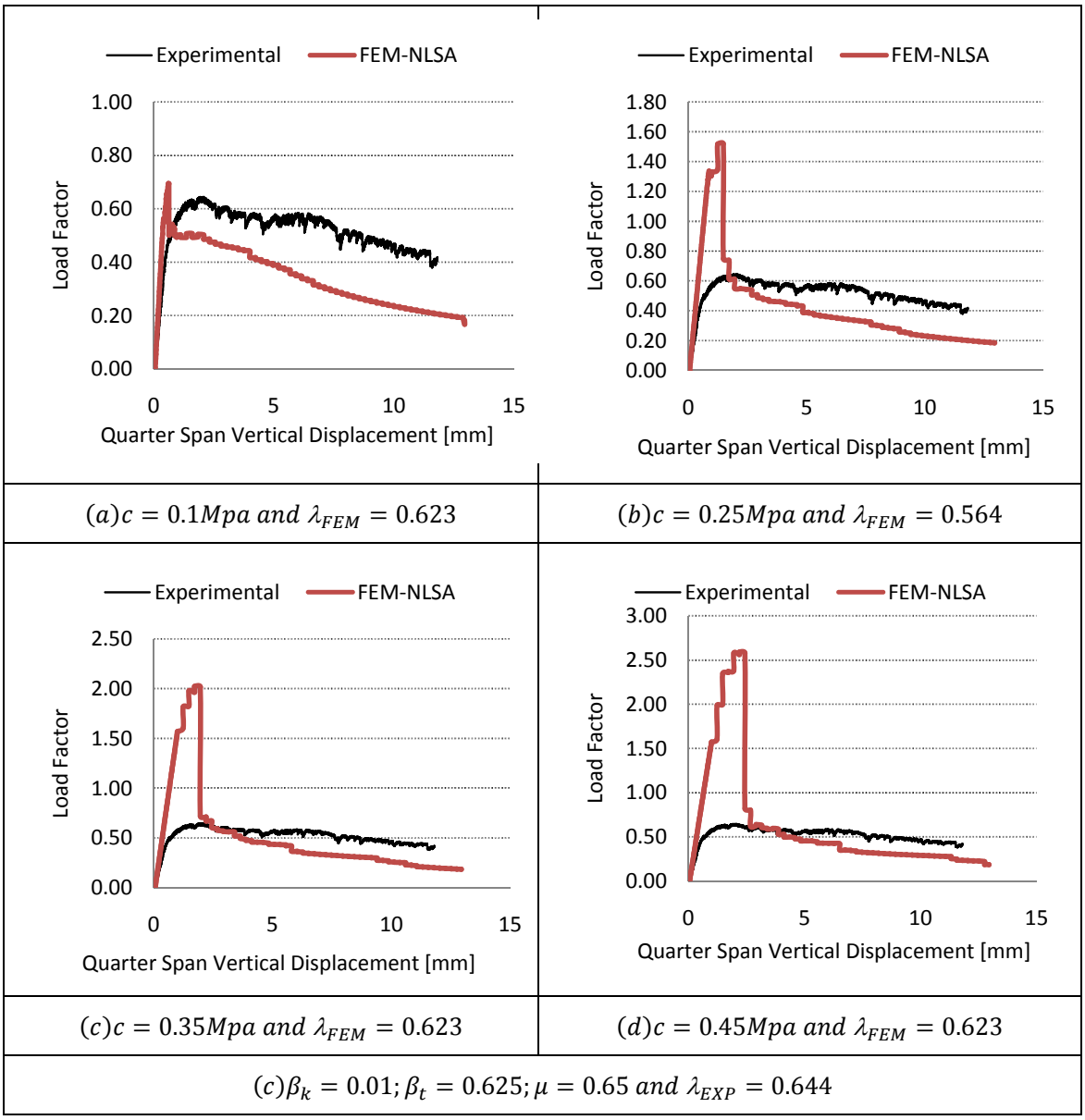

Figure 3.21 Effect of cohesion on the quasi-static capacity of stone masonry arches.

CHAPTER 4

IMPACT PERFORMANCE OF STONE MASONRY BRIDGES: SINGLE SPAN ARCH

4.1 General

Blast and impact loads arise from interactions of systems that occur at very high rate. The interaction involves contact between the systems and results in the transmission of kinetic energy from one body to the other. These interactions induce a very high strain rates (loading rates), which are highly transient and impulsive, in the target structures (one of the interacting systems). However the first load type arises when a very fast moving blast air engulfs the structure where as the second loading phenomenon occurs when a fast moving projectile hits the structure.

To characterize the performance of stone masonry arches at high rate loading, a single span stone masonry arch was assessed both experimentally and numerically for impact loading. The prototype arches were tested experimentally using a drop weight apparatus. The numerical simulation was carried out using an explicit dynamic analysis software LS-DYNA. Finally a calibration of the numerical model was calibrated using the experimental results.

4.2 Dynamic Material Properties

Impact and blast loads typically produce very high strain rates in the ranges of $10^0 - 10^2 s^{-1}$ and $10^2 - 10^4 s^{-1}$ respectively. The approximate ranges of the expected strain rates for different loading conditions are shown in the Figure 4.1. It can be observed that ordinary static strain rate is located in the range of $10^{-6} - 10^{-4}\ s^{-1}$, where as dynamic loads yield strain rates in the range: $10^{-3} - 10^4\ s^{-1}$.

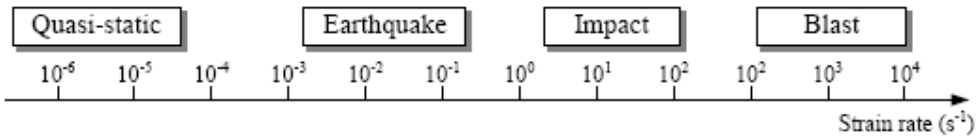

Figure 4.1 Strain rates of different loading conditions.

This high straining (loading) rate would alter the dynamic mechanical properties of target structures and, accordingly, the expected structural performance of various structural elements. The strength enhancement of structures at high rate loading with that of the quasi static loading conditions is referred as Dynamic enhancement factor (DIF). For masonry structures subjected to this high rate loading, the strength of the units and the joints can increase significantly due to strain rate effects.

4.2.1 Properties of Stone Blocks

The mechanical properties of stone blocks under dynamic loading conditions can be quite different from that under static loading. For this study, DIF for stiffness or strength of granite stones have not been found. However it can be well predicted from that of concrete and brick.

For concrete, It has been reported that while the dynamic stiffness does not vary a great deal from the static stiffness, the stresses that are sustained for a certain period of time under dynamic conditions may gain values that are remarkably higher than the static compressive strength (NGO, Mendis, Gupta, & Ramsay, 2007).Strength magnification factors as high as 4 in compression and up to 6 in tension for strain rates in the range : $10^2 - 10^3\ /sec$ have been reported for concrete.

Based on dynamic uniaxial compressive tests conducted to study the strain rate effect of brick, the dynamic increase factor (DIF) for strength of brick material was formulated as (Wei & Hao, 2009):

$$DIF = \begin{cases} 0.0268 ln\dot{\varepsilon} + 1.3504 \; for \; \dot{\varepsilon} \leq 3.2 s^{-1} \\ 0.2405 ln\dot{\varepsilon} + 1.1041 \; for \; \dot{\varepsilon} > 3.2 s^{-1} \end{cases} \qquad 4.1$$

Hence for impact loading conditions, which have strain rate range of $10^0 \; to \; 10^2$, DIF for strength of brick varies from 1.37 to 3.5. Based on the argument discussed in Chapter 3 and DIFs reported for brick and concrete, we can model the stone blocks to behave linear elastically with quasi-static modulus of elasticity.

4.2.2 Properties of Dry-Joint Stone interfaces

In the simulation of masonry joints using the explicit finite element code LS-DYNA3D, the interfaces are represented using specialized contact surface formulations. Dry joints are simulated using surface to surface contact formulations and mortared joints are simulated using tied surface to surface formulation. Both formulations are based on Mohr Coulomb failure criteria as discussed in Chapter 3 with two exceptions.

Primarily the softening of friction coefficient depends on the relative velocity of the surfaces in contact, in which the peak coefficient of friction is referred as static coefficient of friction and the residual friction coefficient as dynamic. Typically, the static coefficient of friction is higher than the dynamic coefficient of friction. ANSYS provides the following exponential decay friction model (see Figure 4.2):

$$\mu = \mu_d * \left(1 + \left(\frac{\mu_s}{\mu_d} - 1\right) e^{-D\dot{v}}\right) \qquad 4.2$$

where:

$\mu_s =$ static coefficient of friction

$\mu_d =$ dynamic coefficient of friction

$\dot{v} =$ slip rate (interface tangential velocity) in units of length/time.

D = decay coefficient, which has units of time/length. When D is zero, the equation is rewritten to be $\mu = \mu_d$ for the case of sliding and $\mu = \mu_s$ for the case of sticking

Secondly cracking and gaping failure mode in the tensile regime is simulated using tied surface to surface contact formulation. In this approach, nodes on the surface of a given masonry unit remain tied to the surface of an adjacent unit whilst failure criterion (Eq. 4.1) is satisfied, after which the surfaces are free to separate or slide with friction.

$$\left(\frac{\tau}{c}\right)^2 + \left(\frac{\sigma}{f_t'}\right)^2 \leq 1 \qquad 4.3$$

where

$\tau =$ shear interface stress

$c =$ cohesion

$\sigma =$ normal interface stress (tensile) and

$f_t' =$ tensile strength of the joint

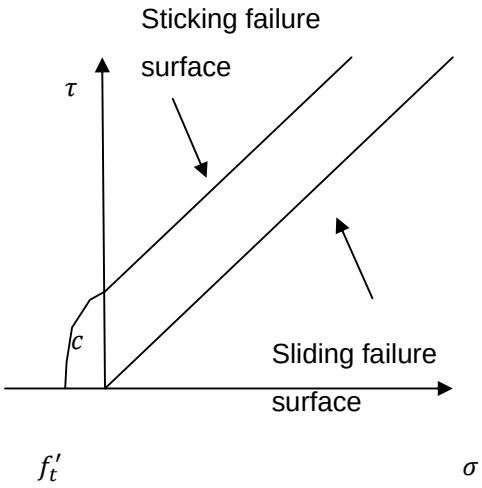

(a) Failure surfaces

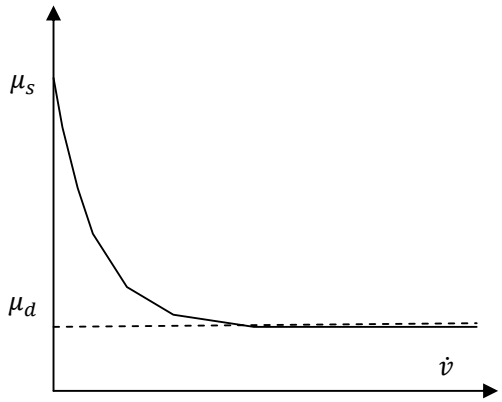

(b) Coefficient of friction

Figure 4.2 Fictional interface properties of masonry joint adopted for dynamic analysis.

Masonry, when subjected to high stress rates does exhibit enhanced bond strength due to the finite crack propagation velocity (Burnett et. al. 2007). It has been reported that the strain rate sensitivity of mortar appeared to be a function of water content. Shrinkage problem can lead to the formation of voids and micro cracks within the mortar matrix. However, the formation of voids and micro cracks may not be uniform over a cross-section because moisture evaporates more easily from the perimeter. And hence it might be expected that the tensile failure stress at the perimeter will be less than at the centre. If a masonry specimen is subject to quasi-static load, stresses are free to progressively redistribute in the cross-section prior to complete failure occurring. However, when dynamically loaded, stresses in a specimen will not have time to redistribute and consequently failure may effectively involve simultaneous mobilization of all bonds at the unit–mortar interface.

It has been reported that brick-mortar joints subjected to tensile load at strain-rates of approximately $1\ s^{-1}$ have an apparent dynamic enhancement of the bond strength with DIF equal to 3.1(Burnett et. al. 2007). Taking the strain rate of $2 * 10^{-5}\ s^{-1}$ as the reference static strain rate, DIF for ultimate compressive strength of mortar was formulated as (Wei & Hao, 2009):

$$DIF = \begin{cases} 0.0372 ln\dot{\varepsilon} + 1.4025\ for\ \dot{\varepsilon} \leq 13 s^{-1} \\ 0.3447 ln\dot{\varepsilon} + 0.5987\ for\ \dot{\varepsilon} > 13 s^{-1} \end{cases} \qquad 4.4$$

Hence based on the aforementioned works, DIF for bond strength of mortared joints can be assumed to vary from 1.44 to 3.1 for impact loading conditions.

4.3 Numerical Impact Response Simulation: LS DYNA

Numerical methods for solving structural responses resulting from interactions occurring at high rate, such as blast and impact, are generally divided into those used for prediction of actions (loads) experienced by interacting bodies and those for calculation of the resulting structural responses (action effects). The methodologies are generally categorized into uncoupled and coupled analyses.

The uncoupled analysis the actions are calculated as if the interacting structures were rigid and then applying these loads to a responding model of the structure of interest. When the actions are estimated with a rigid model of the structure, the loads on the structure are often over-predicted, particularly if significant motion or failure of the structure occurs during the loading period. For example, the blast load on structures is simulated as a transient pressure, and the response of structures under impact is estimated using impact factors for the static responses. Examples of computer codes for such simulations are DIANA, and ANSYS

For a coupled analysis, both the interacting bodies are modelled simultaneously to estimate the action effects within the components of each system. For example in estimating the effect of explosions on structures, the CFD (computational fluid mechanics) model for blast-load prediction is solved simultaneously with the CSM (computational solid mechanics) model for structural response. Whereas for impact response of structures, both the colliding systems are modelled explicitly being interlinked by superficial interface (contact elements in FE formulation). Computer codes, which are used to evaluate the responses by explicit model of interacting bodies, are AUTODYN, LS-DYNA.

For this study, the impact response of prototype arch was simulated using coupled analysis in which the arch and the drop weight were modelled explicitly and solved simultaneously.

4.3.1 Structural Modeling and Analysis

An explicit dynamic analysis was carried out to predict the failure mode and capacity of the prototype arch under impact in advance of the experimental work. The non-linear behaviour of the prototype arch under impact loading was simulated using the 3D non-linear explicit dynamic analysis programme, LS-DYNA (integrated with ANSYS). A simplified discrete-crack

finite element modelling approach has been adopted to model the non-linear performance the arch under impact load. The model was developed using linear elastic solid elements for masonry units and impactor block, and using contact elements for all interfaces in the system. The detailed description of the modelling and analysis procedure is given as comment in source code of the model (Appendix 3). The 3D model is shown in the Figure 4.3.

Analysis for self weight- the self weight was applied in advance to get stabilizing pre-compression stress against shear sliding failure of the joints. Ramped Gravity load was applied to arch model by defining a base acceleration, then explicit dynamic analysis using the method of dynamic relaxation was carried out to damp out resulting oscillations. The base acceleration was ramped from 0m/s to 9.81m/s2 for 50ms and kept constant for the next 50ms.This gravity loading history was found to be sufficient for obtaining an equivalent quasi static recompression in the arch.

Analysis for Impact- following the dynamic relaxation analysis for gravity loading, an explicit dynamic analysis was carried out applying base acceleration to both the arch and the impactor block.

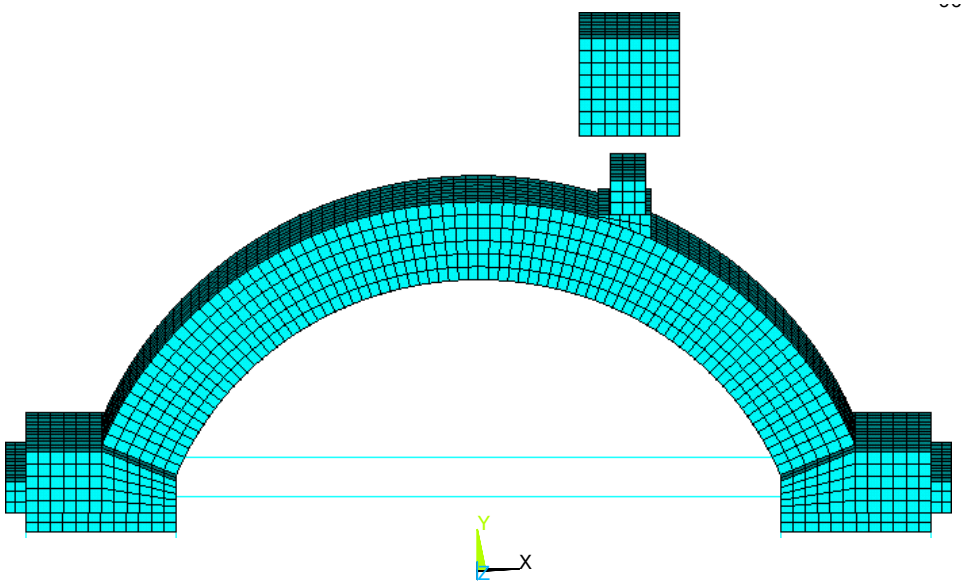

Figure 4.3 Global FM model of the prototype stone masonry arch for non-linear static analysis (drop mass = 60kg and drop height = 30cm).

4.3.2 Results and Discussion

The results of numerical simulation of the pilot model, with material properties and loading conditions described in Appendix 3, will be presented. Three rotational hinges and one sliding hinge were prominently observed at the same location as that of the numerical simulation. Two rotational hinges centered at the extrados and intrados of the left and right quarter span, one rotational hinge at the right arch-abutment interface, and one sliding hinge at the left quarter span (impacor point). At the right side abutment, the sliding was more than that of the left side as the thrust force predominantly goes to the nearby support, which in turn gives greater sliding resistance.

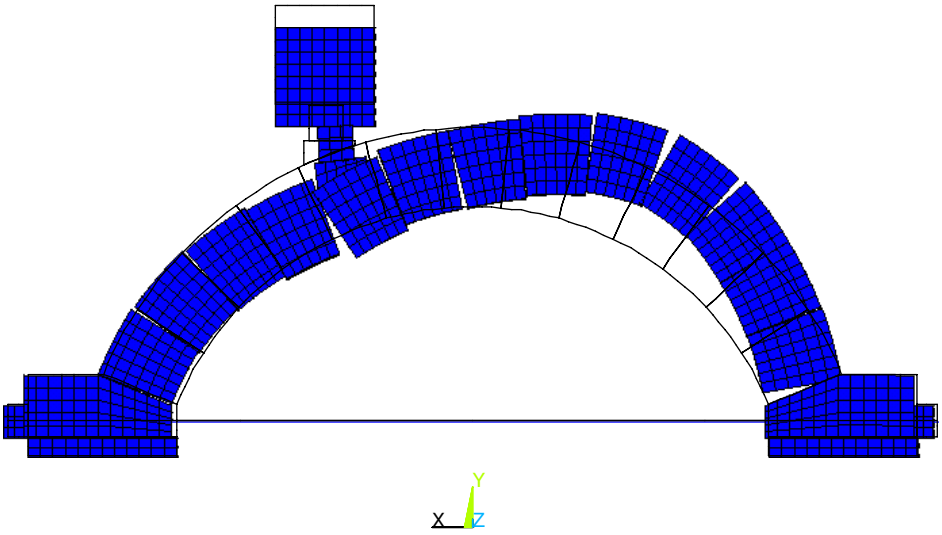

Figure 4.4 The damage mode for the pilot dry joint arch specimen (M60H30) simulated using ANSYS LS-DYNA.

Figure 4.6 , Figure 4.7 and Figure 4.7 shows the response history (displacement, velocity and acceleration history) the arch obtained by the non linear dynamic analysis. The results were taken at control node which is located at top corner of wooden wedge, which is referred as impactor point here after. As shown in the velocity diagram the impact occurs twice and the arch takes approximately 60ms to return back to the static equilibrium position. The arch attains maximum displacement of 13mm at 38ms and rebounds back with residual deformation of 9mm. Hence the FE simulation shows that the arch can absorb target kinetic

energy of 179.5 J which is much higher than predicted by quasi-static simulation (See chapter 3).

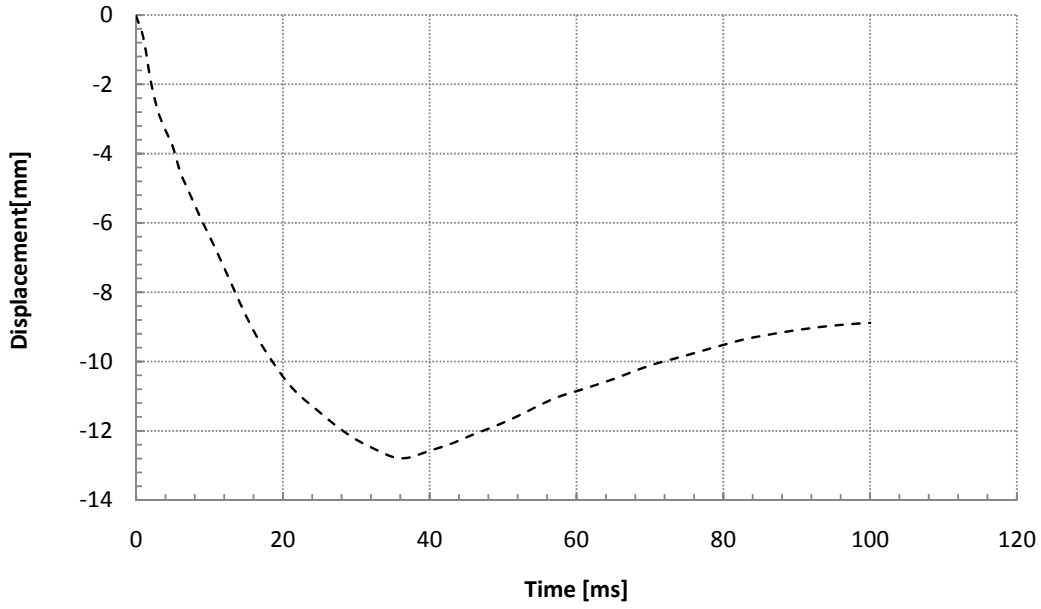

Figure 4.5 Displacement history of pilot arch model under an impact of 61kg drop weight with drop height of 30 cm.

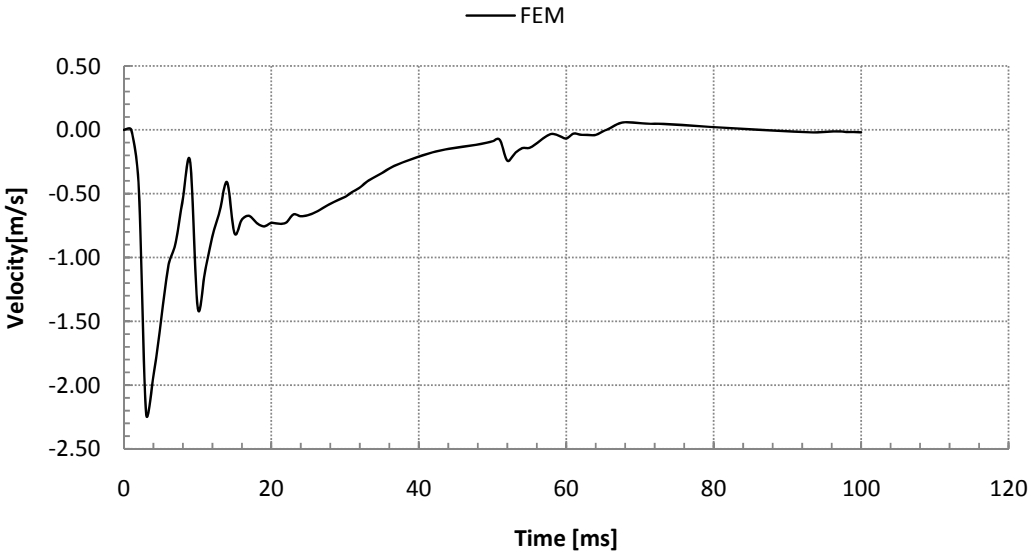

Figure 4.6 Velocity history of pilot arch model under an impact of 61kg drop weight with drop height of 30 cm.

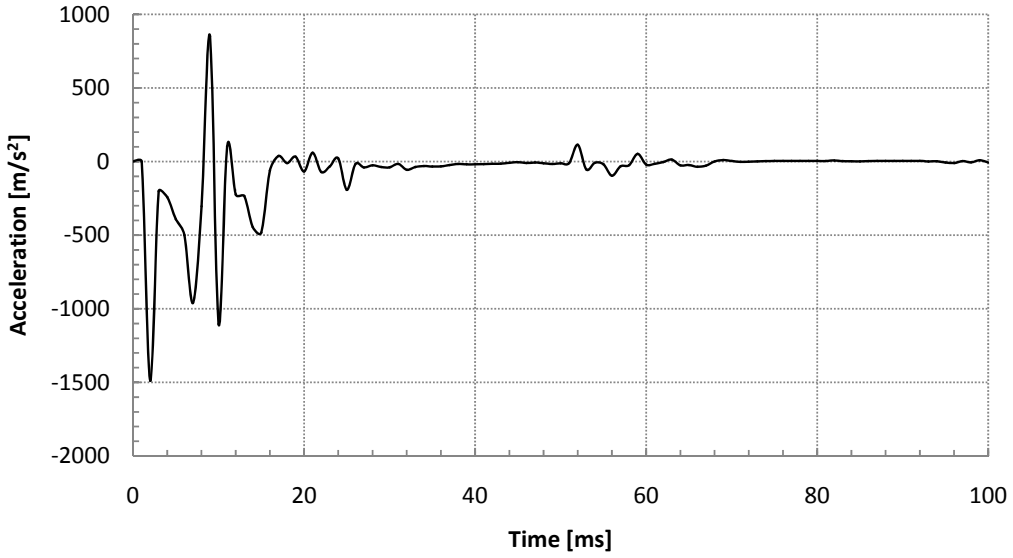

Figure 4.7 Acceleration history of pilot arch model under an impact of 61kg drop weight with drop height of 30 cm.

4.4 Experimental Impact Response Simulation

To calibrate the results from the non-linear explicit dynamic analysis, an impact experimental test was carried out on the prototype arch using a drop weight apparatus. The test was carried out in the Mechanical Engineering Department laboratory, University of Minho. The testing procedure and the corresponding results are presented in the following sections.

4.4.1 Experimental Set Up

A series of eight prototype arches were assembled within the drop weight apparatus for impact test as shown in Table 4.1.The first six of the arches were dry jointed stone masonry and the last two were mortar jointed stone masonry. The arches were constructed using the same stone units that were used for the quasi-static test. The set ups were labeled to refer the amount of drop weight and drop height. For example M60H30 refers a test specimen subjected to an impact from mass of 60.93kg dropping from a height of 30.5cm.

In all of the eight arches, the construction was carried out using a formwork that had been used for the quasi-static test. The back seat units (abutments) were set primarily with separation of 1.2m inside the apparatus and then tied together horizontally using reinforcement bars, as shown in the Figure 4.8 (a). Once the abutments were constructed, the arch ring was constructed by stacking each unit one by one up to the key stone. Finally

the key stone was driven in between the right and the left rings of the arch using a hammer. Note that the abutments are restrained laterally using the steel ties**Error! Reference source not found.**.

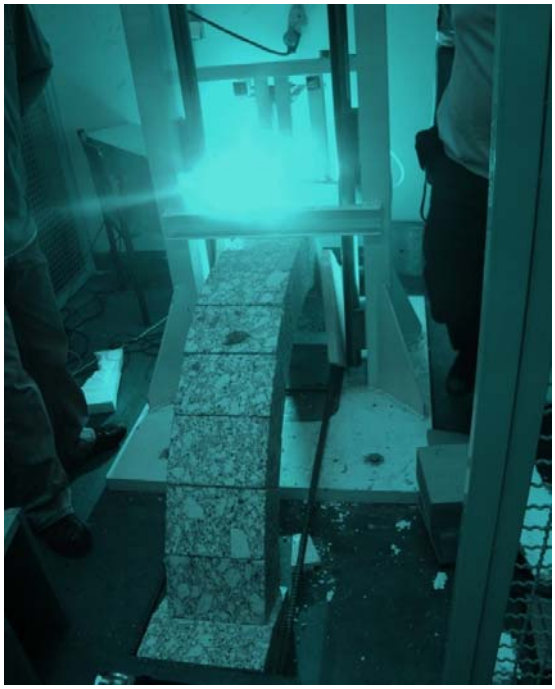

a) Assembled arch inside the drop weight apparatus cell

b) Photron camera

c) Setting the drop height

Figure 4.8 Drop weight apparatus cell.

Once the arch was constructed, a wooden bearing, with horizontal width of 11cm, out of plane thickness of 200mm, and a height (on the left) of 50mm, was glued to the fifth stone block using rapid hardening epoxy resin adhesive. The wooden wedge was place in such way that it coincides with the location of the quarter span (300mm from the center line of the arch). More over additional 7cm high wooden blocks were glued to the wooden wedge using epoxy resin to ensure that the drop weight wouldn't hit the arch units.

After the construction of every arch, a photron camera (see Figure 4.8(b)) was positioned by focusing on the units at the quarter span (just below the impactor point). The camera was placed on the same level as that of the units under focus. And then drop weights were positioned at different heights as shown in the Figure 4.8 (c).

Table 4.1 Impact test set ups and observed global response after test execution

Test set up	Drop weight (kg)	Drop height (cm)	Target kinetic energy (J)	Response after impact*
M80H45	81	450	357.57	Full collapse
M75H45	74.35	455	331.87	Full collapse
M74H20	74.35	205	149.5	Full collapse
M60H20	60.93	205	122.53	Hinges formation (3R +1S)
M60H25	60.93	255	152.45	Hinge formation (3R +1S)
M60H20	60.93	305	**182.26**	Hinge formation(3R +1S)
M60H40	60.93	405	242.11	Remains intact
M60H70	60.93	705	**421.43**	Hinge formation (1R+1S)

The responses are from visual observation after impact before lifting the drop weight

4.4.2 Test Execution

A series of tests were carried out on six dry jointed masonry arches and two mortar jointed masonry. The weights were dropped from different heights. And series of pictures of the focused units were taken using the photron camera at a rate of 3000fps. Moreover photographs of the arch specimens were made before and after impact to capture failure

mechanisms of the arch. The deformation progress of the arches below the loading point was captured using the photrone camera as shown by Figure 4.9, and Figure 4.10.

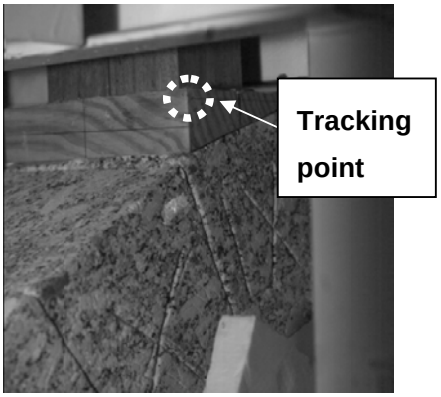	
$\Delta t = 1.0ms$	$\Delta t = 100ms$
	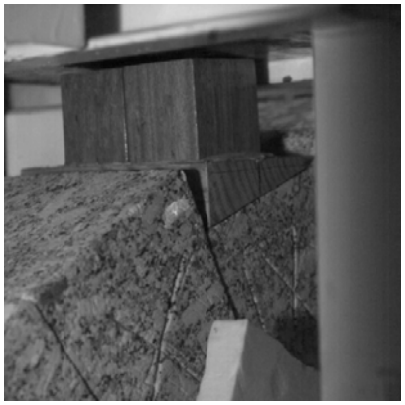
$\Delta t = 200ms$	$\Delta t = 300ms$
	
$\Delta t = 400ms$	$\Delta t = 500ms$

	
$\Delta t = 600ms$	$\Delta t = 700ms$

Figure 4.9 Deformation of dry joint arch after impact, taken by photron camera at rate of 3000fps

	
$\Delta t = 1.0ms$	$\Delta t = 100ms$
	
$\Delta t = 200ms$	$\Delta t = 300ms$

	
$\Delta t = 400ms$	$\Delta t = 500ms$
	
$\Delta t = 600ms$	$\Delta t = 700ms$

Figure 4.10 Deformation of mortar jointed arch after impact, taken by photron camera at rate of 3000fps(continued).

4.4.3 Results and Discussion

As discussed above, the deformation at quarter span was recorded using a photron camera at a rate of 3000fps. The kinematic response parameters at the control point were extracted using the TEMA software. To transform the data from units of pictures(pixels) to units of length, scaling factor was established from the vertical dimension measurements of the wooden wedge. The height of the wedge in units of pixel was calculated using distance formula using the pixel co-ordinates of the bottom and top corner points of the wedge.

The dry jointed arch was found to absorb a maximum kinetic energy of 182.27J where as the mortared jointed arch resisted an impact with target energy of 421.44J as shown in Table 4.1. Figure 4.11 shows the ultimate deformation of the arch specimens after impact test. The

first three arch specimens fully collapsed to the ground after impact as shown in the Figure 4.11 (a) and (b). The dry jointed masonry arch was found to resist a dropping mass of 61kg at a height of 30cm, which is equivalent to a target kinetic energy of 182.27J. Whereas the mortar jointed arch resisted an impact of 61kg with a target velocity of 2.6m/s.

The failure mechanism of the dry masonry arches observed during the experimental test was identical to that of the FE nonlinear explicit dynamic analysis using LS DYNA (see Figure 4.11 and Figure 4.12). Three rotational hinges and one sliding hinge were prominently observed at the same location as that of the numerical simulation for dry jointed arches. Two rotational hinges centered at the extrados and intrados of the left and right quarter span, one rotational hinge at the right arch-abutment interface, and one sliding hinge at the left quarter span below the loading point. At the right side abutment, the sliding was more than that of the left side as the thrust force predominantly goes to the nearby support, which in turn gives greater sliding resistance.

a) $M80H45$

b) $M74H20$

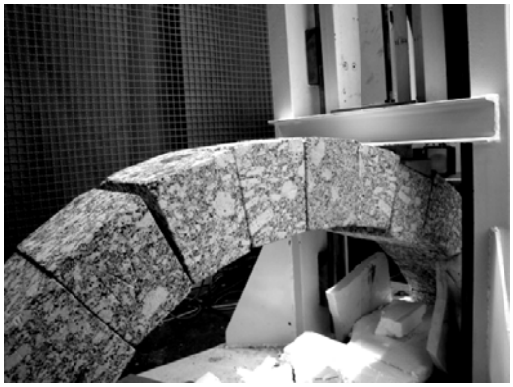

c) M60H20

d) M60H30

e) M60H40

f) M60H70

Figure 4.11 Damages of stone masonry arches after Impact test.

The mortar jointed arches perform better than the dry jointed arches. The mortar jointed arch subjected to an impact from a mass of 60.95kg dropping from a height of 40cm, responds elastically and no damage was observed after impact. On the other hand damages were observed after the impact test in the arch specimen M60H70. Three hinges were observed after impact: two hinges at impacor span (1 sliding + 1 rotational) and one rotational hinge at the right span (see Figure 4.12). No damage was observed at both abutment ends.

Hinges formed after impact of dry joint masonry arch (M60H30)

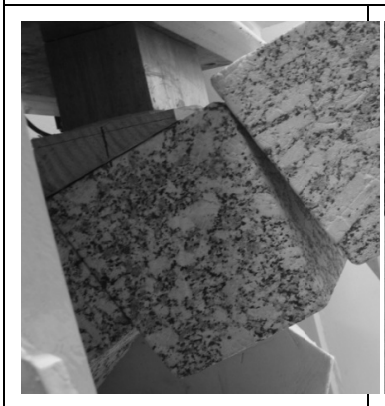

a) Left quarter span

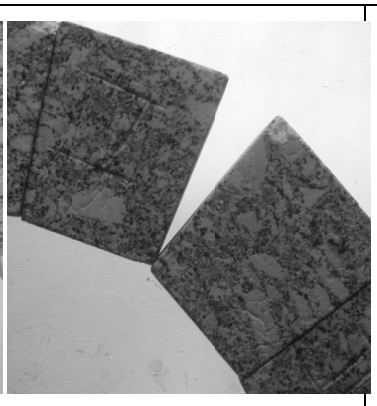

b) Right quarter span

c) Right abutment

Hinges formed after impact of mortared joint masonry arch (M60H70)

d) Left quarter span

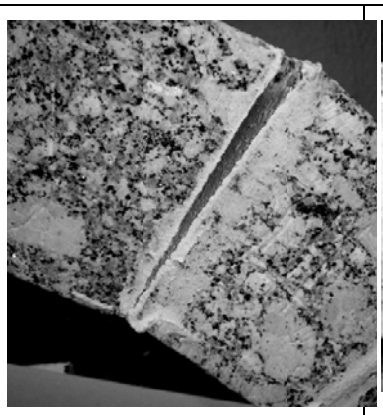

e) Right quarter span

f) Right abutment

Figure 4.12 Hinges formed after impact tests of stone masonry arches.

The kinematic response parameters of the tracking point are shown in Figure 4.13 for the typical dry joint and mortar joint masonry arches (M60H30 and M60 H70). The mortar joint arch rebounds back after impact with a less residual deformation, 5mm. whereas the dryjointed arch attains its static equilibrium position with plastic deformation of 60mm. For other arch specimens the peak values are reported in the Table 4.2.

Table 4.2 Peak experimental impact responses of stone masonry arches.

Test set up	Maximum response amplitude of quarter span (vertical)		
	Displacement (m)	Velocity(m/s)	Acceleration(m/s^2)
M80H40	**	3.19	5115.4
M74H45	**	2.99	2138.6
M74H20	**	1.91	1416.3
M60H30	0.053	2.08	1440.1
M60H25	0.04	2.13	1588.6
M60H20	0.034	1.99	1417.1
M60H70	0.0338	1.30	833.43

**The arch was fully collapsed to the ground

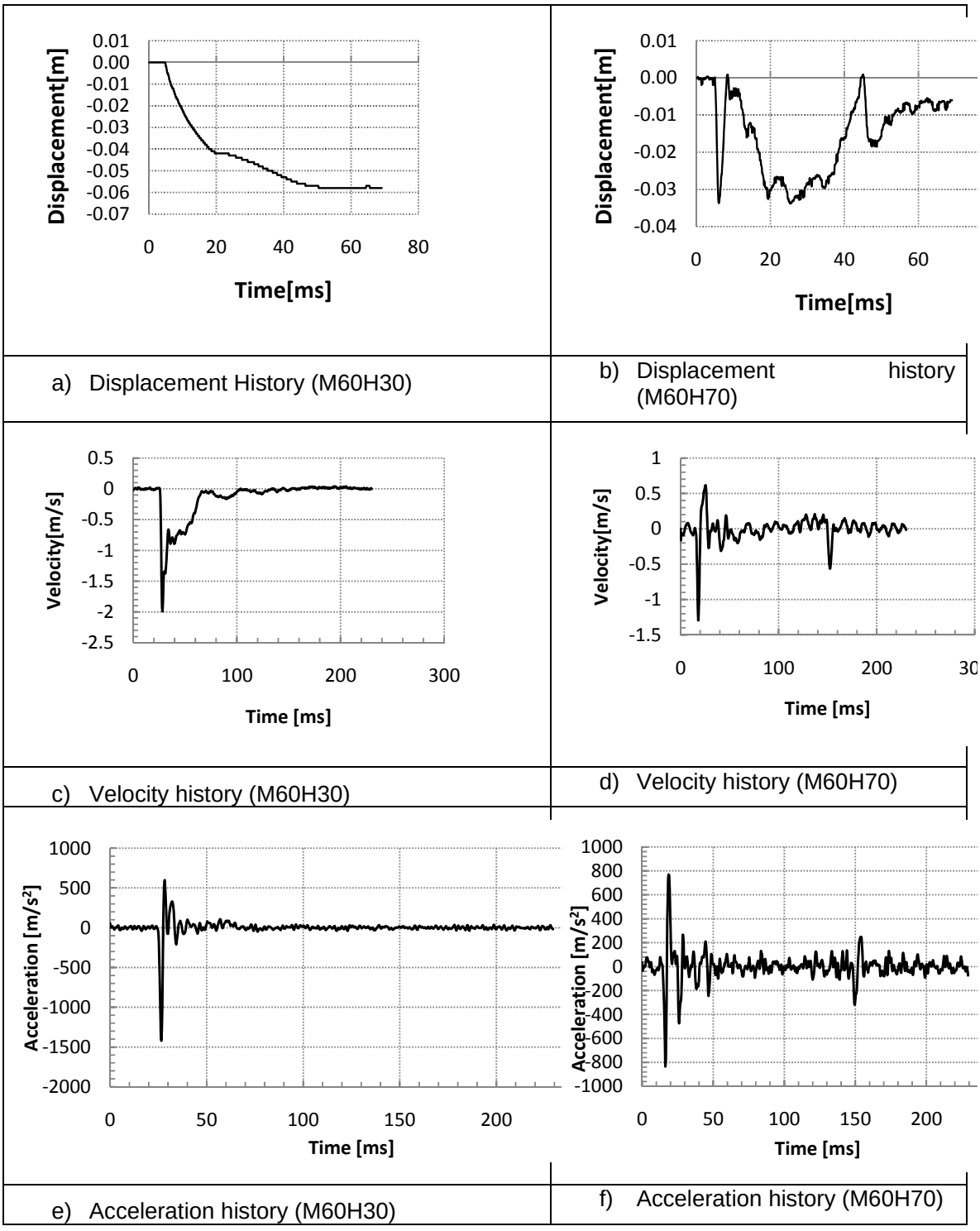

Figure 4.13 Responses after impact of dry joint masonry arch (on the left) and mortared joint masonry arch (on the right).

For the comparision of impact performance of dry joint masonry arches, displacement histories of the control point are shown in the Figure 4.14. The graph of specimen M80H45 and M74H20 shows unstablized deformation progress which is indicated by negative slop (down ward velocity) of the point until last time the picture was taken by the camera. Where as the horizontal deflection curve of specimens M60H25 and M60H30 shows that the arch attained static equilibrium with out rebound.

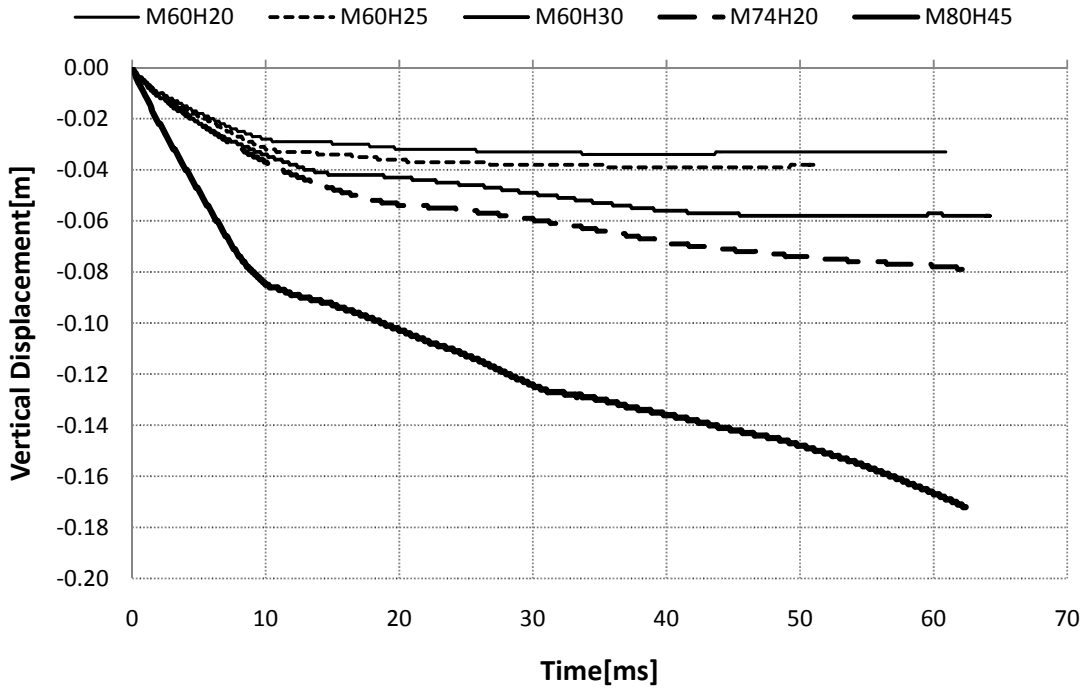

Figure 4.14 Quarter span deflection of arches at impactor points.

4.5 Validation of Structural Models

To validate the numerical model parameters, a calibration of the experimental and numerical results was made for the specimen M60H30 (dry masonry arch subjected to mass of 60.9kg dropping from a height of 30cm). The failure mechanism of the dry masonry arches observed during the experimental test was identical to that of the FE nonlinear explicit dynamic analysis using LS DYNA as shown in the Figure 4.4 and Figure 4.12. Three rotational hinges and one sliding hinge were prominently observed at the same location as that of the numerical simulation. Two rotational hinges centered at the extrados and intrados of the left

and right quarter span, one rotational hinge at the right arch-abutment interface, and one sliding hinge at the left quarter span (impacor point). At the right side abutment, the sliding was more than that of the left side as the thrust force predominantly goes to the nearby support, which in turn gives greater sliding resistance. Overall, there is good agreement between the computed and measured damage mode.

As discuss in Chapter 3, joint stiffness parameters influence the result of the numerical model, and hence a parametric study was done to calibrate the numerical result with that of experiment. In the impact response analysis, it was found that the joint stiffness greatly affects the impulse duration (temporal distribution of the) velocity response. Hence the results of three different analyses are shown in the Figure 4.15. The stiffness of the contact elements, representing the joints, are automatically evaluated by the software as discussed in Chapter 3. The adjustment of the joint stiffness is possible through the use of the coefficient called penalty factor. The penalty factor of 0.001 gives stiffness factor, $\beta_k = 0.006$, which is in a good agreement as predicted through quasi static elements.

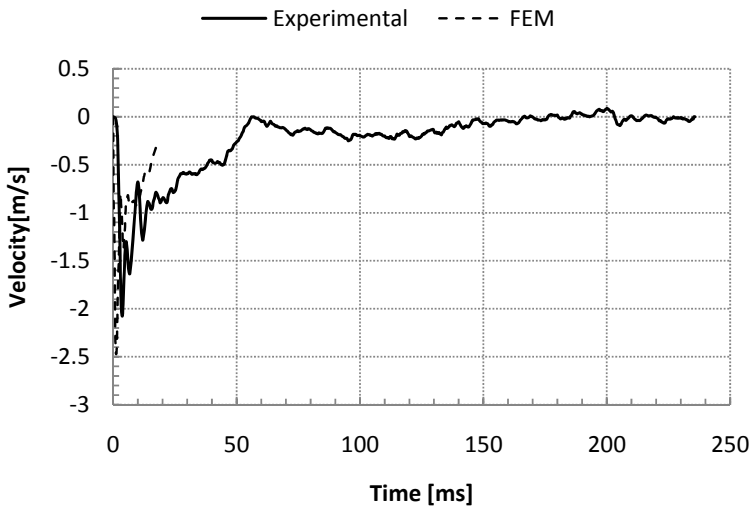

a) Velocity history, $pf = 0.01$

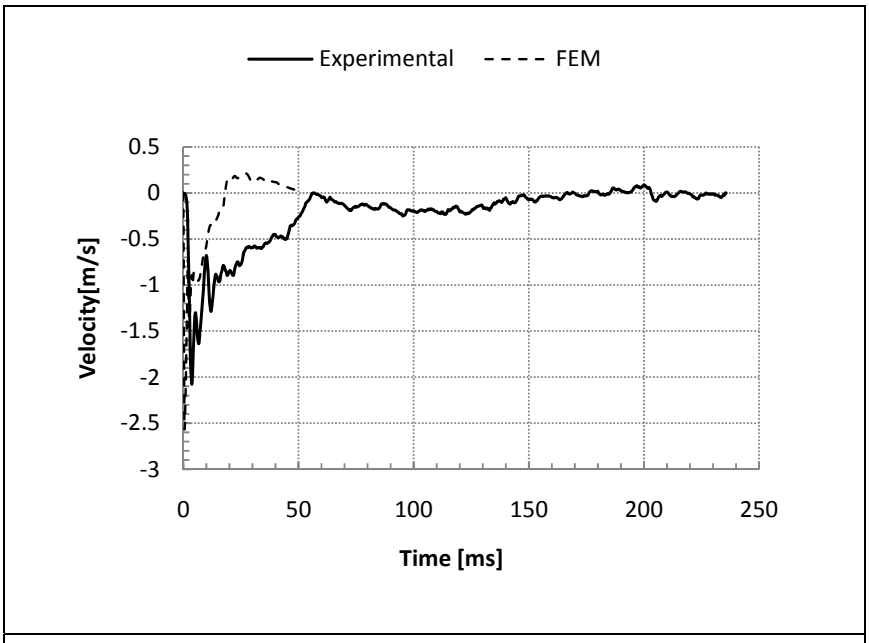

b) Velocity history, $pf = 0.005$

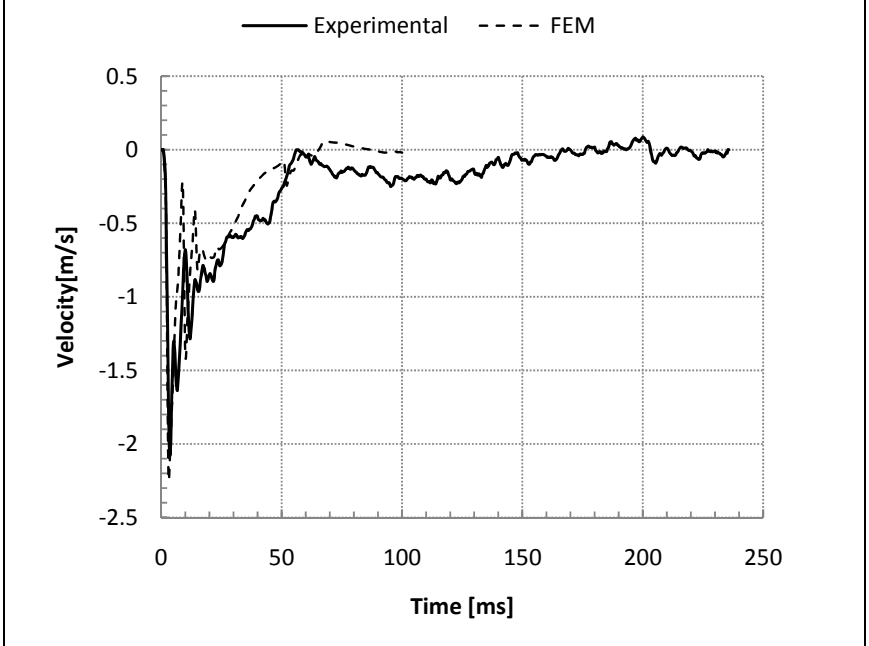

c) Velocity history, $pf = 0.001$

Figure 4.15 Comparisons of experimental and numerical impact responses of the prototype arch (M60H30) at the impactor point.

CHAPTER 5

CONCLUSIONS AND RECOMMENDATIONS

5.1 Conclusions

In this Dissertation work, both experimental and numerical studies have been conducted to investigate the performance of stone masonry bridges at high rate loading resulting from explosions. A prototype scaled arch was designed and used for both numerical and experimental simulations.

The capacity curve of stone masonry arches has been assessed by experimental testing, advanced non-linear analysis using DIANA and simplified methods using RING software. The behavior of stone masonry bridges under high rate loading has been discussed using drop-weight tests on a scaled stone masonry model, and further analyzed using a non-linear explicit dynamic analysis software (LS-DYNA).

From the results of the numerical and analytical works which have been executed in this study, the following conclusions are made:

1) A non-linear FE simulation based on discrete cracking masonry models has proposed for evaluation of the resistance function of stone masonry arches. And the model has been calibrated based on experimental results.
2) It has been found that the non-linear FE simulation based on discrete masonry material models is highly dependent on linear elastic stiffness of the masonry joints. Formulations for evaluating threshold values of interface stiffness for stone masonry bridges have been discussed and proposed.
3) The behavior of stone masonry arches at high rate dynamic loading has been simulated using drop-weight impact test. The impact responses of the experimental models were used to calibrate the numerical models. It has been found that the numerical model is highly sensitive to joint stiffness parameters.
4) It has been found that mortar jointed arches are found more robust than dry jointed masonry arches to resist impact loads.

5.2 Recommendations

Railway masonry bridges are main and unavoidable components of a railway system, moreover, their heritage value is a paramount. Hence to ensure safety of such bridges against explosion induced actions, the understanding of their behavior under blast loading should be continued by conducting both analytical and experimental researches.

As an extension of this study, the following is recommended for further research work:

1) The parameters identified to simulate the behavior of the prototype bridge can be used to generate a refined numerical model of real bridges for blast assessment.

2) The results of experimental and the refined numerical simulations developed in this study can be used as a basis for formulating simplified analytical models which can be used for fast structural assessment.

3) More refined parametric studies can be studied to define the trends of the capacity curves of stone masonry arches (with either mortar or dry joints) associated with different failure mechanisms. Once the general behavior of capacity curves are identified, a simplified resistance curve for SDOF model can be extracted.

4) The simplified capacity curves can be used to generate assessment curves using dynamic analysis of the corresponding SDOF models. These carves can be used for quick assessment of masonry bridges against blast loading.

BIBLIOGRAPHY

[1]. Bangash, M., & Bangash, T. (2006). *Explosion-Resistant Buildings.* Springer.

[2]. Berinch, A., & Francesco, U. (2004). Assessment of multi-span masonry arch bridges. I: simplified approach. *Journal of Bridge Engineering , 9* (6), 582-590.

[3]. Bulson, P. (1997). *Explosive loading of engineering structures.* London, UK: E & FN Spon.

[4]. Burnett, S. (2007). The response of masonry joints to dynamic tensile loading. *Materials and Structures , 40*, 517-527.

[5]. Continuum model for masonry: parameter estimation and validation. (1998). *Journal of Structural Engineering , 124* (6).

[6]. DIANA. (2006). *DIANA-9, Finite Element Analysis, User's Manual.* NETHERLANDS: TNO.

[7]. Fischer, K., & Haring, I. (2009). SDOF response model parameters from dynamic blast loading experiments, Engineering Structures. *Engineering Structures* , in press.

[8]. Gantes, C. J., & Pnevmatikos, N. G. (2004). Elastic-plastic response spectra for experimental blast loading. *International Journal of Impact Engineering* (30), 323-343.

[9]. Gantes, C., & Pnevmatikos, N. G. (2004). Elastic-Plastic Response Spectra for Exponential Blast Loading. *International Journal of Impact Engineering , 30*, 323-343.

[10]. Gilbert, M., Hobbs, B., & Molyneaux, T. K. (2002). The performance of unreinforced masonry subjected to low velocityimpacts: Mechanism analysis. *International Journal of Impact Engineering , 27*, 517-527.

[11]. Gilbert, m., Hobbs, B., & Molyneaux, T. (2002). The performance of unreinforced masonry walls subjected to low-velocity impacts: mechanism analysis. *International Journal of Impact Engineering , 27*, 253-275.

[12]. Hallquist, J. (1998). *LS-DYNA user manual.* Livermore Software Technology Corporation.

[13]. Hao, H., Ma, G.-M., & Lu, Y. (2002). Damage Assesment of masonry infilled RC frames subjected to blasting induced ground excitations. *Engineering Structures , 24*, 799-809.

[14]. Lourenco, P. B. (1998). Continuum model for masonry: parameter estimation and validation. *Journal of Structural Engineering , 124* (6).

[15]. LS-DYNA. (n.d.).

[16]. Molyneaux, T., Beattie, G., Gilbert, M., Burnett, S., Hobbs, B., & Newton, P. (2002). Assessment of static and dynamic failure characteristics of mortar joints in unreinforced and reinforced masonry. *Proc. British Masonry Society*, *9*, pp. 341-350.

[17]. Morison, C. (2006). Dynamic response of walls and slabs by single-degree-of-freedom analysis-a critical review and revision. *International Journal of Impact Engineering , 32*, 1214-1247.

[18]. NGO, T., Mendis, P., Gupta, A., & Ramsay, J. (2007). Blast loading and blast effects on structures-an overview. *ESJE Special Issue: Loading on Structures* .

[19]. Nystrom, U., & Gylltoft, K. (2009). Numerical studies of the combined effects of blast and fragment loading. *International Journal of Impact Engineering , article in press*, 1-11.

[20]. Pandy, A. K., Kumar, R., Paul, D. K., & Trikha, D. N. (2006). Non-linear response of concrete containment structure under blast loading. *Nuclear Engineering and Design , 236*, 993-1002.

[21]. Snyman, M. F., Bird, W. W., & Martin, J. B. (1991). A simple formulation of a dilatant joint element governed by Coulomb friction. *Engineering Computations , 8*, 215-229.

[22]. US Department of the Army. (1990). *Structures to resist the effect of accidental explosions.* Army Technical Manual, TM5-1300, Washington, DC.

[23]. Vasconcelos, G. F. (2005). *Experimental investigations on mechaics of stone masonry- characterization of granites and behavior of anicient masonry shear walls.* Ph.D. Thesis, University of Minho, Guimaraes, Portugal.

[24]. Wei, X., & Hao, H. (2009). Numerical derivation of homoginized dynamic masonry material properties with strain rate effects. *International Journal of Impact Engineering , 36*, 522-536.

APENDIX

ANSYS LS-DYNA Command File for 3D Modeling and Explicit Dynamic Analysis of Single Span Arch

```
/BATCH
! /COM,ANSYS RELEASE 11.0    UP20070125       17:52:25    06/12/2009
!==================================
!SET GEOMETRIC PARAMETERS OF THE ARCH AND TIE
!==================================
*SET,H,0.4                !RISE OF THE ARCH
*SET,L,1.2                !CLEAR SPAN OF THE ARCH
*SET,TH,.16               !RADIAL THICKNESS OF THE ARCH
*SET,W,0.2                !OUT-OF-PLANE THICKNESS OF THE ARCH
*SET,N,13                 !NUMBER OF UNITS OF THE ARCH
*SET,HAB,0.065            !HEIGHT OF THE ABUTMENT
*SET,LAB,0.3              !LENGTH OF THE ABUTMENT
*SET,DIA,0.008            !DIAMETER OF TIE (STEEL REBAR)

!==============================================
!SET PROPERTIES OF THE IMPACTOR AND WOODEN BEARING
!==============================================
*SET,HW1,0.05             !EDGE SIZE(HEIGHT) OF WOODEN WEDGE
*SET,WW1,0.105            !EDGE SIZE(HORIZONTAL LENGTH) OF WOODEN WEDGE
*SET,WW2,0.07             !EDGE SIZE(HEIGHT) OF WOODEN CUBE
```

```
*SET,ECC1,0.01                !ECCENTRICITY B/N EDGES OF WOODEN WEDGE AND STONE UNIT
*SET,ECC2,0.01          !ECCENTRICITY B/N EDGES OF WOODEN BLOCKS

*SET,WI,0.20            !WIDTH OF IMPACTOR
*SET,DI,0.35            !DEPTH OF IMPACTOR
*SET,THI,0.2            !THICKNESS OF IMPACTOR
*SET,XI,0.30    !HORIZONTAL CENTEROID OF IMPACTOR FROM ARCH CENTER[0.329]

*SET,HI,0.305                   !DROP HEIGHT OF IMPACTOR
*SET,MI,61                      !MASS OF IMPACTOR IN kILOGRAMS
*SET,DROPFRACTION,0.3       !FRACTION OF DROP HEIGHT TO BE SIMULATED DIRECTELY
*SET,GAP,DROPFRACTION*HI    !SIMULATED GAP BETWEEN THE IMPACTOR AND THE ARCH IN METERS
*SET,DEF,0.4                !EXPECTED ULTIMATE DEFORMATION OF THE ARCH AT QUARTER SPAN
*SET,HF,0.57            !CLEAR HEIGHT OF FRAME[DROP WEIGHT GUIDE]

!====================================
!SET MATERIAL PROPERTY PARAMETERS FOR STONE-ARCH
!=======================================
*SET,ESTONE,50E9                !MODULUS OF ELASTICITY OF STONE UNITS
*SET,NUSTONE,0.2                !POISNON'S RATIO
*SET,ROSTONE,2600               !DENSITY OF STONE BLOCKS

!====================================
```

```
!SET MATERIAL PROPERTY PARAMETERS FOR DRY JOINTS
!=======================================
*SET,MUS,0.6                  !STATIC COEFICIENT OF FRICTION
*SET,MUD,0.6                  !DYNAMIC COEFICIENT OF FRICTION
*SET,DECAY,0                   !EXPONENTIAL FRICTION DECAY
*SET,FTMAX,100                  !MAXIMUM TENSILE STRENGTH
*SET,TAUMAX,150                  !MAXIMUM SHEAR STRENGTH-COHESION
*SET,PF,0.1                 !GLOBAL PENALTY STIFNESS FACTOR OF ALL INTERFACES,
                           ! DEFAULT 0.1
*SET,PFS,0.005                          !PENALITY SCALE FACTOR FOR STONE[LOCAL
INTERFACE ADJUSTMENT,DEFAULT,1
!=====================================
!SET MATERIAL PROPERTY PARAMETERS STEEL-
!=======================================
*SET,ESTEEL,200E9               !MODULUS OF ELASTICITY OF STEEL
*SET,NUSTEEL,0.3                !POISNON'S RATIO
*SET,ROI,MI/(WI*DI*THI)          !DENSITY OF IMPACTOR
*SET,ROSTEEL,7800                !DENSITY OF STEEL
!=====================================
!SET MATERIAL PROPERTY PARAMETERS WOODEN BEARING
!=======================================
*SET,EWOOD,10E9                  !MODULUS OF ELASTICITY OF STONE UNITS
*SET,NUWOOD,0.3                  !POISNON'S RATIO
*SET,ROWOOD,500                   !DENSITY OF STONE BLOCKS
*SET,PFW,1                      !PENALITY SCALE FACTOR FOR WOODEN INTERFACES,
DEFAULT =1
```

```
!====================================
!SET MATERIAL PROPERTY PARAMETERS FOR sPRING-DAMPER ELEMENTS
!====================================
*SET,DC,50                    !DAMPING CONSTANT[FORCE/DISPLACEMET RATE]
*SET,KSOIL,1E9                !sPRING sTIFFNESS FOR SOL-4 SPRINGS PER ABUTMENT
!================================
!SET MESH SIZE CONTROL PARAMETERS
!================================
*SET,ND,6                     !MESHING DIVISION PER edge of stone block BLOCK
*SET,DL,TH/ND
!============================================================
!SET ACCELERATION LOAD HISTORY & INITIAL VELOCITY OF IMPACTOR
!============================================================
*SET,G,9.81                          !GRAVITATIONAL ACCELERATION IN m/s^2
*SET,TI,SQRT(2*HI/G)-SQRT(2*(HI-GAP)/G)       !TIME OF IMPACT
*SET,VIY,SQRT(2*G*(HI-GAP)),                  !INITIAL VELOCITY[m/s] OF THE IMPACTOR
AT POINT OF RELEASE(JUST ABOVE THE GAP)

*DIM,TIMEI,ARRAY,2                    !SETTING TIME VECTOR FOR ACCELERATION
LOAD DEFINITION
*SET,TIMEI(1),0,2,
*DIM,GRAVI,ARRAY,2
*SET,GRAVI(1),G,G,                      !BASE ACCELERATION LOAD VECTOR FOR
IMPACTOR

*DIM,TIMEA,ARRAY,3                    !SETTING TIME VECTOR FOR ACCELERATION
LOAD DEFINITION
```

```
*SET,TIMEA(1),0,0.05,0.1,
*DIM,GRAVA,ARRAY,3
*SET,GRAVA(1),0,G,G,                    !BASE ACCELERATION LOAD VECTOR FOR IMPACTOR
!===================================
!*SET SOLUTION AND OUT-PUT TIME STEPS [RESULT TIME HISTORY]
!===================================
*SET,BETTA,0.1                          !SOLUTION TIME STEP SIZE FRACTION AS THAT
                                        ! OF CRITICAL TIME STEP[Default 0.9]
!*SET,T,SQRT(2*(HI+DEF)/G)-SQRT(2*(HI-GAP)/G)    !DURATION OF EXECUTION [s] BASED ON FREE FALL ASSUMPTION
*SET,T,0.1                              !USER SPECIFIED DURATION OF EXECUTION
!*SET,DT,0.0001                         !OUT PUT TIME HISTORY TIME STEP
*SET,RNSTEP,100                         !NO.  OF STEPS AT WHICH RESULT IS WRITTEN TO RESULT FILE.[DEFAULT=100]
*SET,THNSTEP,1000                       !NO.  OF STEPS AT WHICH RESULT IS WRITTEN TO TIME HISTORY FILE.[DEFAULT=1000]
!*********************************************
!EVALUATE INTERMEDIATE PARAMETERS
!*********************************************
*AFUN,DEG                               !CHANGE THE ANGULAR MEASURMENTS IN TO DEGREE
*SET,RI,H/2+(L**2)/(8*H)                !INTRADOS RADIUS OF THE ARCH
*SET,RE,RI+TH                           !EXTRADOS RADIUS OF THE ARCH
*SET,THETA0,ACOS(0.5*L/RI)              !sUBTENDING ANGLE OF THE ABUTMENT
*SET,THETAS,180-2*THETA0                !SUBTENDING ANGLE OF THE ARCH
*SET,DTHETA ,THETAS/N                   !SUBTENDING ANGLE OF EACH UNIT
```

```
*SET,THETA1 ,THETA0+DTHETA                !ANGULAR LOCATION OF THE FIRST UNIT FROM HORIZONTAL

*SET,THETA2 ,ACOS((L/4+WW1/2-ECC1)/RE)    !ANGULAR LOCATION OF WOODEN BEARING LONGER VERTICAL EDGE

*SET,THETA3 ,ACOS((L/4-WW1/2-ECC1)/RE)    !ANGULAR LOCATION OF WOODEN BEARING SHORTER VERTICAL EDGE

*AFUN,RAD

/PREP7

!*************************

!DEFINE MESHING ELMENTS

!*************************

ET,1,164                  !DEFINING ELEMENT TYPE 1[SOLID 164] FOR THE IMPACTOR MASS

MP,EX,1,ESTEEL            !ASSIGNING MODULUS OF ELASTICITY FOR THE IMPACTOR

MP,NUXY,1,NUSTEEL         !ASSIGNING POISON'S RATIO FOR IMPACTOR

MP,DENS,1,ROI             !ASSIGNING DENSITY FOR THE IMPACTOR

EDMP,RIGID,1,6,7          !DEFINE RIGID [ALL DOF CONSTRAINED EXCEPT VERTICAL-TRANSLATION[Y]


ET,2,164                  !DEFINE SOLID ELEMENT[TYPE 2] FOR WOODEN BEARING

MP,EX,2,EWOOD             !ASSIGNING MODULUS OF ELASTICITY FOR THE ARCH BLOCK

MP,NUXY,2,NUWOOD          !ASSIGNING POISON'S RATIO FOR ARCH BLOCK

MP,DENS,2,ROWOOD          !ASSIGNING DENSITY FOR THE ARCH BLOCK


ET,3,164                  !DEFINE SOLID ELEMENT[TYPE 2] FOR ARCH STONE UNITS
```

```
MP,EX,3,ESTONE              !ASSIGNING MODULUS OF ELASTICITY FOR THE ARCH BLOCK
MP,NUXY,3,NUSTONE       !ASSIGNING POISON'S RATIO FOR ARCH BLOCK
MP,DENS,3,ROSTONE       !ASSIGNING DENSITY FOR THE ARCH BLOCK

ET,4,164            !DEFINING ELEMENT TYPE 4[SOLID 164] FOR THE TIE ANCHOR
MP,EX,4,ESTEEL          !ASSIGNING MODULUS OF ELASTICITY FOR THE TIE ANCHOR
MP,NUXY,4,NUSTEEL       !ASSIGNING POISON'S RATIO FOR TIE ANCHOR
MP,DENS,4,ROSTEEL       !ASSIGNING DENSITY FOR THE TIE ANCHOR
EDMP,RIGID,4,5,7        !DEFINE RIGID [ALL DOF CONSTRAINED EXCEPT VERTICAL-TRANSLATION[X]

ET,5,164                !DEFINING ELEMENT TYPE 4[SOLID 164] FOR THE ABUTMENT SEAT
MP,EX,5,ESTEEL          !ASSIGNING MODULUS OF ELASTICITY FOR THE ABUTMENT SEAT
MP,NUXY,5,NUSTEEL       !ASSIGNING POISON'S RATIO FOR ABUTMENT SEAT
MP,DENS,5,ROSTEEL       !ASSIGNING DENSITY FOR THE ABUTMENT SEAT
EDMP,RIGID,5,6,7        !DEFINE RIGID [ALL DOF CONSTRAINED EXCEPT VERTICAL-TRANSLATION[Y]

ET,6,160            !DEFINE LINK ELEMENT[TYPE 6] FOR tie
R,6,3.14*DIA**2/4.0,    !REAL CONSTANT FOR LINK ELEMENTS [aREA OF THE TIE]
MP,EX,6,ESTEEL          !ASSIGNING MODULUS OF ELASTICITY FOR REBAR
MP,NUXY,6,NUSTEEL       !ASSIGNING POISON'S RATIO REBAR
MP,DENS,6,ROSTEEL       !ASSIGNING DENSITY FOR THE REBAR
```

```
ET,7,165              !DEFINE sPRING eLEMET [TYPE 5] FOR SOIL
R,7                   !REAL CONSTANT FOR SOIL SPRING ELEMENTS [TYPE 5]
TB,DISCRETE,7,,,0     !REAL CONSTANT UNDERLING SOIL [TYPE 5]
TBDATA,1,KSOIL        !ASSIGNING lINEAR eLASTIC sTIFFNESS

ET,8,165              !DEFINE DAMPER eLEMET [TYPE 6] FOR SOIL
R,8                   !REAL CONSTANT FOR SOIL DAMPER ELEMENTS [TYPE 6]
TB,DISCRETE,8,,,1     !REAL CONSTANT UNDERLING SOIL [TYPE 6]
TBDATA,1,DC           !ASSIGNING lINEAR eLASTIC sTIFFNESS

ET,9,164
EDMP,RIGI,9,7,7
MP,DENS,9,ROSTEEL
MP,EX,9,ESTEEL
MP,NUXY,9,NUSTEEL

!==================================
!GENERATE GEOMETRY-DEFINE KEY POINTS
!==================================
*AFUN,DEG
CSYS,1                !CHANGE THE GLOBLAL CARTESIAN TO CYLINDERICAL COR.
SYSTEM
K,1,0,0,              !CENTER OF THE ARCH
K,2,RI,THETA0         !-----------------------------------------
K,3,RE,THETA0         !DEFINE KEY POINTS OF A STONE UNIT-ARCH
K,4,RE,THETA1         !
```

```
K,5,RI,THETA1                !-----------------------------------------

K,6,RE,THETA2                !-------------------------------
K,7,RE,THETA3                !
CSYS,0                       !KEY POINTS OF WOODEN WEDGE
K,8,L/4+WW1/2-ECC1,RE*SIN(THETA2)+HW1  !
K,9,L/4-WW1/2-ECC1,RE*SIN(THETA2)+HW1  !---------------------------------

K,10,L/4+WW1/2-ECC1-ECC2,RE*SIN(THETA2)+HW1        !----------------------
K,11,L/4+WW1/2-ECC1-ECC2,RE*SIN(THETA2)+HW1+WW2            !KEY POINTS OF
wooden block
K,12,L/4+WW1/2-ECC1-ECC2-WW2,RE*SIN(THETA2)+HW1+WW2  !
K,13,L/4+WW1/2-ECC1-ECC2-WW2,RE*SIN(THETA2)+HW1     !-----------------------

K,14,XI+WI/2,RE*SIN(THETA2)+HW1+WW2+GAP     !----------------------
K,15,XI+WI/2,RE*SIN(THETA2)+HW1+WW2+GAP+THI   !KEY POINTS OF IMPACTOR
K,16,XI-WI/2,RE*SIN(THETA2)+HW1+WW2+GAP+THI   !
K,17,XI-WI/2,RE*SIN(THETA2)+HW1+WW2+GAP     !----------------------

K,18,L/2,0.5*L*TAN(THETA0)-HAB,-0.25*W          !--------------------------------
K,19,RE*COS(THETA0),0.5*L*TAN(THETA0)-HAB,-0.25*W     !
K,20,L/2+LAB,0.5*L*TAN(THETA0)-HAB,-0.25*W          !
K,21,L/2+LAB ,RE*SIN(THETA0),-0.25*W            !kEY POINTS OF THE ABUTMENT
CSYS,1                                  !
K,22,RE,THETA0,-0.25*W                          !
K,23,RI,THETA0,-0.25*W                         !--------------------------------
```

```
CSYS,0
K,24,L/2+LAB,0.5*L*TAN(THETA0)-HAB,-0.25*W            !-----------------------
K,25,L/2+LAB+0.2*W,0.5*L*TAN(THETA0)-HAB,-0.25*W !KEY POINTS OF  TIE ANCHOR
K,26,L/2+LAB+0.2*W,0.5*L*TAN(THETA0),-0.25*W           !
K,27,L/2+LAB,0.5*L*TAN(THETA0),-0.25*W                 !-----------------------

K,28,L/2+LAB+0.2*W,0.5*L*TAN(THETA0)-0.5*HAB,-0.25*W   !-----------------------
K,29,L/2+LAB+0.2*W,0.5*L*TAN(THETA0)-0.5*HAB,W+0.25*W  !KEY POINTS OF THE TIE
KSYMM,X,28,29                                          !-----------------------

K,32,L/2,0.5*L*TAN(THETA0)-HAB-0.2*W,-0.25*W           !---------------------------
K,33,L/2+LAB,0.5*L*TAN(THETA0)-HAB-0.2*W,-0.25*W   !KEY POINTS OF ABUTMENT
SEAT
K,34,L/2+LAB,0.5*L*TAN(THETA0)-HAB,-0.25*W             !
K,35,L/2,0.5*L*TAN(THETA0)-HAB,-0.25*W                 !---------------------------

K,36,L/2,0.5*L*TAN(THETA0)-HAB-0.25*W,-0.25*W          !---------------------------
K,37,L/2+LAB,0.5*L*TAN(THETA0)-HAB-0.25*W,-0.25*W      !
K,38,L/2,0.5*L*TAN(THETA0)-HAB-0.25*W,W+0.25*W         !KEY POINTS FOR SOIL
SPRINGS
K,39,L/2+LAB,0.5*L*TAN(THETA0)-HAB-0.25*W,W+0.25*W     !
KSYMM,X,36,39                                          !---------------------------

!==================================
!GENERATE THE ARCH[STONE UNITS]
```

```
!==================================
CSYS,1
A,2,3,4,5
VOFFST,1,W, ,
TYPE,3                    !SPECIFYING ELEMENT TYPE FOR MESHING ARCH BLOCK
MAT,3                     !SPECIFYING MATERIAL TYPE FOR MESHING ARCH BLOCK
ESIZE,DL,                 !SETTING MESHING SIZE-NO. OF DIVISIONS OF VOL. EDGES
VMESH,1                   !MESHING VOLUME 2 (ARCH BLOCK)
VGEN,N,ALL,,,,DTHETA
*AFUN,RAD
!==========================================
!CREATE JOINT INTERFACES BETWEEN STONE UNITS
!==========================================
EDCONTACT,PF              !SPECIFY SCALE FACTOR FOR SLIDING INTERFACE PENALITY STIFFNESS
ASEL,S,,,5                !SELCT CONTACT SURFACE AREA LABELED AS 5
NSLA,S                    !SELECT NODES ATTATCHED TO THE SELECTED AREA 5
CM,J1T,NODE               !CREATE COMPONENT J1T(TARGET OF JOINT 1) CONSISTING SELECTED NODES
ASEL,S,,,9                !SELCT CONTACT SURFACE AREA LABELED AS 5
NSLA,S                    !SELECT NODES ATTATCHED TO THE SELECTED AREA 5
CM,J1C,NODE               !CREATE COMPONENT J1C(CONTACT SET OF JOINT 1) CONSISTING SELECTED NODES
EDCGEN,TSTS,J1C,J1T,MUS,MUD,DECAY,,,FTMAX,TAUMAX   !GENERATE NODES-TO-SURFACE CONTACT JIC AND J1T WITH FRICTION PROPERTIES:MUS,MUD,DECAY
EDCMORE,ADD,1, ,PFS,PFS,
```

```
ASEL,S,,,11                    !---------------------------------------------
NSLA,S                         !
CM,J2T,NODE                    !
ASEL,S,,,15                    !GENERATE NODE-TO SURFACE CONTACT AT JOINT 2
[J2C TO J2T]
NSLA,S                         !
CM,J2C,NODE                    !
EDCGEN,TSTS,J2C,J2T,MUS,MUD,DECAY,,,FTMAX,TAUMAX     !--------------------------------
EDCMORE,ADD,2, ,PFS,PFS,
ASEL,S,,,17
NSLA,S
CM,J3T,NODE
ASEL,S,,,21
NSLA,S
CM,J3C,NODE
EDCGEN,TSTS,J3C,J3T,MUS,MUD,DECAY,,,FTMAX,TAUMAX
EDCMORE,ADD,3, ,PFS,PFS,
ASEL,S,,,23
NSLA,S
CM,J4T,NODE
ASEL,S,,,27
NSLA,S
CM,J4C,NODE
EDCGEN,TSTS,J4C,J4T,MUS,MUD,DECAY,,,FTMAX,TAUMAX
EDCMORE,ADD,4, ,PFS,PFS,
```

```
ASEL,S,,,29
NSLA,S
CM,J5T,NODE
ASEL,S,,,33
NSLA,S
CM,J5C,NODE
EDCGEN,TSTS,J5C,J5T,MUS,MUD,DECAY,,,FTMAX,TAUMAX
EDCMORE,ADD,5, ,PFS,PFS,
ASEL,S,,,35
NSLA,S
CM,J6T,NODE
ASEL,S,,,39
NSLA,S
CM,J6C,NODE
EDCGEN,TSTS,J6C,J6T,MUS,MUD,DECAY,,,FTMAX,TAUMAX
EDCMORE,ADD,6, ,PFS,PFS,
!---------------------------------
ASEL,S,,,41
NSLA,S
CM,J7C,NODE
ASEL,S,,,45
NSLA,S
CM,J7T,NODE
EDCGEN,TSTS,J7C,J7T,MUS,MUD,DECAY,,,FTMAX,TAUMAX
EDCMORE,ADD,7, ,PFS,PFS,
```

```
ASEL,S,,,47
NSLA,S
CM,J8C,NODE
ASEL,S,,,51
NSLA,S
CM,J8T,NODE
EDCGEN,TSTS,J8C,J8T,MUS,MUD,DECAY,,,FTMAX,TAUMAX
EDCMORE,ADD,8, ,PFS,PFS,
ASEL,S,,,53
NSLA,S
CM,J9C,NODE
ASEL,S,,,57
NSLA,S
CM,J9T,NODE
EDCGEN,TSTS,J9C,J9T,MUS,MUD,DECAY,,,FTMAX,TAUMAX
EDCMORE,ADD,9, ,PFS,PFS,
ASEL,S,,,59
NSLA,S
CM,J10C,NODE
ASEL,S,,,63
NSLA,S
CM,J10T,NODE
EDCGEN,TSTS,J10C,J10T,MUS,MUD,DECAY,,,FTMAX,TAUMAX
EDCMORE,ADD,10, ,PFS,PFS,
ASEL,S,,,65
```

```
NSLA,S
CM,J11C,NODE
ASEL,S,,,69
NSLA,S
CM,J11T,NODE
EDCGEN,TSTS,J11C,J11T,MUS,MUD,DECAY,,,FTMAX,TAUMAX
EDCMORE,ADD,11, ,PFS,PFS,
ASEL,S,,,71
NSLA,S
CM,J12C,NODE
ASEL,S,,,75
NSLA,S
CM,J12T,NODE
EDCGEN,TSTS,J12C,J12T,MUS,MUD,DECAY,,,FTMAX,TAUMAX
EDCMORE,ADD,12, ,PFS,PFS,
!***********************************
!GENERATE WOODEN WEDGE
!***********************************
L,7,6
CSYS,0
L,6,8
L,8,9
L,9,7
AL,157,158,159,160
VOFFST,79,W, ,
TYPE,2                !SPECIFYING ELEMENT TYPE FOR MESHING WOODEN BEARING
```

```
MAT,2                          !SPECIFYING MATERIAL TYPE FOR MESHING WOODEN
BEARING
ESIZE,DL,                  !SETTING MESHING SIZE- OF VOL. EDGES
VMESH,14                     !MESHING VOLUME 79 (wooden wedge)
!-----------------------------------
!GENERATE THE INTERFACE BETWEEN THE ARCH AND WOODEN BEARING
!-----------------------------------
ASEL,S,,,81
NSLA,S
CM,JWAC,NODE
ASEL,S,,,28
NSLA,S
CM,JWAT,NODE
EDCGEN,TDNS,JWAC,JWAT,MUS,MUD,DECAY
EDCMORE,ADD,13, ,PFW,PFW,

!*********************************
!GENERATE WOODEN BEARINGS
!*********************************
A,10,11,12,13
VOFFST,85,W, ,
TYPE,2                      !SPECIFYING ELEMENT TYPE FOR MESHING IMPACTOR
MAT,2                      !SPECIFYING MATERIAL TYPE FOR MESHING IMPACTOR
ESIZE,DL,                   !SETTING MESHING SIZE- OF VOL. EDGES
VMESH,15                     !MESHING VOLUME 15 (Impactor cube)
!-------------------------------------------------------
```

```
!GENERATE THE INTERFACE BETWEEN THE WOODEN BEARING AND WEDGE
!-----------------------------------------------------------
ASEL,S,,,83
NSLA,S
CM,JWWC,NODE
ASEL,S,,,90
NSLA,S
CM,JWWT,NODE
EDCGEN,TDNS,JWWC,JWWT,MUS,MUD,DECAY
EDCMORE,ADD,14, ,PFW,PFW,


!***********************************
!GENERATE IMPACTOR
!*********************************
A,14,15,16,17
VOFFST,91,W, ,
TYPE,1                    !SPECIFYING ELEMENT TYPE FOR MESHING IMPACTOR
MAT,1                     !SPECIFYING MATERIAL TYPE FOR MESHING IMPACTOR
ESIZE,DL,                  !SETTING MESHING SIZE- OF VOL. EDGES
VMESH,16                    !MESHING VOLUME 16 (Impactor)
!-------------------------------------
!GENERATE THE INTERFACE BETWEEN THE IMPACTOR AND WOODEN BEARING
!-------------------------------------
vsel,s,,,1,15
eslv,s
nsle,s
```

```
CM,JIAC,NODE
vsel,s,,,16
eslv,s
nsle,s
CM,JIAT,NODE
EDCGEN,ASTS,JIAC,JIAT,
!**********************************
!GENERATE THE ABUTMENT
!**********************************
A,18,19,22,23
A,19,20,21,22
VOFFST,97,1.5*W,
VOFFST,98,1.5*W,
TYPE,3                    !SPECIFYING ELEMENT TYPE FOR ABUTMENT
MAT,3                     !SPECIFYING MATERIAL TYPE FOR MESHING ABUTMENT
ESIZE,DL,                 !SETTING MESHING SIZE-NO. OF DIVISIONS OF VOL. EDGES
VMESH,17                  !MESHING VOLUME 16 (ABUTMENT)
VMESH,18                  !MESHING VOLUME 17 (ABUTMENT)
VSEL,S,,,17,18
VSYMM,X,ALL
!-------------------------------------
!GENERATE THE INTERFACE BETWEEN THE ARCH AND ABUTMENT
!-------------------------------------
ASEL,S,,,3
NSLA,S
CM,JAABCR,NODE
```

```
ASEL,S,,,102
NSLA,S
CM,JAABTR,NODE
EDCGEN,NTS,JAABCR,JAABTR,MUS,MUD,DECAY,,,FTMAX,TAUMAX
EDCMORE,ADD,16, ,PFS,PFS,
ASEL,S,,,77
NSLA,S
CM,JAABCL,NODE
ASEL,S,,,113
NSLA,S
CM,JAABTL,NODE
EDCGEN,NTS,JAABCL,JAABTL,MUS,MUD,DECAY,,,FTMAX,TAUMAX
EDCMORE,ADD,17, ,PFS,PFS,
ASEL,S,,,101
NSLA,S
CM,JABCR,NODE
ASEL,S,,,108
NSLA,S
CM,JABTR,NODE
EDCGEN,TDNS,JABCR,JABTR,MUS,MUD,DECAY
ASEL,S,,,112
NSLA,S
CM,JABCL,NODE
ASEL,S,,,120
NSLA,S
CM,JABTL,NODE
```

```
EDCGEN,TDNS,JABCL,JABTL,MUS,MUD,DECAY
!************************************
!GENERATE tIE-ANCHOR PLATE
!************************************
A,24,25,26,27
VOFFST,121,1.5*W,
TYPE,4                    !SPECIFYING ELEMENT TYPE FOR MESHING ANCHOR
MAT,4                     !SPECIFYING MATERIAL TYPE
ESIZE,DL,                 !SETTING MESHING SIZE- OF VOL. EDGES
VMESH,21                  !MESHING VOLUME 20 (ANCHOR PLATE)
VSEL,S,,,21
VSYMM,X,ALL
!-----------------------------------------------------
!GENERATE THE INTERFACE BETWEEN THE ABUTMENT AND ANCHOR
!-----------------------------------------------------
ASEL,S,,,106              !CREATE RIGHT ABUT- TIE ANCHOR INTERFACE
NSLA,S
CM,RABACC,NODE
ASEL,S,,,126
NSLA,S
CM,RABACT,NODE
EDCGEN,NTS,RABACC,RABACT,MUS,MUD,DECAY

ASEL,S,,,118              !CREATE LEFT ABUT TIE ANCHOR INTERFACE
NSLA,S
CM,LABACC,NODE
```

```
ASEL,S,,,132
NSLA,S
CM,LABACT,NODE
EDCGEN,NTS,LABACC,LABACT,MUS,MUD,DECAY

!-----------------------------------------------------
!GENERATE TIES AND ATTACH TO THE ANCHOR PLATE
!-----------------------------------------------------

L,29,31                    ! CREATE REBAR TIES
L,28,30
LSEL,S,,,263,264
LESIZE,ALL,,,4
TYPE,6
MAT,6
REAL,6
LMESH,ALL

KSEL,S,,,28,29
NSLK,S          !CONNNECT THE TIE AND RIGHT ANCHOR
CM,RTAC,NODE
ASEL,S,,,124
NSLA,S
CM,RTAT,NODE
EDCGEN,TDNS,RTAC,RTAT,MUS,MUD,DECA
```

```
KSEL,S,,,30,31          !CONNNECT THE TIE AND LEFT ANCHOR
NSLK,S
CM,LTAC,NODE
ASEL,S,,,130
NSLA,S
CM,LTAT,NODE
EDCGEN,TDNS,LTAC,LTAT,MUS,MUD,DECA
ALLSEL
!*************************************
!GENERATE ABUTMENT SEAT
!*************************************
A,32,33,34,35
VOFFST,133,1.5*W,
TYPE,5                  !SPECIFYING ELEMENT TYPE FOR MESHING ABUTMET SEAT
MAT,5                   !SPECIFYING MATERIAL TYPE
ESIZE,DL,               !SETTING MESHING SIZE- OF VOL. EDGES
VMESH,23                !MESHING VOLUME 21 (BACK RESTRAING BAR)
VSEL,S,,,23
VSYMM,X,ALL
!-----------------------------------------------------
!GENERATE THE INTERFACE BETWEEN THE ABUTMENT AND GROUND SEAT
!-----------------------------------------------------
ASEL,S,,,100            !CREATE RIGHT ABUT SOIL INTERFACE
ASEL,A,,,105
NSLA,S
CM,RABSOC,NODE
```

```
ASEL,S,,,137
NSLA,S
CM,RABSOT,NODE
EDCGEN,NTS,RABSOC,RABSOT,MUS,MUD,DECAY

ASEL,S,,,111                !CREATE LEFT ABUT SOIL INTERFACE
ASEL,A,,,117
NSLA,S
CM,LABSOC,NODE
ASEL,S,,,143
NSLA,S
CM,LABSOT,NODE
EDCGEN,NTS,LABSOC,LABSOT,MUS,MUD,DECAY
ALLSEL
!!!!!!!!!!!!!!!!!!!!!!!!!!!!!!!!!!!!

!-------------------------------------------------------
!CREATE SOIL SPRING-DAMPER ELEMETS
!-------------------------------------------------------
L,36,32                     ! CREATE SOIL SPRING ELEMETS
L,37,33
L,38,190
L,39,191
L,40,194
L,41,195
L,42,198
```

```
L,43,199
LSEL,S,,,289,296
LESIZE,ALL,,,1
TYPE,7
MAT,7
REAL,7
LMESH,ALL

KSEL,S,,,36,43
NSLK,S
D,ALL,ALL       !cONSTRAINE THE OUTER BOUND NODES OF SOIL SPRING-DAMPERS
ALLS
!*********************************
!*CREATE COMPONENTS
!*********************************
VSEL,S,,,1,15
VSEL,A,,,17,20
NSLV,S
CM,ARCH,NODE

VSEL,S,,,16
NSLV,S
CM,IMPACTOR,NODE
VSEL,S,,,1,20
NSLV,S
CM,ARCHSYSTEM,NODE
```

```
ALLSEL
EPLOT
!***********************************
!*SPECIFY LOAD
!***********************************
EDLOAD,ADD,ACLY,,ARCH,TIMEA,GRAVA,1          !APPLY RAMP LOAD FOR STATIC
                                              ! PRELOADING OF THE ARCH
TIME,0
EDDRELAX,DYNA
EDLOAD,ADD,ACLY,,IMPACTOR,TIMEI,GRAVI        !APPLY TRANSIENT GRAVITY FOR
                                              ! THE IMPACTOR AND ARCH
EDVEL,VELO,IMPACTOR,,-VIY
ALLSEL
EPLOT
```